PH.D. IN ASTRONOMY, ASTROPHYSICS
AND SPACE SCIENCE

CYCLE XXVIII

Early cosmic star formation in the Milky Way environment

Matteo de Bennassuti
A.Y. 2015/2016

Supervisor: Prof. Raffaella Schneider

Co-supervisors: Dr. Stefania Salvadori
Dr. Luca Graziani

Coordinator: Prof. Pasquale Mazzotta

Deputy Coordinator: Prof. Roberto Capuzzo Dolcetta

Contents

Abstract

Understanding how the first stars formed and gave rise to the first galaxies is one of the major challenges of modern Cosmology.
In standard Λ Cold Dark Matter (ΛCDM) cosmological models the formation of dark matter (DM) structures occurs hierarchically from smaller DM halos (the so-called "mini-halos", with virial temperatures $T_{vir} < 10^4$K and total mass $\sim 10^6 M_\odot$ collapsing at redshift $z \approx 20$) which gradually merge to form larger halos ($T_{vir} \geqslant 10^4$K). Prior to the formation of the stars, the gas in the primordial Universe was made mostly by H and He, with traces of Li and Be. Indeed, heavier elements (the so-called metals) are formed in the interior of stars and released into the surrounding gas through stellar winds and supernova (SN) explosions. Hence, the first stars, referred to as Population III (Pop III) stars, have formed in DM halos out of metal-free gas. Numerical simulations that study the formation of the first stars and look at different physical processes do not agree in the final mass of Pop III stars: while some simulations predict them to be much more massive than present-day stars, from ~10s to 100s $M_\odot$ (or even ~1000 $M_\odot$), others show that they can also have subsolar masses. Hence the initial mass function (IMF) of Pop III stars is still largely unknown.
Being likely massive, Pop III stars do not survive until today, however they are the first sources of chemical enrichment, producing metals and dust. Heavy elements provide efficient cooling channels for the formation of subsequent less massive stars, the so called Population II (Pop II) stars, which could survive to present-day. Although it has been demonstrated that the presence of heavy elements can trigger the transition to the first low-mass stars at a given metallicity Z, the role of metal line-cooling and dust cooling in driving this transition is still debated.
The duration of Pop III star formation and their impact on cosmic evolution depend on the complex interplay of different feedback processes, other than the chemical one. The ultraviolet (UV) radiation quenches star formation by photo-dissociating H_2 molecules (i.e. the main coolant at high-z) and gradually (re)ionize H in the intergalactic medium (IGM), reducing/suppressing gas infall in mini-halos. When exploding, Pop III stars also eject gas from the halo through SN-driven outflows. Thus the duration of the Pop III epoque is unknown due the complex interplay between these feedback effects.
Up to now no metal-free star has been detected. Yet a promising way to investigate the properties of Pop III stars is by studying the ancient most metal-poor stars observed in our own Milky Way (MW) and its environment. Measuring the chemical abundances in their photosphere and assuming that they are the same of their natal cloud, polluted by Pop III stars, allows to constrain the nucleosynthetic products of Pop III stars. In addition, the number distribution of stars as function of their [Fe/H], the so-called Metallicity Distribution Function (MDF), provides constraints on the physical processes regulating star formation at high-z. Large surveys provide the Galactic halo MDF and chemical abundances of most metal-poor stars, showing an increasing

[C/Fe] with decreasing [Fe/H]. These observations could give important information on the nature of the first stars, on the physical processes driving the transition to the first low-mass stars, and on feedback effects regulating star formation at high-z.
To unveil the potential of these observations, adequate theoretical models must be adopted to connect high-z star formation with the MW local relics. Here we use two complementary tools:
(*i*) GAMETE, a code which follows star formation in a large sample of semi-analytical DM merger trees (plausible MW formation histories, which is unknown) thus allowing to rapidly explore different model parameters and to statistically quantify the errors induced by different histories, although no spatial information is provided;
(*ii*) GAMESH, a pipeline where GAMETE is applied to a DM merger tree from an N-body simulation, and combined with the radiative transfer code CRASH. This approach cannot account for different MW formation histories, but allows to follow in detail the build-up of the MW accounting for the spatial distribution of the star forming progenitors and for the ionizing radiation they produce locally.
The outline of the Thesis is the following:
In Chapter 1 we describe the theory of formation of DM halos where first stars form. In particular we focus on the physics leading to the formation of Pop III stars and to the transition to low-mass stars, describing the main feedback processes which could affect the star formation at high-z. We also present available observations for ancient metal-poor stars in the MW Galactic halo.
In Chapter 2 we investigate whether current observations of the Galactic halo MDF can provide constraints on the physics of the Pop III/II transition and some indications on the mass of Pop III stars. To this end we use GAMETE to follow the chemical enrichment (metals and dust) across the MW formation. We explore different mass ranges and chemical yields of Pop III stars and compare simulated and observed MDF. This part of the work has been published in de Bennassuti, Schneider, Valiante & Salvadori (2014), *MNRAS*, 445, 3039.
In Chapter 3, we investigate the role of star formation in mini-halos and its effect in shaping the Galactic halo MDF, providing robust data-driven constraints on the PopIII IMF. To this aim we use an improved version of GAMETE, to self-consistently describe the physical processes regulating star-formation in mini-halos: the poor sampling of the Pop III IMF and the effect of UV radiation. We study the effect of this new physics and of the IMF of Pop III stars on the MDF and on the properties of C-enhanced and C-normal stars. This part of the work is published in de Bennassuti, Salvadori, Schneider, Valiante (2017), *MNRAS*, 465, 926.
In Chapter 4 we study the interplay between different feedback processes along the MW formation. To this aim, we apply GAMESH to a low-resolution N-body simulation and we account for the radiative transfer of ionizing photons to follow the inhomogeneous reionization and heating of the IGM. This part of the work has been published in Graziani, Salvadori, Schneider, Kawata, de Bennassuti, Maselli (2015), *MNRAS*, 449, 3137.
In Chapter 5, we study the history of the dark and luminous MW progenitors and their role in shaping the properties of the MW. This is done by applying GAMESH to a higher resolution simulation which allows a more detailed investigation of the MW properties, also providing a larger statistics of mini-halos and satellite galaxies. This part of the work will be published in a forthcoming paper.
Finally, in Chapter 6 we present the main conclusions of the work.

1

The first stars

When the first stars appeared the Universe was only made by neutral hydrogen and helium gas, with small traces of Lithium and Beryllium. Thus, the first stars, usually referred as Population III (Pop III) stars formed out of metal-free gas, which collapses and fragments inside the first virialized structures: low mass dark matter (DM) mini-halos. Since the primordial composition of the gas does not provide efficient cooling, Pop III stars are predicted to be typically more massive than Population II (Pop II) and Population I (Pop I) stars observed in the Local Universe. Once the first stars evolve, they enrich the surrounding medium with metal and dust grains, providing new cooling channels, thus enhancing the gas fragmentation and possibly triggering the formation of low-mass stars. The change of the cooling properties of the gas leads to a transition from massive metal-free Pop III stars to normal Pop II stars.
So far zero-metallicity stars have never been observed, indirectly confirming the massive nature of short-lived Pop III stars. Yet, the properties of elusive Pop III stars can be inferred by measuring the chemical imprint they left in ancient low-mass stars, which form in gaseous environments polluted by their nucleosynthetic products.

In this Chapter, we describe how the first DM halos form starting from primordial density fluctuations (Sec. 1.1). In Sec. 1.2 we introduce the process of star formation, with particular attention to primordial gas cooling and the properties of the first stars. In Sec. 1.3 we summarize the main feedback processes (mechanical, radiative and chemical) which can act both positively and negatively on star formation. In particular, we will focus on the role of metals and dust in driving the transition between Pop III and Pop II stars. Finally, in Sec. 1.4 we will present the state-of-the art of current observations of metal-poor stars in the Galactic halo, mainly focusing on their Fe and C abundances which provide important constraints on the properties of the first stars.

1.1 Hierarchical structure formation

The parameters defining the commonly adopted Λ Cold Dark Matter (ΛCDM) cosmological model are: the adimensional density of the universe, $\Omega_0 = \Omega_m + \Omega_\Lambda$ (where Ω_m and Ω_Λ are the contribution from matter and vacuum, respectively), the Hubble constant, $H_0 = 100\ h$

km s^{-1} Mpc^{-1}, the adimensional baryon density, Ω_b, the rms mass fluctuations on 8 h^{-1} Mpc scale, σ_8, and the spectral index of the primordial density fluctuation, n_s.

Recent constraints on these cosmological parameters have been set by observations of the Cosmic Microwave Background (CMB) with the Planck satellite [1] (Planck Collaboration et al., 2014), with best fit values of $h_0 = 0.67$; $\Omega_b\, h^2 = 0.022$; $\Omega_m = 0.32$; $\Omega_\Lambda = 0.68$; $\sigma_8 = 0.83$; $n_s = 0.96$.

Throughout this Thesis we will adopt these cosmological parameters, unless specified.

1.1.1 Linear gravitational growth

The commonly adopted theory for structure formation is the gravitational instability scenario, in which primordial density perturbations grow through gravitational Jeans instability to form all the structures we observe today. The most favored model for the origin of these perturbations is inflation. In this scenario, the universe expands exponentially for a brief period of time at early epochs (t $\approx$ 10^{-35} – 10^{-33} s). While at the end of this period it appears to be highly homogeneous on large scales, actually it is locally perturbed due to quantum fluctuations. In what follows the evolution of these primordial density fluctuations into the first bound objects (usually called DM halos) is described. Considering the universe as a collisionless DM and baryons fluid, with a mean mass density $\bar{\rho}$, the time- and position-dependent mass density can be written as $\rho(\mathbf{x}, t) = \bar{\rho}(t)[1 + \delta(\mathbf{x}, t)]$, where $\mathbf{x}$ is the comoving spatial coordinates and $\delta(\mathbf{x}, t)$ is the mass density contrast. The time evolution equation for δ during the linear regime ($\delta \ll 1$) reads (Peebles, 1993):

$$\ddot{\delta}(\mathbf{x}, t) + 2H(t)\dot{\delta}(\mathbf{x}, t) = 4\pi G\bar{\rho}(t)\delta(\mathbf{x}, t) + \frac{c_s^2}{a(t)^2}\nabla^2\delta(\mathbf{x}, t) \tag{1.1}$$

where c_s is the sound speed, $a(t)$ is the scale factor describing the Universe expansion, $H(t) = H_0[\Omega_m(1+z)^3+\Omega_\Lambda]^{1/2}$ is the time dependent Hubble parameter and G is the universal gravitational constant. The second term on the left hand side of Eq. 1.1 represents the effect of cosmological expansion. This, together with pressure support (second term on the right hand side) acts against the growth of the perturbation driven by the gravitational collapse (first term on the right hand side). While pressure in the baryonic gas is due to collisions, the pressure term of collisionless DM comes from the readjustment of particle orbits. The total density contrast can be described in the Fourier space as a superposition of modes with different wavelengths:

$$\delta(\mathbf{x}, t) = \int \frac{d^3k}{(2\pi)^3}\delta_{\mathbf{k}}(t)exp(i\mathbf{k}\cdot\mathbf{x}), \tag{1.2}$$

[1] http://www.cosmos.esa.int/web/planck

where **k** is the comoving wave number of the Fourier series. The evolution of the single Fourier components is then given by:

$$\ddot{\delta}_{\mathbf{k}} + 2H\dot{\delta}_{\mathbf{k}} = \left(4\pi G\bar{\rho} - \frac{k^2 c_s^2}{a^2}\right)\delta_{\mathbf{k}}. \tag{1.3}$$

When the pressure and gravitational forces cancel, a critical length, the Jeans length λ_J (Jeans, 1928), is naturally introduced and it is defined as:

$$\lambda_J = \frac{2\pi a}{k_J} = \left(\frac{\pi c_s^2}{G\bar{\rho}}\right)^{1/2}. \tag{1.4}$$

If $\lambda \gg \lambda_J$ the pressure term is negligible because the time related to the pressure term is much longer with respect to the time of the density contrast growth, and the zero pressure solutions apply. On the other hand, if $\lambda < \lambda_J$ the pressure force counteracts gravity and the density contrast oscillates as a sound wave. Along with the Jeans length, also a Jeans mass (M_J) can be defined, as the mass within a sphere of radius $\lambda_J/2$:

$$M_J = \frac{4\pi}{3}\bar{\rho}\left(\frac{\lambda_J}{2}\right)^3. \tag{1.5}$$

In a perturbation with mass greater than M_J the pressure force is not counteracted by gravity and the structure collapses. Thus M_J sets a threshold for the scales which can collapse. Given the initial power spectrum of perturbations, $P(k) \equiv\mid \delta_{\mathbf{k}} \mid^2$, the evolution of each mode can be followed through Eq. 1.3 and then integrated to recover the global spectrum at any time. In particular the power spectrum predicted by the inflationary theory is $P_{in}(k) \propto k^{n_s}$, with $n_s =$ 1. This value corresponds to Gaussian random perturbations, and neither small nor large scales dominate. Although the initial power spectrum is a pure power-law, perturbation growth results in a modified final power spectrum. In fact, while on large scales the power spectrum follows a simple linear evolution, on small scales it changes shape due to the additional non-linear gravitational growth of perturbations and it results in a bended spectrum, $P(k) \propto k^{n_s-4}$. The amplitude of the power spectrum, however, is not specified by current models of inflation and must be determined observationally.

The power spectrum is given by:

$$P(k) = P_{in}(k)T(k)^2 = Ak^{n_s}T(k)^2, \tag{1.6}$$

where A is a normalization constant that is fixed through observations and $T(k)$ is the transfer function. A good fit for $T(k)$ is given by (Bardeen et al., 1986):

$$T(k) = \frac{ln(1+2.34q)}{2.34q}\left[1 + 3.89q + (16.1q)^2 + (5.46q)^3 + (6.71q)^4\right]^{-1/4}, \tag{1.7}$$

where $q = (k/h\Gamma)$ Mpc^{-1} and Γ is the shape parameter introduced by Sugiyama (1995), in order to account for the effects of the non-zero baryonic density:

$$\Gamma = \Omega_0 h e^{-\Omega_b(1+\sqrt{2h}/\Omega_0)}. \tag{1.8}$$

In order to determine the formation of objects of a given size and mass, it is useful to consider the statistical distribution of the smoothed density field. Using a normalized window function $W(\mathbf{y})$ so that $\int d^3\mathbf{y}W(\mathbf{y}) = 1$, the smoothed density perturbation field $\int d^3\mathbf{y}\delta(\mathbf{x}+\mathbf{y})W(\mathbf{y})$ follows a gaussian distribution with zero mean. By choosing a spherical top-hat window function, i.e. $W(kR) = 4\pi R^3[(sin(kR) - kRcos(kR))/(kR)^3]$, where $W = 1$ within a sphere of radius R and $W = 0$ outside, the smoothed perturbation field measures the mass fluctuation, δ_M, in a sphere of radius R (Barkana & Loeb, 2001). The mass variance σ_M is defined as the root-mean square of the density fluctuation:

$$\sigma_M^2 = \delta_M^2 = \frac{1}{2\pi}\int_0^\infty dkP(k)W^2(kR)k^2. \tag{1.9}$$

This function allows to estimate the abundance of collapsed objects. The normalization constant of the initial power spectrum, A, is specified by the value of $\sigma_8 = \sigma_M$(R=8/h Mpc). There are several methods to constrain σ_8, which rely on different observables. For instance it can be determined by galaxy-galaxy correlations (e.g. Tegmark et al., 2004; Cole et al., 2005), fluctuations in the CMB (Spergel et al., 2003, 2007; Komatsu et al., 2009), gravitational lensing statistics (e.g. Hoekstra et al., 2006; Benjamin et al., 2007; Kitching et al., 2007), cluster mass function (e.g. White et al., 1993; Bahcall & Fan, 1998; Reiprich & Böhringer, 2002; Wen et al., 2010), Ly-α forest (Jena et al., 2005; McDonald et al., 2005) and galaxy peculiar velocities (Feldman et al., 2003). Since most of the power of the spectrum is on small scales, in standard ΛCDM models low mass objects are those predicted to collapse first.

1.1.2 Non-linear objects

DM is made of collisionless particles that interact very weakly with matter and radiation. Hence the DM density contrast starts to grow at early times. Once the density contrast scale becomes non-linear (i.e. $\delta \approx 1$), the linear perturbation theory described in the previous section does not apply anymore. In fact the self-gravity of the local mass concentration causes an expansion at a slower rate compared to the background Universe resulting in the collapse and formation of bound objects. Zel'dovich (1970) proposed a simple approximation to describe the non-linear growth of perturbations, which has been confirmed by numerical simulations to be accurate during the early phase of non-linear collapse, and not accurate at later times. The simplest model is the one of a spherically symmetric, constant density region, for which the collapse can be followed analytically. The initial overdensity δ grows according to the linear theory. At a certain point the region reaches a maximum radius of expansion, then it turns around and starts to contract under the effect of self-gravity, ideally collapsing into a point. Before this happens, DM experiences a relaxation process quickly reaching the virial equilibrium. If z is the redshift at which this condition is achieved, a DM halo with total mass M can be described in terms of its virial radius, r_{vir}, circular velocity, $v_c = \sqrt{GM/r_{vir}}$, and gas virial temperature, $T_{vir} = \mu m_p v_c^2/2k_B$, whose expressions are (Barkana & Loeb, 2001):

$$r_{vir} = 0.784\left(\frac{M}{10^8 h^{-1} M_\odot}\right)^{1/3}\left[\frac{\Omega_m}{\Omega_m(z)}\frac{\Delta_c}{18\pi^2}\right]^{-1/3}\left(\frac{1+z}{10}\right)^{-1} h^{-1}\mathrm{kpc}, \tag{1.10}$$

$$v_c = 23.4\left(\frac{M}{10^8 h^{-1} M_\odot}\right)^{1/3}\left[\frac{\Omega_m}{\Omega_m(z)}\frac{\Delta_c}{18\pi^2}\right]^{1/6}\left(\frac{1+z}{10}\right)^{1/2} \mathrm{km\,s^{-1}}, \tag{1.11}$$

$$T_{vir} = 2\times 10^4\left(\frac{\mu}{0.6}\right)\left(\frac{M}{10^8 h^{-1} M_\odot}\right)^{2/3}\left[\frac{\Omega_m}{\Omega_m^z}\frac{\Delta_c}{18\pi^2}\right]^{1/3}\left(\frac{1+z}{10}\right)\mathrm{K}, \tag{1.12}$$

where μ is the mean molecular weight of the gas[2], m_p is the proton mass,

$$\Delta_c = 18\pi^2 + 82(\Omega_m(z) - 1) - 39(\Omega_m(z) - 1)^2, \tag{1.13}$$

and:

$$\Omega_m(z) = \frac{\Omega_m(1+z)^3}{\Omega_m(1+z)^3 + \Omega_\Lambda}. \tag{1.14}$$

Since spherical collapse provides only an approximate description of the physics of the halo formation, to study their inner structure numerical simulations should be used. Navarro et al. (1996, 1997) simulated the formation of DM halos in a broad range of masses, finding a universal shape for the density profile, independent of halo mass, initial density fluctuation spectrum and cosmological parameters:

$$\rho(r) = \frac{\rho_s}{(r/r_s)(1 + r/r_s)^2}, \tag{1.15}$$

where ρ_s and r_s are characteristic density and radius. This parametrization of the DM density profile is usually referred to as NFW (Navarro, Frenk & White) profile. The quantity $c \equiv r_{vir}/r_s$ represents the concentration parameter. As ρ_s can be written in terms of c, the above equation is a one-parameter form.

[2] The value of μ depends on the ionization fraction of the gas: μ=0.59 for a fully ionized primordial gas, μ=0.61 for a gas with ionized hydrogen but only singly-ionized helium, and μ=1.22 for neutral primordial gas.

Although there is no convergence towards a universal shape of the halo density profile, the density of DM halos and their spatial distribution are better known. Two main methods have been proposed to study these halo properties: numerical simulations solving the equations of gravitational collapse, and analytical methods that approximate these results with simple functions. The advantage of using numerical simulations is that they give the spatial information on halos, but analytical techniques are extremely useful as they are much faster and allow the analysis of a wide range of parameters. One of the most popular analytical method applied to the problem of structure formation has been developed by Press & Schechter (1974): the abundance of halos at a redshift z is determined from the linear density field by assuming a spherical collapse to associate peaks in the field with virialized objects in a full non-linear treatment. This model, has later been improved (Extended Press Schechter, EPS) by Bond et al. (1991) and Lacey & Cole (1993). The method provides the comoving number density of halos, dn, with mass between M and $M + dM$ as (Peebles 1993):

$$\frac{dn}{dM} = \sqrt{\frac{2}{\pi}} \frac{-d(ln\sigma_M)}{dM} \frac{\rho_m}{M} \nu_c e^{-\nu_c^2/2}, \tag{1.16}$$

where ρ_m is the present-day mean mass density, σ_M is the mass variance (see Eq. 1.9) and ν_c is the minimum number of standard deviations of a collapsed fluctuation (i.e. $\nu_c = \delta/\sigma_M$).
The EPS formalism is in relatively good agreement with numerical results, although Sheth & Tormen (1999) showed that the agreement is worse for halos with $\nu_c \lesssim 2$, which appear to be more clustered, and for those with $\nu_c \gtrsim 10$, which are less clustered.

1.2 Gas fragmentation and star formation

In contrast to DM, as long as the gas is fully ionized, the radiation drag on free electrons prevents the formation of gravitationally bound systems. The ionized gas gradually combines into neutral atomic hydrogen. When the electron fraction drops below 0.1, recombination occurs. This epoch corresponds to $z_{rec} \approx 1250$. The residual ionization keeps the gas temperature locked to the CMB temperature through Compton scattering, down to a redshift $1 + z_t \propto 1000(\Omega_b h^2)^{2/5}$ (Peebles, 1993). Hence the neutral matter decouples from the radiation and baryonic perturbations grow in the pre-existing DM halo potential wells forming the first baryonic bound objects within DM halos. The virialization process is similar for baryons and for DM: during the contraction the gas is reheated due to shocks to a temperature where pressure is sufficient to balance the collapse. The mass of these first bound objects can be derived from Eqs. 1.4 and 1.5, where c_s is the velocity of the baryonic gas. In particular, at $z > z_t$ the Jeans mass does not depend on time, while at $z < z_t$, when the gas temperature adiabatically decreases, M_J decreases with decreasing redshift:

$$M_J = 3.08 \times 10^3 \left(\frac{\Omega_m h^2}{0.13}\right)^{-1/2} \left(\frac{\Omega_b h^2}{0.022}\right)^{-3/5} \left(\frac{1+z}{10}\right)^{3/2} M_\odot \tag{1.17}$$

Since the determination of this Jeans mass is based on a perturbative approach, it can only describe the initial phase of the collapse, when the linear theory holds true.

In order to have the collapse into a bound object, the condition $M > M_J$ is not sufficient. To allow the collapse to occur the cooling time must be shorter than the Hubble time. In addition the dynamical and chemical evolution of the collapsing gas must then be derived in detail to assess if star formation can be triggered.
In the standard cosmological hierarchical scenario for structure formation, the objects which collapse first are predicted to have masses corresponding to virial temperatures $T_{vir} < 10^4$ K. For a gas of primordial composition at such low temperatures the main coolant is molecular hydrogen H_2, which is then crucial for the formation of the first stars. Primordial H_2 forms with a fractional abundance of $f_{H_2} \approx 10^{-7}$ at redshifts $\gtrsim 400$ via the H_2^+ formation channel. But at redshifts $\lesssim 110$ the CMB radiation becomes so weak to allow the formation of H^- ions and more H_2 molecules can be formed through the following formation channel:

$$\mathrm{H} + \mathrm{e}^- \rightarrow \mathrm{H}^- + \mathrm{h}\nu$$
$$\mathrm{H}^- + \mathrm{H} \rightarrow \mathrm{H}_2 + \mathrm{e}^-$$

Due to the lack of molecular data, it has unfortunately not been possible to follow the details of the H_2^+ chemistry as its level distribution decouples from the CMB. Assuming the rotational and vibrational states of H_2^+ to be in equilibrium with the CMB, the H_2^+ photo-dissociation rate is much larger than the one obtained by considering only photo-dissociations out of the ground state. Conservatively, one concludes that these two limits constrain the H_2 fraction to be in the range $10^{-6} - 10^{-4}$ (e.g. Lepp & Shull, 1984; Palla et al., 1995; Haiman et al., 1996; Tegmark et al., 1997). If we assume that the H^- channel for H_2 formation is the dominant mechanism, i.e. that the H_2^+ photo-dissociation rate at high redshift is close to its equilibrium value, this leads to a typical primordial H_2 fraction of $f_{H_2} \approx 2 \times 10^{-6}$ (Anninos & Norman, 1996). Accounting for other effects in the formation of H_2, slightly different values of f_{H_2} are found (Hirata & Padmanabhan, 2006) with no particular influence on the cooling. Thus, the fate of a virialized gas cloud depends crucially on its ability to rapidly increase its H_2 content during the collapse phase. Haiman et al. (1996) followed the growth of spherical perturbations into the non-linear regime, finding that H_2 cooling becomes important only after virialization. In addition, Tegmark et al. (1997) estimated the evolution of the H_2 abundance in halos with different masses and cosmological conditions finding for each virialization redshift there is a critical mass, M_{sf}, such that only protogalaxies with total mass $M > M_{sf}$ will be able to collapse and form stars. At $z \approx 20$ they found $M_{sf} \approx 10^6 M_\odot$ or $T_{vir} \approx 10^3$ K.

Once the typical mass scale given by the Jeans mass is formed due to the cooling and fragmentation of the gas cloud, the collapse of each fragment proceeds leading to the formation of a hydrostatic core at the center. The final mass of the star strongly depends on the accretion process of the surrounding gas on the central core. Accretion histories normally are highly variable, resulting in short accretion bursts (exceeding $0.01 M_\odot$/yr) followed by relatively long

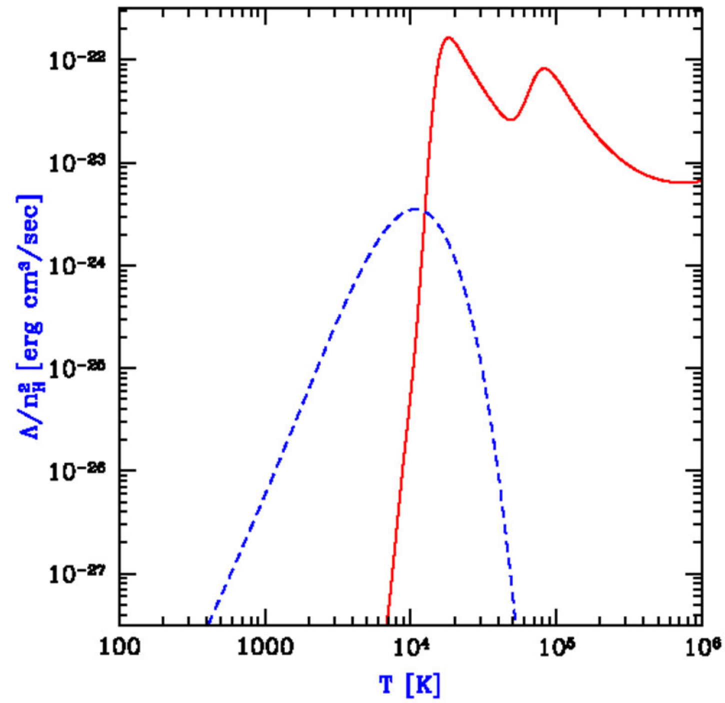

Figure 1.1 *Cooling rates as a function of temperature for a primordial gas composed of atomic hydrogen and helium, as well as molecular hydrogen, in the absence of any external radiation. We assume a hydrogen number density* $n_H = 0.045\,\mathrm{cm}^{-3}$ *and a molecular abundance equal to 0.1% of* n_H*. The red solid (blue dashed) line shows the cooling curve for an atomic (molecular) gas.*

quiescent phases (e.g. Smith et al., 2012; Vorobyov et al., 2013; DeSouza & Basu, 2015; Sakurai et al., 2016).

In general (e.g. Schneider et al., 2002), cooling is efficient when the cooling time is much shorter than the free-fall time, i.e. $t_{cool} \ll t_{ff}$, where $t_{cool} = 3nkT/\Lambda(n,T)$ and $t_{ff} = (3\pi/32G\rho)^{1/2}$, n is the gas number density while ρ is the gas mass density, and $\Lambda(n,T)$ is the net radiative cooling rate (in units of erg cm^{-3} s^{-1}). In Fig. 1.1 (Barkana & Loeb, 2001) we show the temperature evolution of the $\Lambda(n,T)/n^2$ function for a primordial gas. As it can be noted, a sharp transition occurs at $T \approx 10^4$ K: the dominant cooling is given by molecules (H_2, HD) if the temperature is $T \lesssim 10^4$ K (blue dashed line), while at higher temperatures it is dominated by atomic H, which is much more efficient (red solid line). The condition on cooling/free-fall timescales ($t_{cool} \ll t_{ff}$) can be translated into the unbalance between gravitational contraction and radiative losses, leading to the fragmentation of the gas. The typical length scale of the fragments is $R_F \approx \lambda_J \propto c_s t_{ff}$ where the sound speed $c_s \propto T^{1/2}$. Since c_s varies on the cooling timescale, the corresponding R_F becomes smaller as T decreases and the gas fragments into smaller and smaller pieces.

In Fig. 1.2 we show the gas distribution of a prestellar gas cloud in the temperature-density phase space, computed with a cosmological simulation with hydrodynamics and chemistry (Yoshida

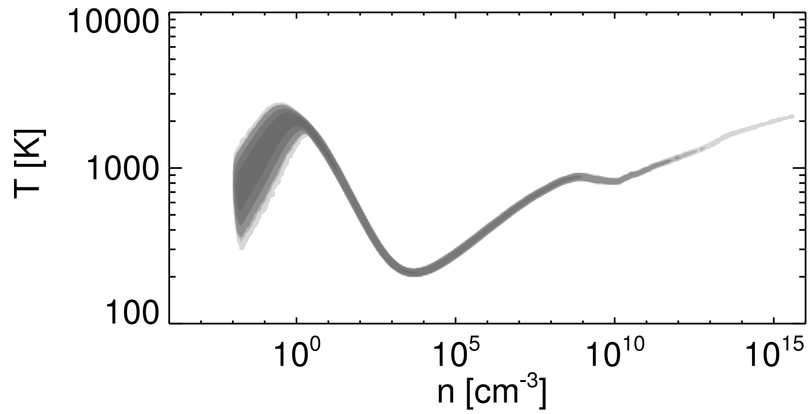

Figure 1.2 *Distribution of gas in the temperature-density phase plane for a primordial composition gas cloud, when the central density of the cloud is* $5 \times 10^{15}\mathrm{cm}^{-3}$.

et al., 2006). The gas cloud can cool and fragment if its temperature-density conditions are close to a temperature minimum, and the characteristic fragmentation mass is given by the Jeans mass related to those conditions. For a metal-free gas, the temperature minimum occurs around a density $n \sim 10^4$ cm^{-3}, at $T \sim 200$ K, as shown in Fig. 1.2. In these conditions the fragmentation mass scale is $\sim 10^3 M_\odot$.

This hierarchical fragmentation process comes to an end when cooling becomes inefficient because (*i*) the critical density for Local Thermodynamical Equilibrium (LTE) is reached or (*ii*) the gas becomes optically thick to cooling radiation. In both cases, t_{cool} becomes larger than t_{ff}. At this stage, the temperature cannot decrease any further and it either remains constant (if energy deposition by gravitational contraction is exactly balanced by radiative losses) or it increases. The necessary condition to stop fragmentation and start gravitational contraction within each fragment is that the Jeans mass does not decrease any further, thus favoring fragmentation into sub-clumps. This happens when $t_{cool} \gg t_{ff}$.

1.2.1 Pop III initial mass function

The stellar initial mass function (IMF) of the first stars, i.e. the mass distribution of Pop III stars at their formation, is of fundamental importance in determining the properties of the first galaxies and how they evolve with time.

Recently, Hirano et al. (2014) used radiation-hydrodynamic simulations that followed the growth of a primordial protostar (Hosokawa et al., 2011) to investigate the influence of radiation in a sample of 110 different mini-halos that were extracted from 3D cosmological simulations. They found final stellar masses in the range $\sim$ [10-1000] $M_\odot$ which are correlated with the thermal evolution of the gas during the initial collapse phase. Fig. 1.3 (Hirano et al., 2014) shows the distribution of the final stellar masses obtained in their simulations. The resulting stellar masses

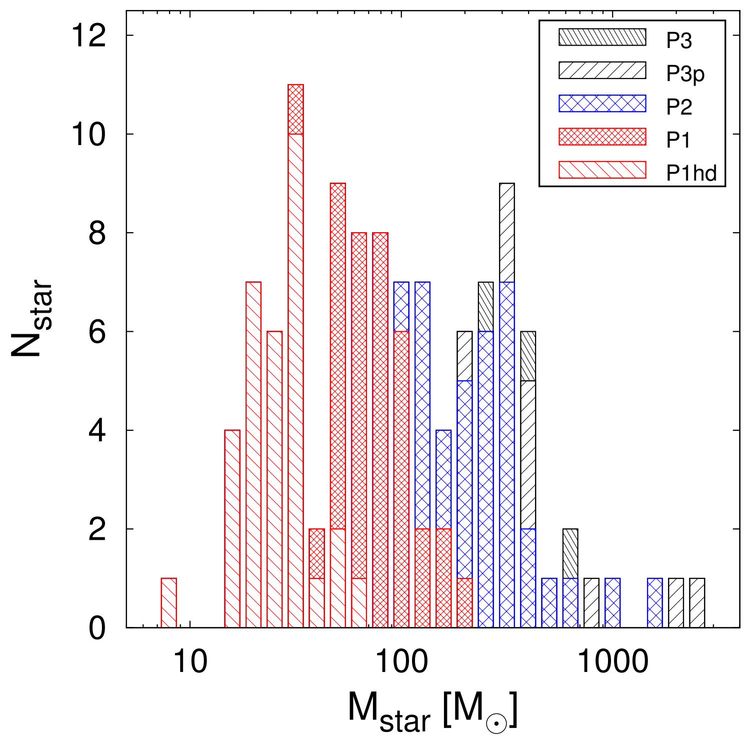

Figure 1.3 *IMF of Pop III according to the 2D radiation hydrodynamics simulations of Hosokawa et al. (2011), applied to 110 different mini-halos. The red, blue, and black histograms represent the different paths of proto-stellar evolution: P1 denotes Kelvin-Helmholtz contracting proto-star (red), P2 an oscillating proto-star (blue), and P3 super-giant proto-star (black). P1hd refers to the cases in which the gas clouds are formed by HD cooling and evolve on low-temperature tracks. P3p (predicted) indicates the same cases as P3, except that the final masses are calculated from a correlation between the properties of the cloud and the resulting stellar mass. Adapted from Hirano et al. (2014).*

are largely scattered, ranging from $\sim 10M_{\odot}$ to $\gtrsim 1000M_{\odot}$. The bulk of stars is distributed around several 10s or a few 100s of solar masses. In a subsequent work, Hirano et al. (2015) studied the redshift evolution of the Pop III IMF, finding that it changes from a single peak function at high redshifts ($z \gtrsim 14$) to a bimodal function for lower redshifts.

In addition, high-resolution simulations suggest the possibility to form low-mass stars (Stacy et al., 2010; Clark et al., 2011; Greif et al., 2011, 2012; Stacy et al., 2016). The gas infall onto the central proto-star is eventually limited by radiative feedback (McKee & Tan, 2008; Hosokawa et al., 2011; Stacy et al., 2012; Susa, 2013; Susa et al., 2014), resulting in stars with final masses of the order of a few tens of solar masses. Indeed, Susa (2013) and Susa et al. (2014) found that most Pop III stars had final masses in the range $10M_{\odot} \lesssim m_{*} \lesssim 100M_{\odot}$ due to the photo-dissociating radiation from the central proto-star which can suppress the accretion. Hosokawa et al. (2016) use stellar evolution models and 3D radiation-hydrodynamic simulations to study the evolution of primordial proto-stars along their dynamic accretion history under the influence

of stellar ionizing and dissociating UV feedback, resulting in a wide diversity of final stellar masses, covering $10M_\odot \lesssim m_* \lesssim 10^3 M_\odot$. In fact, Omukai & Palla (2003) already found that in a metal-free gas the accretion rate can be as high as $4 \times 10^{-3} M_\odot$/yr, giving rise to a proto-star with final mass $\sim 300M_\odot$ (see also Hosokawa & Omukai 2009).
However, if the proto-stellar disk is unable to transfer gas onto the proto-star fast enough with respect to the accretion rate, it becomes gravitationally unstable. This allows the disk to further fragment and to form stars with masses down to subsolar values (Stacy et al., 2016). In addition, the presence of magnetic field would also affect the accretion process, preventing the formation of a stable proto-stellar disk (Turk et al., 2012; Machida & Doi, 2013; Peters et al., 2014).
In spite of all this theoretical effort, up to now a complete description of the formation of Pop III stars with 3D simulations, high resolution and a detailed treatment of radiative transfer is still missing. For instance, the simulations of Hosokawa et al. (2011) and Hirano et al. (2014) were limited to two dimensions, although including a very detailed treatment of radiative transfer. On the other side, the 3D simulations of Stacy et al. (2012), Susa (2013) and Susa et al. (2014), have limited resolution and a simplified treatment of the radiative transfer.

Another problem in determining the emerging shape of the Pop III IMF is the capability of the gas to cool and to form large enough stellar masses to sample all the possible masses. Semi-analytical models usually make the assumption of a well-populated IMF, which is correct when the total stellar mass is sufficiently large to allow the formation of a large number of stars (Pindao et al., 2002; Fumagalli et al., 2011; Eldridge, 2011). However, for "small" stellar populations the analytic description of the IMF does not hold true anymore, and the sampling of the IMF with a small number of stars may lead to significant differences, due to the possible undersampling of the less probable mass range. Examples of such "stochastic" IMF effects have been studied by various authors (e.g. Cerviño et al., 2000; Bruzual A., 2002; Cerviño & Luridiana, 2006). For small objects, such as the first galaxies, stochasticity can be important for the building of the Pop III IMF.

Due to the complexity of the physical processes described above and the limitations of current numerical simulations which cannot simultaneously capture all of them, there is still no general consensus on the IMF of primordial stars. Although still very uncertain, the most likely mass range of the Pop III IMF is [10-300] $M_\odot$.

1.2.2 Final fate of Pop III stars

Due to the lack of CNO in primordial gas, zero metallicity stars can only be powered by pp-chain, which is not sufficient to counteract the gravitational collapse allowing the central temperature to increase above 10^8 K , until C, N and O are formed through the triple-α process. Hence the final fate of primordial stars can be very different with respect to what observed for stars in the solar neighborhood. Theoretical analysis on the evolution of metal-free, non-rotating stars predict that their fate can be classified according to their mass m_* (Heger & Woosley, 2002):

- stars with $2M_\odot \lesssim m_* \lesssim 10M_\odot$, if formed, loose their envelope during Asymptotic Giant Branch (AGB) phase, characterized by thermal pulses and dredge-up events. Since these mechanisms depend on the metallicity of the star, the final mass of zero metallicity AGB stars can be different from solar composition stars.

- In the mass range $10M_\odot \lesssim m_* \lesssim 40M_\odot$ stars proceed through the entire series of nuclear burnings from hydrogen to iron. When the star has built up a large enough iron core, exceeding its Chandrasekhar mass, it collapses, followed by a "core-collapse" supernova (SN) explosion with typical energies of 10^{51} erg (Woosley & Weaver, 1995). Stars in this mass range can also evolve as "faint" SNe if during their evolution experience mixing and fallback. In this case, although the explosion energy is similar to that of ordinary core-collapse SNe, the stars release an extremely small amounts of Fe with respect to light elements such as C (e.g. Bonifacio et al., 2003; Umeda & Nomoto, 2003; Iwamoto et al., 2005; Tominaga et al., 2007; Marassi et al., 2014; Ishigaki et al., 2014).

- For stars of $40M_\odot \lesssim m_* \lesssim 140M_\odot$ the neutrino-driven explosion is probably too weak to form an outgoing shock. A black hole (BH) forms and the ejected material has not a sufficient energy to escape the gravitational potential, entirely falling back on the BH possibly producing a Gamma Ray Burst (GRB; Fryer, 1999).

- Stars with $140M_* \lesssim m_* \lesssim 260M_\odot$ form large He cores that reach carbon ignition with masses in excess of about 45 $M_\odot$. It is known that after helium burning, cores of this mass will encounter the electron-positron pair instability, collapse and ignite oxygen and silicon burning explosively. If explosive oxygen burning provides enough energy, it can reverse the collapse in a giant nuclear-powered explosion (the so-called Pair Instability Supernova, PISN, with energies of the order $[10^{52} - 10^{53}]$ erg) by which the star would be completely disrupted (Fryer et al., 2001; Heger & Woosley, 2002; Heger et al., 2003; Joggerst & Whalen, 2011; Baranov et al., 2013; Chen et al., 2014, 2015).

- In more massive stars ($m_* \gtrsim 260M_\odot$) a large fraction of the center of the star becomes so hot that photo-disintegration instability occurs before explosive burning reverses the implosion, accelerating the collapse and leading to the direct formation of a massive BH (Bond et al., 1984; Fryer et al., 2001; Ohkubo et al., 2006; Suwa et al., 2007; Inayoshi et al., 2013).

This classification of the final outcome of Pop III stars assumes that stars are non rotating. Models including rotation show that metals may be mixed between nuclear burning layers and even to the surface of the star. This may have an effect on the evolution of the stars, the degree to which their elements are mixed (Meynet & Maeder, 2002; Heger et al., 2005; Hirschi et al., 2007; Ekström et al., 2008; Takahashi et al., 2014) and their final fates (Suwa et al., 2007; Joggerst et al., 2010; Chatzopoulos & Wheeler, 2012; Yoon et al., 2012; Chatzopoulos et al., 2013).
In Fig. 1.4 we show the final fate of stars according to their mass and rotational velocity, as estimated by Yoon et al. (2012). The velocity is given in units of the Keplerian velocity, v_K, and the forbidden region, i.e the upper-right part of Fig. 1.4, represents the regime where the surface

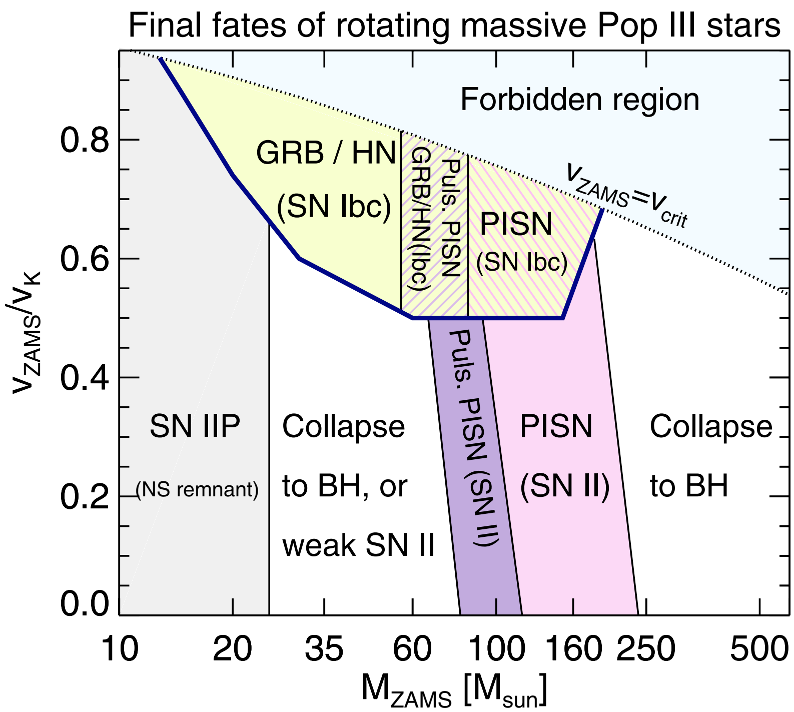

Figure 1.4 *Phase diagram for the final fates of massive Pop III stars, in the plane of the mass and the equatorial rotational velocity (in units of the Keplerian value, v_K) on the zero-age main sequence (ZAMS). The dotted line denotes the limit above which the rotational velocity at the surface would exceed the critical rotation velocity (v_{crit}). The thick solid line marks the boundary between the regimes for the chemically homogeneous evolution (CHE), and the non-CHE evolution. The regions for different final fates are divided by thin solid lines. Each acronym has the following meaning. SN IIP: Type IIP supernova, NS: neutron star, BH: black hole, SN II: type II supernova, PISN: pair-instability supernova, Puls. PISN: pulsational pair-instability supernova, GRB: gamma-ray bursts, HN: hypernova, SNIbc: type Ib or Ic supernova.*

rotational velocity exceeds the critical limit, v_{crit} [3]: any star in this region would be unstable, experiencing mass eruption, and forced to come back to the regime of sub-critical rotation. As it can be seen, by increasing the rotational velocity (i.e. by moving upward) the PISN mass range is gradually shifted to lower masses, because the helium core mass increases with rotation. Indeed, the onset of a PISN depends on whether the star can retain enough of its initial mass to have a helium core bigger than about 64 $M_\odot$ at the end of the core He-burning phase, or rather lose the mass during the previous stages of its evolution (Meynet et al., 2006).

In conclusion, the main nucleosynthetic contribution by Pop III stars at the end of their lives, is given by AGB stars, SNe (either core-collapse or faint) and PISNe. In addition, since the rotational velocity of primordial stars is unknown, in this work we will consider non-rotating stars.

[3] See Yoon et al. (2012) for a detailed determination of v_K and v_{crit}.

1.3 Feedback processes

Once the first stars have formed, they can affect the subsequent galaxy and star formation process through the so-called "feedback" effects. Usually feedback processes are divided in three classes: radiative (related to the emission of photons by stellar sources), mechanical (related to the energy produced by SN-driven winds) and chemical (related to the production of metals and dust from stars). In what follows, the different types of feedback will be discussed.

1.3.1 Radiative feedback

Radiative feedback is related to the radiation emitted by stars. This radiation can have local effects (i.e. on the same galaxy that produces it) or long-range effects, hence affecting the formation and evolution of nearby objects or joining the radiation produced by other galaxies to form a background. In particular photons emitted at energies $E > 13.6$ eV are responsible for the hydrogen ionization in the interstellar medium, while slightly less energetic photons in the Lyman-Werner band (LW, 11.2 eV $< E <$ 13.6 eV) can photo-dissociate the H_2 molecule, which represents the main coolant in mini-halos at high redshift (see Sec. 1.2).

Proto-stellar radiation
As discussed in Sec. 1.2.1, star formation in primordial gas can be affected by gas accretion onto the central proto-star and/or by disk fragmentation. However, in the presence of (internal or external) heating sources, the disk accretion may be stabilized, thus leading to a single star at the center. While proto-stellar feedback is insufficient to stabilize the disk, possibly delaying its fragmentation (Smith et al., 2011, 2012), it is possible that an external heating source could serve to stabilize the disk and prevent fragmentation. One promising source of such an external background is the radiation in the LW bands: if below a critical threshold, it can heat the disk without suppressing star formation (Dijkstra et al., 2008). Indeed, Susa (2013) and Susa et al. (2014) show that mass accretion onto the star is halted by including the effect of photo-dissociating radiation in their 3D simulations. Also DM annihilation has been proposed as a possible heating source (Ripamonti et al., 2010; Smith et al., 2012): while such heating is unable to suppress star formation, it does serve to stabilize the disk, suppressing fragmentation for a while (Stacy et al., 2012, 2014). Moreover, cosmic X-rays from massive stars in high-mass X-ray binaries (e.g. Clark et al., 2011; Greif et al., 2012; Mirocha, 2014) and possibly from mini-quasars as well (Kuhlen & Madau, 2005; Jeon et al., 2012, 2014) can heat and increase the ionization fraction of gas in neighboring mini-halos (Hummel et al., 2015, 2016).

H_2 Photo-dissociation
Since the density of intergalactic H_2 is extremely low, it is easily photo-dissociated and a UV background in the LW band can rapidly build up, having a negative feedback on the gas cooling and star formation inside smaller halos (Haiman et al., 1997; Ciardi et al., 2000a,b; Haiman et al., 2000; Ricotti et al., 2002; Mackey et al., 2003; Yoshida et al., 2003; Wise & Abel, 2008; Johnson et al., 2008). In addition to this external background, the subsequent star formation process is

also affected by internal dissociating radiation from the first generation of stars formed in a given halo (Omukai & Nishi, 1999; Nishi & Tashiro, 2000; Glover & Brand, 2001; Oh & Haiman, 2002). For example, O'Shea & Norman (2007) showed that the formation of stars in low-mass mini-halos is delayed in the presence of a LW flux, resulting in an increased virial mass of the halo at the time of the collapse. Nishi & Tashiro (2000) found that this feedback has stronger effects at lower metallicities (i.e. $Z < 10^{-2.5} Z_{\odot}$). However, dense H_2 regions can self-shield against the external radiation, with a consequent gas fragmentation and star formation also in presence of dissociating radiation (e.g. Susa & Umemura, 2004, 2006). More recently, Valiante et al. (2016) investigated the formation of super massive BHs at $z > 6$ and they evaluated the mini-halo star formation efficiency as function of (*i*) the halo virial temperature, (*ii*) the halo formation redshift, (*iii*) the gas metallicity and (*iv*) the LW flux ($J_{\rm LW}$) which illuminates the halo (Omukai, 2012). In their Appendix A they clearly show the effect of a photo-dissociating flux in suppressing the fraction of cold gas which can be converted into stars, also accounting for H_2 self-shielding. The negative feedback of photo-dissociating radiation can be counterbalanced by H_2 re-formation, as analyzed by several authors (Ferrara, 1998; Ricotti et al., 2001, 2002; Mashchenko et al., 2006; Abel et al., 2007; Johnson et al., 2007).
In conclusion, many studies agree that the absolute minimum mass allowed to collapse is as low as $10^5 M_{\odot}$ (Abel et al., 2000; Machacek et al., 2001; Reed et al., 2005; O'Shea & Norman, 2007), the minimum mass for star formation (M_{sf}, Sec. 1.2) in $T_{vir} < 10^4$ K halos critically depends not only on the cooling physics and chemical network adopted for H_2 formation (Fuller & Couchman, 2000), but also on H_2 photo-dissociation due to radiative feedback effects. As soon as DM halos reach $T_{vir} > 10^4$ K, furthermore, the gas cooling becomes more efficient, being mostly driven by atomic H and eventually by the metals produced by stars.

Photo-evaporation
The UV radiation can also affect the formation of the first stars in low DM halos. Indeed, UV photons can heat the gas inside these small systems, eventually photo-evaporating them. Yet, also in this case the results are not simple and depend on the competitive interplay between different physical processes. Susa & Kitayama (2000) and Kitayama et al. (2000, 2001) found that the gas can self-shield from the radiation, allowing the collapse also in small objects. The problem has been extensively studied by several authors, exploring the feedback effects of the ionizing radiation, finding that the UV background can delay the formation of low mass objects (Susa & Umemura, 2004) but at $z > 10$ the collapse of halos as small as $v_c \approx 10$ km/s can proceed due to collisional cooling and to the low intensity of the radiation (Dijkstra et al., 2004). Alvarez et al. (2006) found that mini-halos can survive photo-evaporation if the lifetime of stellar sources are shorter than the typical evaporation time, and Whalen et al. (2008) studied the dependence of the photo-evaporation process on the density, finding that the lower is the central density, the larger is the probability for the halo to be photo-evaporated.

Photo-heating
In addition to the photo-evaporation effect, UV photons that are responsible for the (re)ionization of the intergalactic medium (IGM) do also heat the IGM up to $T > 10^4$ K, thus preventing gas accretion in $T_{vir} < 10^4$ K mini-halos (e.g. Gnedin, 2000; Hoeft et al., 2006; Okamoto et al.,

2008, 2010). Okamoto et al. (2008) performed high-resolution cosmological hydrodynamical simulations with an imposed, spatially uniform but time-dependent UV background. They found that accretion onto a given halo is suppressed if the accreting gas from the IGM is hotter than the virial temperature of the halo itself.
Noh & McQuinn (2014) developed a theoretical model to study how the interplay between gravity, pressure, cooling and self-shielding can set the redshift dependent mass scale at which halos can accrete gas. Their models show that gas accretion onto halos depends on its formation history rather than on its mass. As a result, accretion is inhibited onto more massive halos than found by previous studies.
Numerous theoretical models (e.g. Li et al., 2010; Macciò et al., 2010; Font et al., 2011) have confirmed that a combination of a UV background and feedback processes from SNe can reduce the discrepancy that exists between the number of low-mass DM halos predicted by the ΛCDM cosmological model and the number of faint satellites identified around the MW: the "missing satellite problem" (Klypin et al., 1999; Moore et al., 1999). Yet, the increasing number of newly discovered ultra-faint dwarf galaxies in the Local Group, seems to suggest that several mini-halos have successfully formed stars prior the end of reionization (e.g. Madau et al., 2008; Bovill & Ricotti, 2009, 2011; Salvadori & Ferrara, 2009, 2012; Macciò et al., 2009; Salvadori et al., 2015; Bland-Hawthorn et al., 2015).

In conclusion radiative feedback effects are crucial in regulating *the early cosmic star formation. This is especially true for mini-halos, which are likely the formation site of the first stars, and which are particularly affected by feedback processes.*

1.3.2 Mechanical feedback

SN explosions remove the gas from the galaxy, reducing the amount available for subsequent star formation events (e.g. Mac Low & Ferrara, 1999; Nishi & Susa, 1999; Ferrara & Tolstoy, 2000; Springel & Hernquist, 2003; Bromm et al., 2003; Silk, 2003; Wada & Venkatesan, 2003; Greif et al., 2007; Whalen et al., 2008; Salvadori et al., 2008). Yet, the amount of gas removed strongly depends on the number of SN explosions, their explosion energies, along with on the binding energy of the system. Mori et al. (2002) found that in a $10^8 M_\odot$ DM halo at $z \approx 9$ the fraction of SN energy converted into kinetic form is at most $\sim 30\%$, hence preventing the total blow-out of the gas and the complete quenching of star formation. On the contrary, in high-z mini-halos forming Pop III stars, Bromm & Loeb (2003) and Greif et al. (2007) found that the explosion of a single PISN can drastically reduce the gas content of the halo. Similarly, Kitayama & Yoshida (2005) and Whalen et al. (2008) used 1D calculations to investigate the evolution of SN remnants in mini-halos with various explosion energies. They found that more conventional core-collapse SNe fail to remove the gas from more massive halos, while PISNe are able to completely evacuate even the most massive halos. In addition, for such highly energetic explosions the time required for the gas to recollapse is of the order of the Hubble time (Greif et al., 2010), so that subsequent formation of stars is unlikely to occur. However, the ejected metal-enriched gas can pollute near-by mini-halos where subsequent star formation can occur (e.g. Smith et al., 2014) In the case

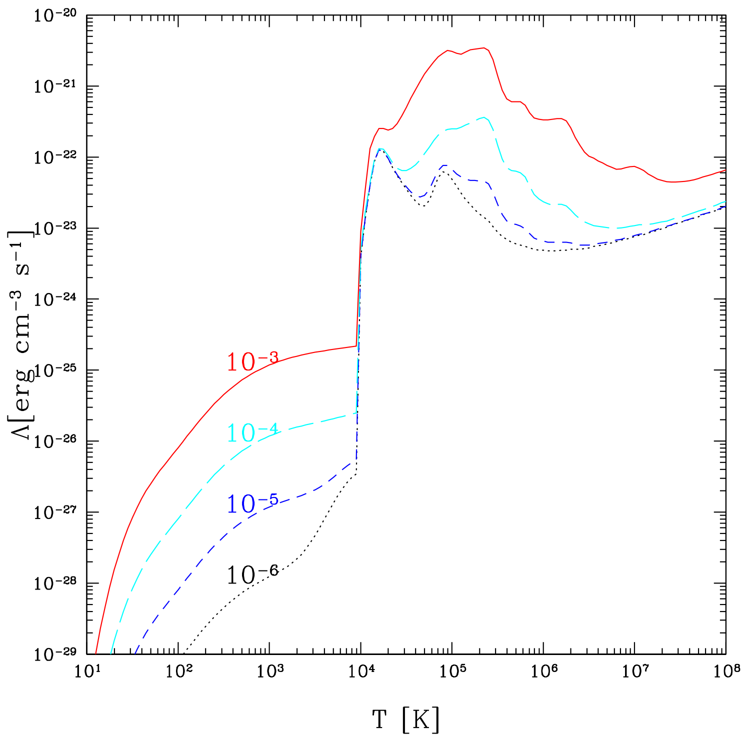

Figure 1.5 *Cooling function accounting for hydrogen, helium, metals, H_2 and HD molecules as a function of temperature, for gas having a hydrogen number density of 1 cm^{-3} (Maio et al. 2015). The fractions of H_2 and HD are fixed to 10^{-5} and 10^{-8}, respectively. The labels in the plot refer to different gas metal fraction: 10^{-3} (red solid line), 10^{-4} (cyan long-dashed line), 10^{-5} (blue short-dashed line) and 10^{-6} (black dotted line).*

of less energetic explosions, i.e. similar to standard core-collapse SNe, the collapse time is ≈10 Myr (Ritter et al., 2012), thus possibly triggering subsequent star formation events. Jeon et al. (2014) found that the re-collapse timescale is highly sensitive to the Pop III progenitor mass, and less to the halo environment. For Pop III progenitor masses from $15M_\odot$ to $40M_\odot$ in a $5\times10^5M_\odot$ mini-halo, recovery times are $\sim$ 10 Myr to $\sim$ 90 Myr. For more massive progenitors, including PISNe, second-generation star formation is delayed significantly, up to a Hubble time. Moreover, they found that second-generation stars forming in gas clouds polluted by Pop III core-collapse SNe are already metal-enriched to $\sim [2-5]\times10^{-4}Z_\odot$, thus being classified as normal Pop II stars. More recently, Ritter et al. (2016) demonstrated that extremely metal poor ($Z\sim[10^{-4}-10^{-3}]\,Z_\odot$) stars can form in a $\sim 10^6M_\odot$ cosmic mini-halo enriched by a single, low-energy core collapse SN from 60 $M_\odot$ Pop III star progenitor only ~10 Myr after the Pop III SN explosion.

1.3.3 Chemical feedback

Once the first SNe explode and start to seed the gas with metals and dust grains, the physical properties of star forming regions change, eventually allowing the formation of the first low-mass Pop II stars if the cooling if sufficiently high. Fig. 1.5 (Maio & Viel, 2015) shows the temperature evolution of the $\Lambda(n, T)$ function for different metallicities, represented by different colors. It is clear that the presence of metals enhances the gas cooling, since they provide additional cooling channels through collisional ionization processes at high T and fine structure lines (mostly O I, C II, Fe II and Si II) at low T. Hence the presence of metals (in gas-phase and/or locked into dust grains) is a crucial ingredient for the formation of stars, modifying the typical mass scales of fragments and inducing a transition between massive Pop III stars to normal Pop II stars, the so-called chemical feedback. Indeed, gas at low metallicity can achieve larger cooling rates through additional molecular species (HD, OH, CO, H_2O), fine structure line–cooling (mostly O I and C II) (Bromm et al., 2001; Bromm & Loeb, 2003; Santoro & Shull, 2006), and thermal emission from dust grains (Omukai, 2000; Schneider et al., 2002; Omukai et al., 2005; Schneider et al., 2006, 2012a). The relative importance of these coolants depends on the density (time) regime during the collapse and on the initial metallicity and dust content of the collapsing core. In Fig. 1.6 we show the prestellar temperature evolution calculated by a one-zone model with different metallicities, including the presence of dust (Omukai et al., 2005). Similar results are obtained by using a radiation hydrodynamical calculation assuming spherical symmetry to describe high density regimes (Omukai et al., 2010). In particular, Fig. 1.6 shows the cases from solar metallicity ($Z = Z_{\odot}$, i.e. [M/H][4]=0) to $Z = 10^{-6} Z_{\odot}$ (i.e. [M/H]=-6) every 1 dex in metallicity. In addition, also the primordial case is shown, $Z = 0$, similarly to what described in Fig. 1.2. Once again, we stress that the gas can cool if the temperature-density relation reaches a minimum, and the Jeans mass related to this condition represents the characteristic fragmentation scale. As the gas metallicity increases, the temperature-density track shows two minima: the first (low n) being related to line-emission cooling, i.e. H_2 and HD cooling and to C and O fine-structure line cooling, the second (higher n) to dust cooling. In particular, at low metallicities the typical Jeans mass at the dust-cooling minimum is of order [0.1-1] $M_{\odot}$.

From a more quantitative point of view, gas cooling due to line emission affects the thermal evolution of collapsing cores at low-to-intermediate densities: when the total metallicity of the gas is $Z < 10^{-2} Z_{\odot}$, molecular cooling dominates at $n < 10^5 \mathrm{cm}^{-3}$, with an efficiency which increases with metallicity because of the larger molecular formation rate on the surface of dust grains (Omukai et al., 2005; Schneider et al., 2006, 2012a). For more metal enriched clouds (i.e. $Z \geq 10^{-2} Z_{\odot}$) O I and C II fine-structure line cooling dominates the thermal evolution at $n < 10^4 \mathrm{cm}^{-3}$, until the NLTE-LTE transition occurs and the cooling efficiency decreases. Bromm & Loeb (2003) have derived the critical O and C abundances required to overcome the compressional heating rate and fragment the gas, finding $[\mathrm{C/H}]_{\mathrm{cr}} = -3.5$ and

[4]A quantity [X/H] is defined as $\log_{10}(n_X/n_H) - \log_{10}(n_X/n_H)_{\odot}$, where n_X is the number density of element X, and n_H that of hydrogen.

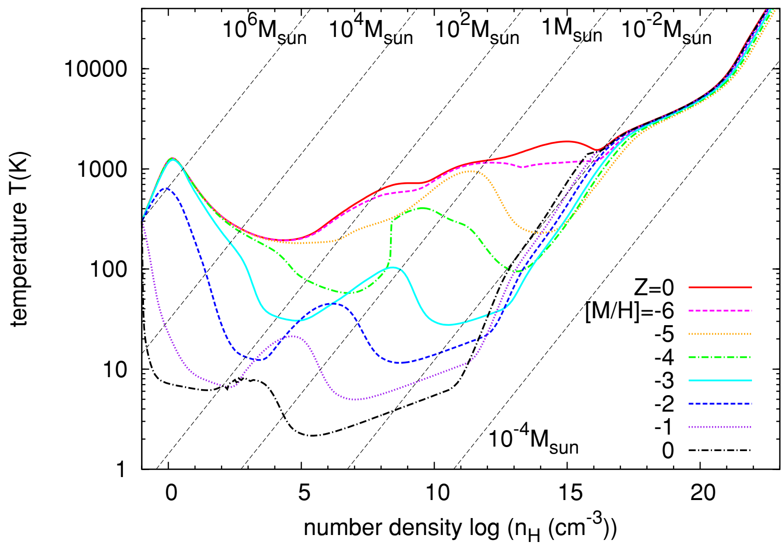

Figure 1.6 *Evolution of temperatures in prestellar cloud cores with metallicities* $Z/Z_\odot = 0, 10^{-6}, 10^{-5}, 10^{-4}, 10^{-3}, 10^{-2}, 10^{-1}$ *and 1 as functions of the number density, which is calculated by one-zone models (Omukai et al., 2010). The dashed diagonal lines indicate the constant Jeans masses. For those above* $10^2 M_\odot$ *(below* $1 M_\odot$*), the gas is assumed to be fully atomic (molecular).*

$[\mathrm{O/H}]_{\mathrm{cr}} = -3.05$. Frebel et al. (2007) have further explored the role of metal fine-structure line cooling by introducing the so-called transition discriminant (a combination of the C and O abundances) that enables the formation of Pop II stars when its value exceeds a critical threshold of $\mathrm{D}_{\mathrm{tr,cr}} = -3.5 \pm 0.2$. In a recent numerical simulation, Safranek-Shrader et al. (2014) have confirmed that there is a clear metallicity threshold for widespread fragmentation between $[10^{-4} - 10^{-3}]Z_\odot$ in high-redshift, atomic-cooling halos ($T_{vir} > 10^4$ K): fine-structure line cooling allows the gas to cool to the CMB temperatures and form a cluster of size ~ 1 pc, with typical fragment masses $\sim 50 - 100\,M_\odot$, consistent with the Jeans masses expected at the end of the fragmentation phase. Although the simulations do not follow the evolution of the cluster to higher densities, taking these results at face value it appears that fine-structure line cooling is not capable of producing solar-mass fragments that have the potential to survive until the present-day, corroborating previous findings based on semi-analytical models (Schneider et al., 2006).

A pervasive fragmentation mode that allows the formation of solar/subsolar mass fragments is activated at higher gas densities, $n > [10^{10} - 10^{12}]\mathrm{cm}^{-3}$, when dust grains are collisionally excited and emit continuum radiation, thereby decreasing the gas temperature until it becomes thermally coupled with the dust temperature $T = T_{\mathrm{dust}}$ or the gas becomes optically thick (Schneider et al., 2002). The efficiency of this physical process depends on the dust-to-gas ratio and on the total grain cross-section, with smaller grains providing a larger contribution to cooling (Schneider et al., 2006). Hence, the minimal conditions for dust-induced fragmentation have been expressed in terms of a minimal critical dust-to-gas ratio,

$$S\,\mathcal{D}_{\mathrm{cr}} = 1.4 \times 10^{-3}\ \mathrm{cm^2 g^{-1}} \left(\frac{T}{10^3\ \mathrm{K}}\right)^{-1/2} \left(\frac{n}{10^{12}\mathrm{cm}^{-3}}\right)^{-1/2}, \tag{1.18}$$

where S is the total cross-section of dust grains per unit dust mass and the expression holds in the regime where dust cooling is effective, hence $T_{\rm dust} \ll T$. An extensive parameter-space exploration shows that $\mathcal{D}_{\rm cr} \sim 4.4 \times 10^{-9}$ can be considered as a good representative value for the minimal dust enrichment required to activate dust-induced fragmentation (Schneider et al., 2012a). These results have been confirmed by numerical simulations (Tsuribe & Omukai, 2006, 2008; Clark et al., 2008; Omukai et al., 2010; Dopcke et al., 2011).

Chemical feedback is a local process: regions close to star formation sites rapidly become metal-polluted with metallicities $Z > Z_{cr}$, while others remaining almost metal-free. Hence it is very likely that the transition occurred rather smoothly because the cosmic metal distribution is observed to be highly inhomogeneous: even at moderate redshifts, $z \approx 3$, observations are consistent with a metal filling factor $\sim 10\%$, showing that metal enrichment is incomplete and inhomogeneous (e.g. Schaye et al., 2003; D'Odorico et al., 2016).
Scannapieco et al. (2003) used an analytical model of inhomogeneous structure formation to study the separate evolution of Pop III/II stars as a function of star formation and SN wind efficiencies. Their main finding was that, essentially independent of the free parameters of the model, Pop III stars continue to contribute to the star formation rate density at much lower redshift, even if several order of magnitudes lower than Pop II. Indeed, due to inefficient heavy element transport by outflows large fluctuations around the average metallicity arise, resulting in a Pop III star formation which can continue even down to $z = 2.5$. Similar results are found by hydrodynamical simulations (e.g. Tornatore et al., 2007; Wyithe & Cen, 2007; Ricotti et al., 2008; Maio et al., 2010, 2011; Muratov et al., 2013; Pallottini et al., 2014; Starkenburg et al., 2016).

Due to these feedback processes, Pop III stars have always been sub-dominant with respect to Pop II stars and being likely massive, they lasted only few Myrs. Hence the observation of Pop III stars is a very challenging task.The properties of the first stars may be probed by their nucleosynthetic signature, which is likely imprinted in second-generation stars that form from metal-enriched gas. If they survive to the present day, their surface abundances may reflect the metal enrichment pattern of the cloud out of which they formed. This approach of probing the first stars has been termed "stellar archeology", or "near-field cosmology" (Beers & Christlieb, 2005; Sneden et al., 2008; Frebel, 2010; Karlsson et al., 2013).

1.4 Observations of Galactic halo stars

Being highly metal poor and old, the stars of the Galactic halo are assumed to have formed in an almost primordial gas which has only been enriched by the first generation of stars. Hence, the observed abundance pattern in any of these low-mass long-living Pop II stars should depend on the chemical yields of Pop III stars. Since Pop III stars with different masses produce different amount (and species) of chemical elements and dust, in principle, it would be possible to set constraints on their properties by interpreting the properties of these ancient and metal-poor stars.

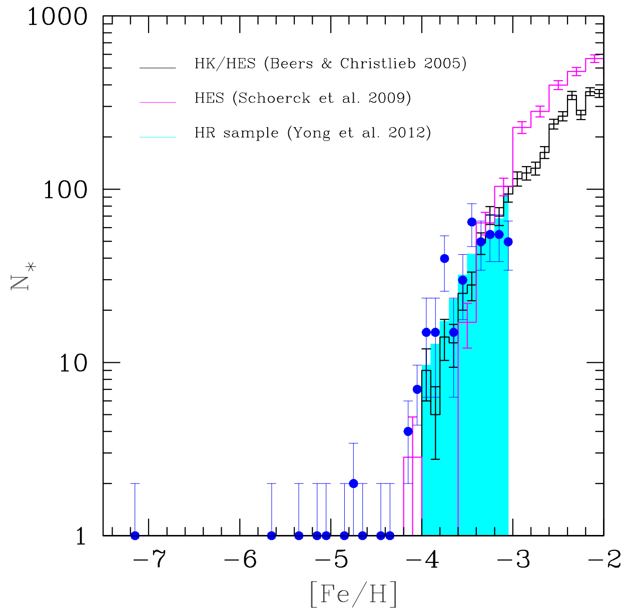

Figure 1.7 *The Galactic halo MDFs obtained using different data-sets and normalized to the same number of stars at [Fe/H]≤ −3. Histograms show the result from: black - the medium resolution HK and HES surveys (Beers & Christlieb, 2005); magenta - the HES survey corrected for observational biases and incompleteness (Schörck et al., 2009); cyan shaded - the homogeneous sample of high-resolution (HR) spectroscopic data from Yong et al. (2013b), corrected to account for incompleteness and observational errors. The blue points show the uncorrected sample by Yong et al. (2013b) to which we added HR data for stars with [Fe/H] < −4, taken from recent literature (see text for details and references). Errorbars represent poissonian errors.*

1.4.1 The metallicity distribution function

Low- and medium- resolution large survey projects, such as the HK survey (Beers et al., 1992), the Hamburg-ESO survey (HES, Wisotzki et al., 2000; Christlieb, 2003), the Sloan Digital Sky Survey (SDSS, York et al., 2000; Gunn et al., 2006) and the Sloan Extension for Galactic Understanding and Evolution (SEGUE, Yanny et al., 2009), are capable to detect a large number of metal-poor stars, i.e. with [Fe/H]$\lesssim$-2: ∼ 1200 (HK), ∼ 1500 (HES), >15000 (SDSS and SEGUE). However, these surveys can only provide the Fe abundance of stars, either by directly measuring the Fe I line or the Ca II line, which is the strongest metal absorption line in the optical wavelength range and which allows to derive the value of [Fe/H] (e.g. Beers et al., 1999). From these observations we can build the so-called metallicity distribution function (MDF), i.e. the number of stars, N_*, as a function of their [Fe/H].

Earlier determinations of the MDF by Ryan & Norris (1991) have shown that the MDF peaks around [Fe/H] = −1.6, with wings from solar abundances down to [Fe/H]≈ −3, although one star at [Fe/H]≈ −4 was already discovered thanks to serendipitous detection (Bessell & Norris, 1984). Spectroscopic follow-up of the HK survey (Beers et al., 1985) by Molaro & Castelli (1990), Molaro & Bonifacio (1990) and Primas et al. (1994) showed that the tail extended down

to [Fe/H] ≈ −4.0.
More recent observations by the HES and the HK survey (e.g. Christlieb et al., 2008) have confirmed the presence of the MDF peak at [Fe/H] ≈ −1.6 and have lead to the identification of some hundreds of new stars at [Fe/H] < −3 (see Fig. 1.7). These "extremely metal-poor stars" are of key importance to understand the early chemical enrichment processes. In particular, it has been shown that the shape of the low-Fe tail of the Galactic halo MDF can shed new light on the properties of the first stellar generations, and on the physical processes driving the transition from massive Pop III stars to normal Pop II stars (Tumlinson, 2006; Salvadori et al., 2007; Komiya et al., 2007; Salvadori et al., 2010a; Tumlinson, 2010; Hartwig et al., 2015; Komiya et al., 2016).
In Fig. 1.7, it is shown the most recent determination of the low-Fe tail of the Galactic halo MDF as derived by various groups, which exploited different data-sets. By normalizing the MDFs to the same cumulative number of stars at [Fe/H] ≤ −3 results from different surveys are compared: (*i*) the joint HK and HES medium-resolution surveys (Beers & Christlieb, 2005); (*ii*) the HES survey (e.g. Christlieb et al., 2008); the derived MDF has been corrected by Schörck et al. (2009) to account for observational biases and incompleteness; (*iii*) the high-resolution sample by Yong et al. (2013b), who collected an homogeneous ensemble of ≈ 95 stars at [Fe/H] ≤ −2.97 by combining data from the literature along with program stars. Following Schörck et al. (2009), Yong and collaborators corrected the high-resolution MDF by using the HES completeness function. Furthermore, they accounted for the gaussian error associated to each [Fe/H] measurements, and derived a realistically smoothed MDF (see their Sec. 3.2 and Fig. 1.7). The effects of these corrections can be appreciated by comparing the final high-resolution (HR) MDF in Fig. 1.7 (shaded area), and the points with error bars within −4 ≤ [Fe/H] ≤ −3, which represent the raw data.
By inspecting Fig. 1.7 it can be seen that the MDFs obtained with the high-resolution sample by Yong et al. (2013b) and the joint HK and HES samples by Beers & Christlieb (2005) are in excellent agreement. Both MDFs continuously decrease between [Fe/H] ≈ −3 and [Fe/H] ≈ −4 spanning roughly one order of magnitude in N_*. On the other hand, the HES sample underestimates the total number of stars at [Fe/H] ≤ −3.7. As discussed by Yong et al. (2013b), this is likely due to the selection criteria exploited by the HES sample, which reject stars with strong G-bands. At lower [Fe/H], the sample is completed by adding all the stars that have been discovered during the years and followed-up at high-resolution (see points in Fig. 1.7). Thus, the observed MDF exhibits a sharp cut-off at [Fe/H] = −4.2 ± 0.2 and a low-Fe tail made by 9 stars that extends down to [Fe/H] ≈ −7.2 (Keller et al., 2014).
A very challenging aspect of the study of the most metal-poor stars is their extreme rarity. Below [Fe/H]$\lesssim$-4.5, only nine stars are known (Christlieb et al., 2002; Frebel et al., 2005; Norris et al., 2007; Caffau et al., 2011a; Keller et al., 2014; Hansen et al., 2015; Bonifacio et al., 2015; Allende Prieto et al., 2015; Frebel et al., 2015; Meléndez et al., 2016).
Once metal-poor stars ([Fe/H] < -2) are selected, higher resolution spectroscopic follow-up can allow to determine the abundance of other chemical species (e.g Cayrel et al., 2004; Barklem et al., 2005; Suda et al., 2008; Frebel, 2010; Aoki et al., 2013; Norris et al., 2013). One of the key element which can be observed is carbon, which can induce metal-line cooling (Bromm et al., 2001; Bromm & Loeb, 2003; Santoro & Shull, 2006) and that can be produced by faint SNe (see Sec. 1.2.2). Hence, observations of the MDF and of chemical abundances of stars might provide

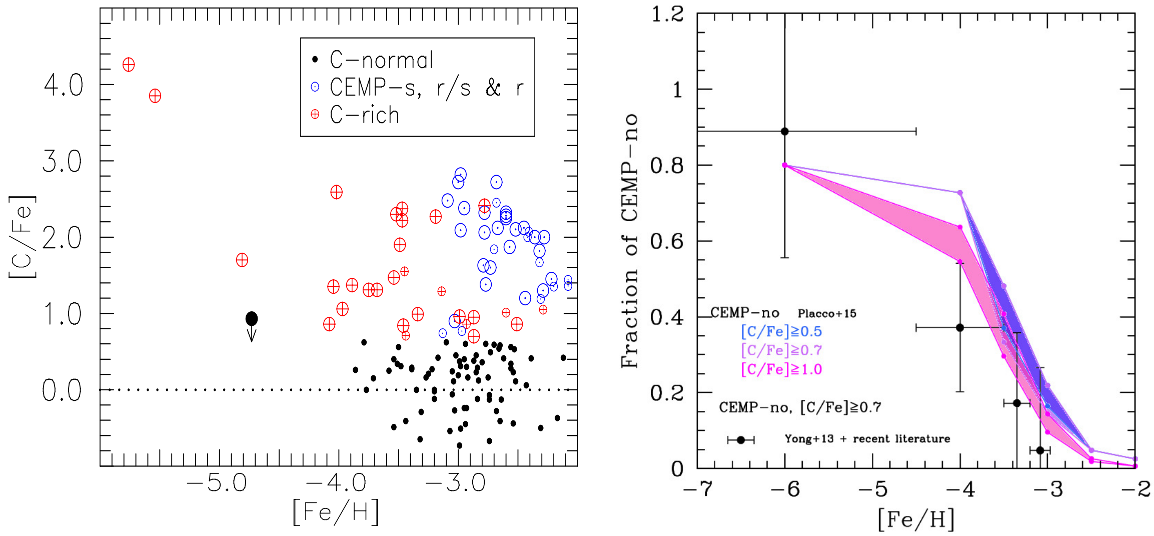

Figure 1.8 *Left panel) [C/Fe] vs. [Fe/H] for the C-rich stars (CEMP-no stars and two with [Fe/H]~-5.5) (large crossed circles) and CEMP-r, -r/s, -s stars (large dotted circles) from Norris et al. (2013). Smaller symbols are used for the data of Barklem et al. (2005). The large filled circle represents the ultra metal-poor, C-normal, star SDSS J102915+172927 (Caffau et al., 2011a), while the small filled circles are the data from Yong et al. (2013b). Note that in this panel most recent CEMP-no stars at [Fe/H]<-4.5 are missing (i.e. Keller et al., 2014; Hansen et al., 2015; Bonifacio et al., 2015; Allende Prieto et al., 2015; Frebel et al., 2015; Meléndez et al., 2016). The horizontal dotted line represents the solar [C/Fe]. (Right panel) Fraction of CEMP-no stars vs [Fe/H] obtained using different data and [C/Fe] cuts for CEMP-no stars (see the labels). Results are from: high-resolution sample by Yong et al. (2013b) that we completed by adding more recent literature data (points with poissonian errorbars); the larger high/medium-resolution sample by Placco et al. (2013) (connected colored points) that the authors corrected to account for carbon depletion due to internal mixing processes (upper points). The shaded area quantifies such a correction.*

fundamental constraints on galactic chemical enrichment models and on the nucleosynthetic yields of the first stars.

1.4.2 Carbon-enhanced metal-poor stars

High- and medium-resolution spectroscopic studies of Galactic halo stars have revealed the existence of a population of carbon-rich stars at [Fe/H]<-3, usually called carbon-enhanced metal-poor (CEMP) stars (e.g. Beers & Christlieb, 2005; Aoki et al., 2007; Lee et al., 2013; Norris et al., 2013; Yong et al., 2013b). These objects are usually defined to have carbon-to-iron ratio [C/Fe]>0.7 (Aoki et al., 2007), and they can be divided into two main populations: (*i*) carbon-rich stars that exhibit an excess in heavy elements formed by slow (or rapid) neutron capture processes, CEMP-s (CEMP-r) stars, and (*ii*) carbon-rich stars that do not exhibit such an excess, CEMP-no stars. The available data are consistent with the idea that CEMP-s/-rs stars belong to binary systems (Lucatello et al., 2005; Starkenburg et al., 2014), and have acquired their carbon-excess from an AGB companion (e.g. Bisterzo et al., 2012; Placco et al., 2013; Abate et al., 2015). Thus, the chemical abundances measured in these stars are not representative of the gas out of which they formed. On the other hand, CEMP-no stars are not preferentially associated with binary systems (Cohen et al., 2013; Hansen et al., 2013; Norris et al., 2013; Starkenburg et al., 2014). Hence there is no observational evidence supporting the idea of mass transfer as the origin of their chemical abundances, which was suggested by some authors (e.g. Suda et al., 2004; Komiya et al., 2007).

In Fig. 1.8 (left panel), we show the [C/Fe] vs [Fe/H] for the sample of Galactic halo stars presented in Norris et al. (2013). C-rich and CEMP-no stars are plotted as red crossed circles, and the CEMP-r, -r/s, and -s stars are presented as blue dotted circles. The small filled circles represent C-normal stars of Yong et al. (2013b) that have carbon detections, while the large filled circle shows the upper limit for the ultra metal-poor dwarf SDSS J102915+172927 (Caffau et al., 2011a). We note in particular that while CEMP-no stars are found at all metallicities below [Fe/H]<-2, there are no CEMP-r, -r/s, or -s stars with [Fe/H]<-3.1. The right panel of Fig. 1.8 shows the fraction of CEMP-no stars in different [Fe/H] bins, $F_{\mathtt{CEMP-no}} = N_{\mathtt{CEMP-no}}([\mathrm{Fe/H}])/N_*([\mathrm{Fe/H}])$, derived by using the HR sample by Yong et al. (2013b) along with new literature data. Only in the lowest bin, [Fe/H]< -4.5, the total number of stars is limited to $N_* = 9$. This is reflected in the larger Poissonian errors. Fig. 1.8 (right panel) also shows the $F_{\mathtt{CEMP-no}}$ values obtained by using the available data and CEMP-no classification by Placco et al. (2014). These authors exploited a larger sample of high- and medium-resolution observations. Furthermore, they corrected the carbon measurements in Red Giant Branch (RGB) stars in order to account for the depletion of the surface carbon-abundance, which is expected to occur during the RGB phase. In both samples $F_{\mathtt{CEMP-no}}$ rapidly decreases with increasing [Fe/H], and the results are consistent within the Poissonian errors. However, as already noticed by Frebel et al. (2016), the estimated CEMP-no fraction is higher in the sample by Placco et al. (2014).

By inspecting Fig. 1.8, we see that both the carbon-excess and the frequency of CEMP-no stars increase with decreasing [Fe/H] (e.g. Lucatello et al., 2005; Lee et al., 2013; Norris et al., 2013). Moreover, 8 out of the 9 halo stars discovered up to now at [Fe/H]<-4.5 appear to be CEMP stars (Christlieb et al., 2002; Frebel et al., 2005; Norris et al., 2007; Keller et al., 2014; Hansen et al., 2015; Bonifacio et al., 2015; Allende Prieto et al., 2015; Frebel et al., 2015; Meléndez et al., 2016). Although only 5 of these CEMP stars have available measurements of slow- and rapid-neutron capture process elements, which have subsolar values, all of them can be likely classified as CEMP-no stars (e.g. see discussion in Bonifacio et al. 2015 and Norris et al. 2010). These findings favor the idea that CEMP-no stars are a peculiar stellar population and that their chemical abundances likely reflect their birth environment. While it seems that most of the observed metal-poor stars show the chemical imprint of core-collapse SNe (Cayrel et al., 2004; Tumlinson, 2006; Heger & Woosley, 2010; Joggerst et al., 2010), the unusual chemical compositions of the most iron-poor and carbon-rich stars can be successfully matched by models of primordial faint SNe that experienced mixing and fallback, hence releasing small amounts of iron and large amounts of carbon and other light elements (e.g. Bonifacio et al., 2003; Umeda & Nomoto, 2003; Iwamoto et al., 2005; Joggerst et al., 2009; Marassi et al., 2014; Tominaga et al., 2014). Relatively good agreement with observations is also obtained by models of zero- (or very low-) metallicity massive “spinstars”, which experience mixing and mass-loss because of their very high rotational velocities (e.g. Meynet et al., 2006, 2010; Maeder et al., 2015). More massive Pop III stars (i.e. PISNe) produce a large amount of metals ($\sim 50\%$ of their mass), and typically enrich the nearby gas to relatively high metallicity, of order $Z \gtrsim 10^{-3} Z_{\odot}$, so that any second-generation stars forming out of this material would be a metal enriched Pop II star (Greif et al., 2010; Wise et al., 2012). Moreover, the chemical signature of a PISN is quite different from core-collapse or faint SNe (Heger & Woosley, 2002). Notably, current observations show that there is almost no sign for PISN enrichment. The absence of any PISN signal was interpreted as evidence that the first stars were typically massive, to enable core-collapse events, but probably not very massive ($m_* \gtrsim 140 M_{\odot}$) or due to an observational selection effect (Salvadori et al., 2007; Karlsson et al., 2008). Indeed, up to now only Aoki et al. (2014) possibly detected the chemical imprint of PISNe in 1 out of 500 stars at [Fe/H] < -2.

2

Decoding the stellar fossils of the dusty Milky Way progenitors

As already discussed in Sec. 1.2, the physical conditions which enable the formation of the first low-mass and long-lived stars to form in the Universe are still a subject of debate. The best available indications from numerical studies (Sec. 1.2.1) suggest that the first stars formed with plausible mass ranges that can vary from sub-solar values (e.g. Stacy et al., 2016) up to $m_{\rm PopIII} \approx 1000 M_{\odot}$ (e.g. Susa et al., 2014; Hirano et al., 2014, 2015; Hosokawa et al., 2016).

Once the first SNe explode and start to seed the gas with metals and dust grains, the physical properties of star forming regions change (Sec. 1.3), eventually allowing the formation of the first low-mass Pop II stars. Gas at low metallicity can achieve larger cooling rates through additional molecular species (HD, OH, CO, H_2O), fine-structure line cooling (mostly OI and CII), and thermal emission from dust grains (Omukai, 2000; Schneider et al., 2002; Omukai et al., 2005).

In this Chapter, we describe an improved version of the hierarchical semi-analytical code GAlaxy MErger Tree and Evolution (GAMETE) originally developed by Salvadori et al. (2007). The main goal is to investigate whether current observations of the MDF and of the relative contribution of CEMP stars at different [Fe/H] can provide constraints on the IMF of Pop III stars and on the physics governing the Pop III/II transition. To this aim, following Valiante et al. (2011), the chemical model has been improved by including the dust evolution in a 2-phase ISM. in this model, grains are destroyed by SN shocks in the diffuse, hot phase, but are shielded from destruction in the dense, cold phase, where they can grow in mass by accreting gas-phase metals. This model can predict the stellar, gas, metal and dust content of all the MW progenitors along the simulated merger trees from $z = 20$ down to $z = 0$. The model free parameters are constrained by comparing the theoretical predictions with observations of the global properties of the MW, such as the gas mass, the stellar content, the metallicity, and the dust-to-gas ratio. In addition, the properties of the MW progenitors predicted by the model appear to be in good agreement with the observed scaling relations between the dust/metal and gas/stellar components inferred from samples of galaxies at $0 < z < 6$.

This Chapter is organized as follows: in Section 2.1 we present the main properties of the algorithm aimed to build the MW merger tree; in Section 2.2 we give a short description of the basic properties of the GAMETE code, with particular attention to the new features implemented in this work. In Section 2.3 we explain how we calibrate the model free parameters to reproduce the observed global properties of the MW. In Section 2.4 we compare the predicted properties of MW progenitors with observational data collected from various galaxy samples. In Section 2.5 we apply the model to Galactic Archaeology, exploring the dependence of the simulated MDF to the assumed Pop III IMF (2.5.1) and Pop III/II transition criteria (2.5.2); we make specific predictions for the metallicity distribution of CEMP stars (2.5.3), comparing the model with observations. Finally, in Section 2.7 we discuss our results and present our main conclusions.

2.1 The semi-analytical merger tree

Conversely to N-body simulations, semi-analytical models reconstruct the hierarchical merger tree by using the Press & Schechter formalism (Sec. 1.1.2), which combines the linear perturbation theory with the spherical top-hat model for the non-linear collapse. The DM halo mass distribution drawn from this approximated approach shows an excellent agreement, as shown by Parkinson et al. (2008), with that derived from N-body simulations (e.g. the Millennium simulation, Springel et al., 2005) and the same is true for the specific case of the MW Galaxy (e.g. Salvadori, 2009, Fig. 2.3), but its main drawback consists in the lack of spatial informations. However, since semi-analytical models can rapidly run on merger trees, this approach enables to efficiently explore the effects of different model parameters on a large sample of possible assembly histories of our Galaxy, which is unknown. Hence, it is the perfect statistical tool to study the impact of the high-z star formation on the observed properties of present-day stars while accounting for the uncertainties induced by different assembling histories.

The algorithms reconstructing hierarchical merger trees generically use semi-analytical approaches based on the so-called Extended Press & Schechter (EPS) theory (Bond et al., 1991; Lacey & Cole, 1993) which describes the DM halo formation in terms of trajectories of the linear density field. Such a different approach provides the description of the halo merging through the following formula:

$$f(M, M_0)dM = \frac{1}{2\pi}\frac{\delta_c - \delta_{c,0}}{\sigma^2_M - \sigma^2_{M,0}} exp\Big[- \frac{(\delta_c - \delta_{c,0})^2}{2(\sigma^2_M - \sigma^2_{M,0})}\Big]\Big|\frac{d\sigma^2_M}{dM}\Big| dM. \tag{2.1}$$

This equation gives the mass fraction within a halo of mass M_0 at redshift z_0 which, at an earlier time $z > z_0$, belongs to less massive progenitors having mass between M and $M + dM$ (see also Cole et al. 2000). The quantities $\delta_c = \delta_c(z)$ and σ^2_M are the critical linear overdensity threshold for collapse at redshift z and the linear r.m.s. density fluctuation smoothed with a top-hat filter of mass M, respectively. The quantities with a 0 subscript are referred to redshift z_0 ($\delta_{c,0} = \delta_c(z_0)$) and to mass M_0 ($\sigma^2_{M,0}$). Multiplying $f(M, M_0)$ by M_0/M, the number of haloes per unit mass can be obtained:

$$\frac{dN(M, M_0)}{dM}dM = \frac{M_0}{M}f(M, M_0)dM \tag{2.2}$$

Eq. 2.2 is the basic equation to reconstruct the hierarchical merger history of a given DM halo. Following Cole et al. (2000) and Volonteri et al. (2003), the code has been developed with a binary Monte Carlo algorithm accounting for mass accretion. By taking the limit $z \to z_0$, Eq. 2.2 provides the average number of progenitors in the mass range $M, M + dM$, into which a halo of mass M_0 fragments considering a step dz back in time (Cole et al., 2000):

$$\frac{dN}{dM}dM = \frac{1}{2\pi}\Big(\frac{1}{\sigma^2_M - \sigma^2_{M,0}}\Big)^{3/2}\frac{M_0}{M}\frac{d\delta_c}{dz}\Big|\frac{d\sigma^2_M}{dM}\Big|dMdz \tag{2.3}$$

where $M < M_0$ and $z = z_0 + dz$. Hierarchical trees are reconstructed by recursively using this equation to decompose any given DM halo (at any initial redshift) into its progenitors assuming cosmological parameters taken from the recent results of the Planck Collaboration et al. (2014) and listed in Sec. 1.1. Given the shape of the matter power spectrum in ΛCDM models, the number of haloes in the Eq. 2.3 diverges as the mass M goes to zero. For this reason a resolution mass M_{res} has been introduced to avoid this problem. This quantity marks the transition between progenitors and mass accretion. At any given time-step, in fact, haloes can either (*i*) lose part of their mass, corresponding to the cumulative fragmentation into haloes with $M < M_{res}$, or (*ii*) fragment into two progenitor halos and lose mass. At each redshift, the mass below the resolution limit accounts for the MW environment (or IGM), which represents the ambient into which haloes are embedded. Note that we are referring to mass accretion as the process of mass loss in the backward stepping merger algorithm since physically, i.e. going into the correct temporal way, this is what it really represents. Once M_{res} is fixed, one can compute the mean number of progenitors between $M_{res} < M < M_0/2$ that a halo of mass M_0 at z_0 is fragmented into during a time-step dz:

$$N_p = \int_{M_{res}}^{M_0/2} \frac{dN}{dM}dM, \tag{2.4}$$

as well as the accreted mass function:

$$F_a = \int_0^{M_{res}} \frac{dN}{dM}\frac{M}{M_0}dM. \tag{2.5}$$

Both these quantities depend on dz (see Eq. 2.3) that has to be suitably chosen in order to prevent multiple fragmentations ($N_p < 1$) hence ensuring the binarity of the code. Since the number of progenitors decreases with dz, binary algorithms generally require a high temporal (redshift) resolution. More practically the Monte Carlo code works as follow: at each time step and for each progenitor mass M_0, a random number $0 < R < 1$ is generated and compared with the value N_p derived by Eq. 2.4. If $N_p < R$, the halo does not fragment at this step. However, a new halo with mass $M_0 \times (1 - F_a)$ is produced, to account for the accreted matter. On the contrary, if $N_p \geqslant R$ fragmentation occurs: a new random value in the range $M_{res} < M < M_0/2$ is drawn from the distribution in Eq. 2.3 to produce a progenitor of mass M; mass conservation sets the mass of the second progenitor to $M_0 \times (1 - F_a) - M$. This procedure is applied to each progenitor halo and at each redshift, providing the whole hierarchical tree of the MW, from the present-day up to $z = 20$ (this algorithm is universal, i.e. it can be used to reconstruct the hierarchical tree of any given DM halo, from an initial redshift up to a final one). Note that at every time and for each progenitor halo, the IGM mass increases with a contribution $M_0 \times F_a$, hence becoming more massive at higher z.

We now need to specify the free parameters of the model, M_{res} and dz. A high value of M_{res} would be required to preserve the binarity of the code (Eq. 2.4) and to control the computational cost implied by a very high time resolution. However, we need M_{res} to be small enough to resolve the low mass haloes that are presumably hosting the first stars. In addition, M_{res} must be redshift dependent, decreasing with increasing redshift, to better reproduce the EPS predictions at high z (Volonteri et al., 2003). The halo mass, corresponding to a virial equilibrium temperature T_{vir} at redshift z, can be derived from Eq. 1.12:

$$M(T_{vir}, z) \approx 10^8 M_\odot \Big(\frac{10}{1+z}\Big)^{3/2} \Big(\frac{T_{vir}}{10^4\mathrm{K}}.\Big)^{3/2} \tag{2.6}$$

where $\left[\frac{\Omega_m}{\Omega_m(z)} \frac{\Delta_c}{18\pi^2}\right] \approx 1$ in the analyzed redshift range. Given the above redshift dependence, taking $M_{res} \propto M(T_{vir}, z)$ appears physically motivated. In addition, in this Chapter the analysis will predominantly focus on haloes with mass $M \geqslant M(T_{vir} = 2 \times 10^4\mathrm{K}, z)$, assuming that star formation in mini-halos is suppressed by strong radiative feedback effects (Sec. 1.3). Hence, star formation occurs in halos above a minimum mass, $\mathrm{M_{sf}}$, that corresponds to the minimum mass of Ly-α cooling halos (in Chapter 3 the star formation process in mini-halos will be discussed), hence to halos with virial temperature $T_{vir} = 2 \times 10^4$ K, $M_{sf}(z) = M_{vir}(2 \times 10^4\mathrm{K}, z)$ (Eq. 1.12). Thus, we have chosen a resolution mass $M_{res}(z) = M_{sf}(z)/10$ which enables to accurately follow the history of all MW progenitors having $M \geqslant M_{sf}(z)$ up to $z = 20$. The time-step dz is empirically selected in order to obtain a good agreement between the EPS predictions and numerical results. We started by considering 820 time-steps logarithmically spaced in expansion factor between $z = 0$ and $z = 20$. However, since the number of haloes in the high mass range was found to exceed the EPS predictions, we have reduced the time-step by a factor 5 within the redshift interval $8 < z < 12$, getting a final number of steps of 1435. Finally, we assume a MW dark matter halo mass of $M_{MW} = 10^{12} M_\odot$ in agreement with current measurements and uncertainties: $1.26^{+0.24}_{-0.24} \times 10^{12}\, M_\odot$ (McMillan, 2011), $0.9^{+0.4}_{-0.3} \times 10^{12}\, M_\odot$ (Kafle et al., 2012), $0.80^{+0.31}_{-0.16} \times 10^{12}\, M_\odot$ (Kafle et al. 2014, see also Wang et al. 2015 for the different methods adopted to infer the DM mass). Fig. 2.1 shows the comparison between the theoretical EPS DM halo

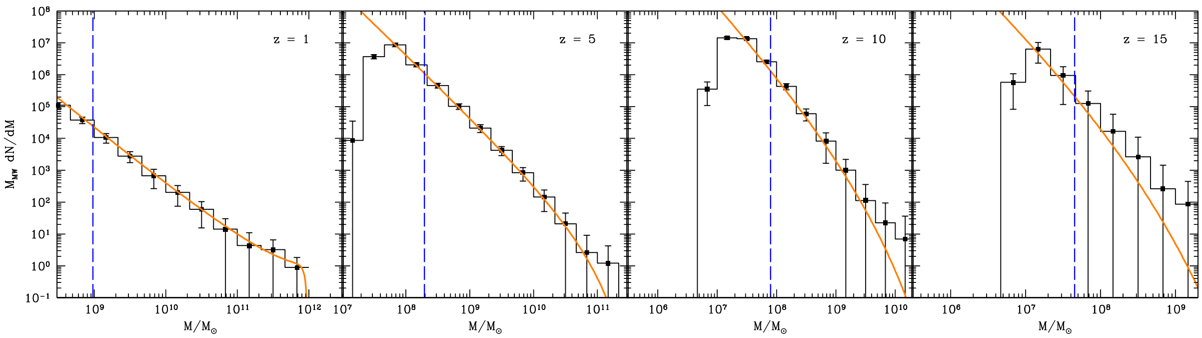

Figure 2.1 *Number of halos as function of halo mass at different redshifts (z=1, 5, 10, 15 from left to right) for a MW-like final DM halo of $10^{12} M_\odot$. The orange solid lines are the analytic predictions from the EPS theory, while the histograms are the simulated mass functions averaged over 50 merger trees. Error bars are given by Poissonian errors. Vertical lines correspond to the adopted minimum mass of star forming halos, M_{sf}, at the corresponding redshift.*

mass function and the simulated one averaged over 50 merger trees[1]. Different panels correspond to different redshifts and in each panel the vertical line represents the $M_{sf}(z)$ computed at the corresponding redshift. The comparison shows that there is a good agreement with the EPS (within the error bars), particularly for $M \gtrsim M_{sf}(z)$, which is the mass range we are interested in. An increase in the minimum mass of star forming halos is expected during cosmic reionization, due to the increased Jeans mass in ionized regions, which causes the quenching of the gas infall in halos below a given circular velocity $v_c(z)$ or DM halo mass (Gnedin, 2000; Hoeft et al., 2006; Okamoto et al., 2008). While the details of the evolution of $v_c(z)$ depend on the reionization redshift, amplitude of the ionizing background and redshift (Noh & McQuinn, 2014), here we simply assume that star formation is quenched in DM halos with circular velocities smaller than $v_c = 30\,\mathrm{km\,s^{-1}}$ when $z < z_{reion} = 6$ (Salvadori & Ferrara, 2009).

2.2 Description of the model

The GAMETE code allows to reproduce the observed global properties of the MW, such as the mass of gas and stars, metallicity and dust-to-gas ratio, predicting their evolution along cosmic time. Enrichment processes are assumed to be regulated by stars, both AGB stars and SNe, which eject metals and dust into the ISM according to their stellar lifetime (i.e. stars with different masses and metallicities evolve on different timescales); at each time, the star formation rate (SFR) is taken to be proportional to the available mass of gas in the ISM,

[1] We use 50 possible MW merger histories because we find that the results converge with this number of realizations, thus a larger number would not provide any improvement in our findings.

$\mathrm{SFR}(t) = \epsilon_* \, M_{\rm ISM}(t)/t_{dyn}(t)$, where $t_{dyn}(t)$ is the dynamical timescale of the host DM halo, and ϵ_* is the star formation efficiency, a free parameter of the model.

2.2.1 Two-phase model for the ISM

GAMETE has further been implemented to describe the evolution of the gas in two separate phases of the ISM: a *diffuse* component (warm/hot low-density gas), where dust can be destroyed by SN shocks, and a *dense* or *molecular cloud* (MC) component (cold and dense gas), where star formation occurs and where dust grains can grow in mass by accreting gas-phase metals being shielded from destructive processes. While grain reprocessing in the ISM is still subject to many uncertainties, observations indicate that dust destruction takes place in regions of the ISM shocked to velocities of the order of 50 - 200 km s^{-1} (Welty et al., 2002; Podio et al., 2006; Slavin, 2009). In our model, part of the newly formed dust in SNe is destroyed in situ (hence in the cold dense medium) by the SN reverse shock (Bianchi & Schneider, 2007). Note also that in the dense phase of the ISM, the grains can grow to larger sizes and hence are generally more resistant to sputtering.

For each quantity (gas, metals, dust), the total mass is simply given by the sum of the masses in the two components. The gas present in the MW environment or IGM, where halos are embedded, is assumed to be only in the diffuse phase; when a DM halo first virializes, the ISM is initially accreted in the diffuse phase, with a gas infall rate $\dot{M}_{inf}$ (Salvadori et al., 2008). For star forming systems, with $M_{halo} \geq M_{sf}$, the following processes are considered:

1. the diffuse gas, $M^{\rm diff}_{\rm ISM}$, condenses into the dense molecular phase, $M^{\rm MC}_{\rm ISM}$, at a rate $\dot{M}_{\rm cond}$;
2. stars (M_*) form out of dense gas with a star formation rate SFR;
3. stars evolve and return gas, metals and dust in the diffuse phase;
4. dust in molecular clouds accretes gas-phase metals, while dust in the diffuse phase is partly destroyed by interstellar shocks due to SN explosions;
5. mechanical feedback due to SN explosions drives gas outflows, ejecting the diffuse gas into the IGM;
6. part of the dense phase returns to the diffuse phase due to dispersion of molecular clouds.

As a result, the time evolution of the gas is described by the following set of differential equations:

$$\dot{M}^{\rm diff}_{\rm ISM}(t) = \dot{M}_{inf}(t) - \dot{M}_{\rm cond}(t) + \dot{R}(t) - \dot{M}^{\rm diff}_{ej}(t), \tag{2.7}$$

and

$$\dot{M}^{\rm MC}_{\rm ISM}(t) = \dot{M}_{\rm cond}(t) - \mathrm{SFR}(t) - \dot{M}^{\rm MC}_{ej}(t). \tag{2.8}$$

In the above expressions, $\dot{R}(t)$ is the gas returned by stars to the ISM (Salvadori et al., 2008), and $\dot{M}_{ej}^{\rm diff}(t)$ and $\dot{M}_{ej}^{\rm MC}(t)$ represent the diffuse and dense gas ejection rate. The total mass of gas ejected per unit time $\dot{M}_{ej}$ due to SN-driven mechanical feedback is proportional to the SN explosion rate and the wind energy is regulated by a free parameter ϵ_w, controlling the conversion efficiency of SN explosion energy into kinetic energy (see Eq. 9 of Salvadori et al. 2008). Since the effect of SN-driven on different ISM phases is still poorly understood (Efstathiou, 2000; Powell et al., 2011), we studied different mass-loading prescriptions, finding that the higher is the MC ejection rate, the higher must be the condensation rate to reproduce the global properties of the MW. Hence we decide to follow Fu et al. (2013) and consider that the energy injected into the medium from SNe leads to the ejection only of the hot diffuse phase through mechanical feedback (i.e. $\dot{M}_{ej}^{\rm MC}(t) = 0$).

The physical processes leading to the formation of molecular clouds are still not fully understood (Dobbs et al., 2014). Here we adopt a simple empirical description, tailored to reproduce the observed mass of gas in the molecular and atomic components of the MW.

We assume the condensation rate to be proportional to the star formation rate, hence $\dot{M}_{\rm cond}(t) = \alpha_{\rm MC}\,{\rm SFR}(t)$, where $\alpha_{\rm MC}$ is a free parameter of the model. The above condensation rate is the net result of the mass exchange between the two ISM phases, which is regulated by the condensation of the diffuse gas into molecular clouds,

$$M_{\rm ISM}^{\rm diff}(t)/t_{form} = \frac{1}{1-f}\,\alpha_{\rm MC}\,{\rm SFR}(t), \tag{2.9}$$

and the dispersal of molecular gas into the diffuse phase,

$$M_{\rm ISM}^{\rm MC}(t)/t_{des} = \frac{f}{1-f}\,\alpha_{\rm MC}\,{\rm SFR}(t), \tag{2.10}$$

where $0 < f < 1$. Hence, the two-phase structure of the ISM is regulated by the free parameters f and $\alpha_{\rm MC}$. When $f \to 0$, the condensation process is very efficient and the gas content in the ISM is dominated by the MC phase. Conversely, when $f \to 1$ the condensation and dispersal rates are in equilibrium. As a result, the newly condensed phase is rapidly dispersed in the ISM, preventing the formation of a stable dense phase. As it will be shown in Sec. 2.3, the values of the two parameters, $\alpha_{\rm MC}$ and f, have been selected to reproduce the observed molecular and atomic gas masses in the MW.

This two-phase model has been also applied to high redshift quasars (Valiante et al., 2014), where accretion onto the central black hole and Active Galactic Nuclei (AGN) feedback are also included.

2.2.2 Chemical evolution

The enrichment in heavy elements (including both gas-phase metals and metals locked in dust grains) is described in the two-phase ISM by means of the following equations:

$$\begin{aligned}\dot{M}_Z^{\rm diff}(t) &= Z_{vir}(t)\,\dot{M}_{inf}(t) - Z_{\rm diff}(t)\,M_{\rm ISM}^{\rm diff}(t)/t_{form} \\ &+ Z_{\rm MC}(t)\,M_{\rm ISM}^{\rm MC}(t)/t_{des} + \dot{Y}_Z(t) - Z_{\rm diff}(t)\,\dot{M}_{ej}^{\rm diff}(t),\end{aligned} \tag{2.11}$$

and

$$\begin{aligned}\dot{M}_Z^{\rm MC}(t) &= Z_{\rm diff}(t)\,M_{\rm ISM}^{\rm diff}(t)/t_{form} - Z_{\rm MC}(t)\,M_{\rm ISM}^{\rm MC}(t)/t_{des} \\ &- Z_{\rm MC}(t)\,{\rm SFR}(t) - Z_{\rm MC}(t)\,\dot{M}_{ej}^{\rm MC}(t),\end{aligned} \tag{2.12}$$

where $Z_{\rm diff} = M_Z^{\rm diff}(t)/M_{\rm ISM}^{\rm diff}(t)$ and $Z_{\rm MC} = M_Z^{\rm MC}(t)/M_{\rm ISM}^{\rm MC}(t)$ are the total (gas-phase + dust) metallicities of the diffuse and dense phases, Z_{vir} is the metallicity of the gas accreted from the IGM and $\dot{Y}_Z(t)$ is the rate at which heavy elements produced by stars are returned to the ISM, given by,

$$\dot{Y}_Z(t) = \int_{m_*(t)}^{m_{up}} m_Z(m,Z)\,\Phi(m)\,{\rm SFR}(t-\tau_m)\,dm, \tag{2.13}$$

where the lower limit of integration refers to the mass of a star with a lifetime $\tau_m = t$, $m_Z(m,Z)$ is the total mass of metals (pre-existing and newly synthesized) produced by a star of initial mass m and metallicity Z, Φ(m) is the stellar IMF and m_{up} is the upper mass limit of the IMF.

The chemical network has been extended to implement the evolution of dust (Valiante et al. 2009, 2011). In the two phase ISM, this is described as,

$$\begin{aligned}\dot{M}_d^{\rm diff}(t) &= \mathcal{D}_{vir}(t)\dot{M}_{inf}(t) - \mathcal{D}_{\rm diff}(t)\,M_{\rm ISM}^{\rm diff}(t)/t_{form} - M_d^{\rm diff}(t)/\tau_d \\ &+ \mathcal{D}_{\rm MC}(t)\,M_{\rm ISM}^{\rm MC}(t)/t_{des} + \dot{Y}_d(t) - \mathcal{D}_{\rm diff}(t)\dot{M}_{ej}^{\rm diff}(t),\end{aligned} \tag{2.14}$$

and

$$\begin{aligned}\dot{M}_d^{\rm MC}(t) &= \mathcal{D}_{\rm diff}(t)\,M_{\rm ISM}^{\rm diff}(t)/t_{form} - \mathcal{D}_{\rm MC}(t)\,M_{\rm ISM}^{\rm MC}(t)/t_{des} \\ &- \mathcal{D}_{\rm MC}(t){\rm SFR(t)} + {\rm M_d^{MC}}/\tau_{\rm acc} - \mathcal{D}_{\rm MC}{\rm (t)\dot{M}_{ej}^{MC}(t)},\end{aligned} \tag{2.15}$$

where $\mathcal{D}_{\rm diff}(t) = M_d^{\rm diff}(t)/M_{\rm ISM}^{\rm diff}(t)$ and $\mathcal{D}_{\rm MC}(t) = M_d^{\rm MC}(t)/M_{\rm ISM}^{\rm MC}(t)$ are the dust-to-gas (mass) ratios in the two phases, $\mathcal{D}_{vir}$ is the dust-to-gas ratio of the infalling gas and $\dot{Y}_d$ is the rate at which dust produced by stars is injected into the ISM by AGB stars and SN explosions (Valiante et al., 2009),

$$\dot{Y}_d(t) = \int_{m_*(t)}^{m_{up}} m_d(m,Z)\,\Phi(m)\,{\rm SFR}(t-\tau_m)\,dm \tag{2.16}$$

where $m_d(m,Z)$ is the mass of dust produced by a star with mass m and metallicity Z, and all other quantities are the same as in Eq. 2.13.
For any given element/grain species i, the corresponding yield is computed as in Eqs. 2.13 and

2.16 substituting m_Z and m_d with $m_i(m, Z)$. A presentation of the mass- and metallicity-dependent dust and metal yields will be given in Sections 2.2.3 and 2.2.5.

Grain growth through accretion of gas-phase metals can occur only in the dense phase of the ISM (see Eq. 2.15); following Asano et al. (2013), we model the dust accretion timescale τ_{acc} as:

$$\tau_{acc} \approx 20\,\mathrm{Myr} \times \Big(\frac{\bar{a}}{0.1\,\mu\mathrm{m}}\Big)\Big(\frac{n}{100\,\mathrm{cm}^{-3}}\Big)^{-1}\Big(\frac{T}{50\,\mathrm{K}}\Big)^{-1/2}\Big(\frac{Z}{Z_\odot}\Big)^{-1} \tag{2.17}$$

where $\bar{a}$ is the typical size of dust grains, n is the number density of the gas in the MC phase, T and Z are the temperature and the gas-phase metallicity of the cloud, respectively. Here we assume that in the MC phase $n = 10^3\mathrm{cm}^{-3}$ and $T = 50$ K, so that the accretion timescale from a gas at solar metallicity is 2 Myr (Asano et al., 2013).

The destruction timescale, τ_d, is the lifetime of dust grains destroyed by thermal sputtering in high-velocity ($v > 150\,\mathrm{km\,s^{-1}}$) SN shocks. We assume that dust grains can be destroyed only in the hot diffuse phase of the ISM and that

$$\tau_d = \frac{M_{\mathrm{ISM}}^{\mathrm{diff}}}{\epsilon_d\, M_{\mathrm{swept}}\, R'_{\mathrm{SN}}}, \tag{2.18}$$

where ϵ_d is the destruction efficiency, M_{swept} is the effective ISM mass that is completely cleared of dust by a single SN shock and $R'_{\mathrm{SN}} = f_{\mathrm{SN}} R_{\mathrm{SN}}$ is the effective SN rate for grains destruction, accounting for the possibility that not all the SNe which interact with the ISM are equally efficient at destroying dust (Dwek & Scalo, 1980; McKee, 1989; Tielens, 2005). In what follows, we assume that stars with masses in the range [140-260] $M_\odot$ explode as PISN (Heger & Woosley, 2002). These are very efficient at destroying dust (Nozawa et al., 2006), hence $f_{\mathrm{PISN}} = 1$. Conversely, stars with masses in the range [8-40] $M_\odot$ explode as core-collapse SNe (either faint or ordinary SNe, see Sec. 2.2.3) and are less efficient at destroying dust, $f_{\mathrm{SN}} = 0.15$. The mass M_{swept} can be computed using the Sedov-Taylor solution for an expanding SN in a homogeneous medium with shock velocity v_{sh} (McKee, 1989),

$$M_{\mathrm{swept}} = 6800\, M_\odot \frac{\langle E_{\mathrm{SN}}\rangle / 10^{51}\mathrm{erg}}{(v_{sh}/100\,\mathrm{km\,s^{-1}})^2}, \tag{2.19}$$

where $v_{sh} \sim 200\,\mathrm{km\,s^{-1}}$ is the (minimum) non-radiative shock velocity and $\langle E_{\mathrm{SN}}\rangle$ is the average supernova explosion energy, assumed to be 2.7 $\times 10^{52}$ erg for PISNe and 1.2 $\times 10^{51}$ erg for core collapse SNe. The adopted dust destruction efficiencies are taken from Nozawa et al. (2006) for PISNe and from Jones et al. (1996) for SNe, $\epsilon_d \sim 0.6$ and $\epsilon_d \sim 0.48$ respectively, and assume a reference ISM density of $n_{\mathrm{ISM}} = 1\, cm^{-3}$.

Note that the mass of gas-phase metals can be easily inferred as $M_Z - M_d$.

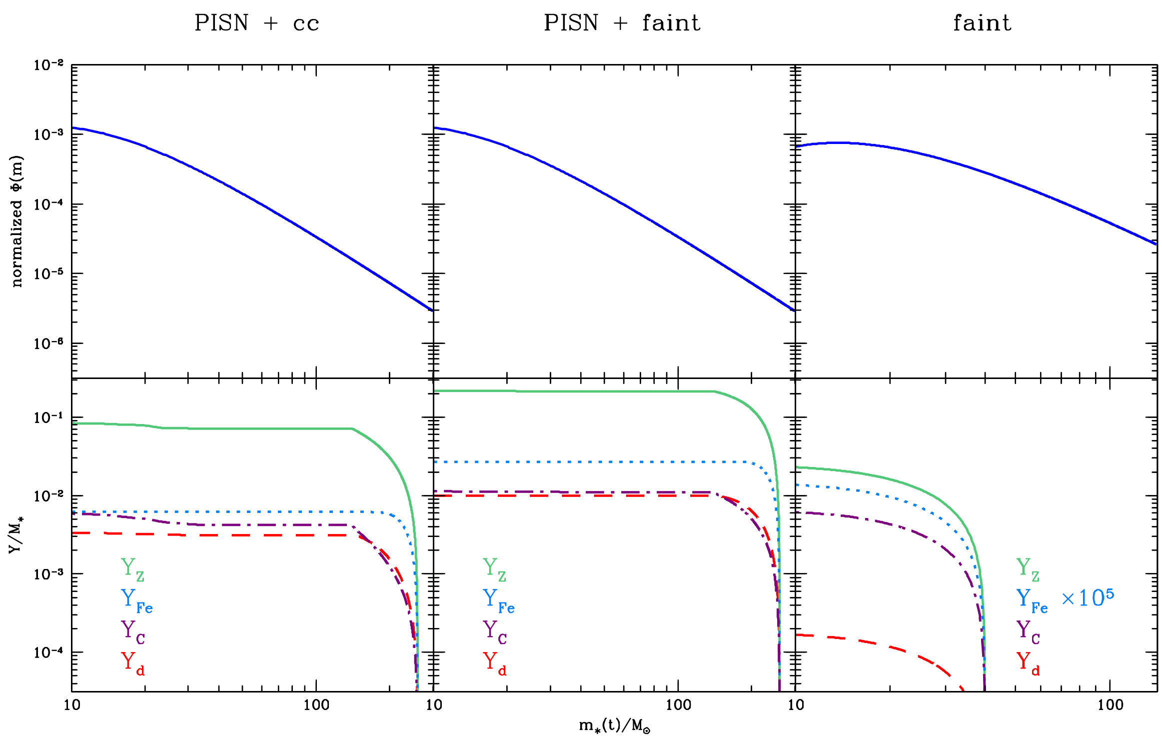

Figure 2.2 *Description of the Pop III models explored. In the upper panels we show the normalized Pop III IMF that we consider and in the bottom panel the corresponding IMF-integrated yields. These are normalized to the stellar mass formed in a single burst and plotted as a function of the minimum stellar mass (see Eqs. 2.13 and 2.16). We show the separate evolution of the total metal (green, solid) and dust (red, dashed) yields and the evolution of the iron (azure, dotted) and carbon (purple, dot-dashed) yields. Left panels: stars form in the mass range [10-300] $M_\odot$ assuming cc SNe yields for masses m < 40 $M_\odot$. Middle panels: stars form in the same mass range but faint SNe yields are considered if m < 40 $M_\odot$. Right panels: stars form in the mass range [10-140] $M_\odot$, excluding the PISN mass range and considering faint SNe yields. Note that in this last case the iron yield is multiplied by a factor 10^5.*

2.2.3 Population III stars

We assume Pop III stars to form according to a Larson-type IMF (Larson, 1998),

$$\Phi(m) = \frac{dN}{dm} \propto m^{\alpha-1} exp\Big(-\frac{m_{ch}}{m}\Big) \tag{2.20}$$

with $\alpha = -1.35$. The value of m_{ch} is chosen in order to have an average mass of Pop III stars of $\sim 40\,M_\odot$ (Hosokawa & Omukai, 2009). In the first model that we explore, Pop III stars are assumed to form with masses in the range [10 - 300] $M_\odot$ with a characteristic mass of $m_{ch} = 20\,M_\odot$. The corresponding Pop III IMF is shown in the upper left panel of Fig. 2.2. We follow the gradual enrichment of the ISM by Pop III stars taking into account their mass-dependent lifetimes (Raiteri et al., 1996; Schaerer, 2002), and consider metal and dust yields from core-collapse SNe ($10\,M_\odot < m_* < 40\,M_\odot$) and PISNe ($140\,M_\odot < m_* < 260\,M_\odot$); outside these two mass ranges stars are assumed to directly collapse to black hole without ejecting the products of their nucleosynthesis. For the purpose of the present study, we follow the evolution of the total mass in metals with the separate contributions of Fe, C and O using the yields of Woosley & Weaver (1995) for core-collapse SNe and of Heger & Woosley (2002) for PISNe. In addition, we also follow the enrichment in dust grains produced in the ejecta of Pop III SNe, using the results by Bianchi & Schneider (2007) for core-collapse SNe and by Schneider et al. (2004) for PISNe. We take into account the partial destruction of the newly formed grains by a reverse shock of moderate intensity (Bianchi & Schneider, 2007), so that approximately 7% of the newly condensed dust mass is able to survive and enrich the ISM (Valiante et al., 2009). In the bottom left panel of Fig. 2.2, we show the Pop III IMF-integrated yields given by Eqs. 2.13 and 2.16 as a function of the minimum stellar mass, $m_*(t)$. Here all the stars are assumed to form in a burst and the total mass ejected is normalized to the total mass of stars formed.

In the second Pop III model that we explore, we keep the same Pop III IMF and mass range as described above but we assume that stars in the $10\,M_\odot < m_* < 40\,M_\odot$ mass range explode as faint SNe, hence are characterized by moderate mixing and strong fallback (Umeda & Nomoto, 2003). For these explosions, we adopt metal and dust yields recently computed by Marassi et al. (2014) and show the corresponding IMF and IMF-integrated yields in the central panels of Fig. 2.2. It is clear from the figure that there are only minor differences between faint and ordinary core-collapse SNe, since massive PISNe are the first to explode and dominate the yields. Only C shows a larger variation, but the difference between the two models is smaller than a factor ~ 2. Finally, in the last model that we explore Pop III stars are assumed to form in the mass range [10 - 140] $M_\odot$ with a characteristic mass $m_{ch} = 32\ M_\odot$ (top right panel), excluding the PISN mass range and assuming faint SNe at m < 40 $M_\odot$. The resulting IMF-integrated yields are show in the bottom-right panel: for stars with $40\ M_\odot < m < 140 M_\odot$ the ejected material completely fallbacks onto the star. Hence stars contribute to the integrated yields only if m < 40 $M_\odot$. While metals/dust/C-yields are a factor ~ 5/20/50 smaller than faint SNe + PISNe case (middle panel), the main feature of faint SNe is the dramatically lower Fe yield (~ 5 orders of magnitude smaller). A summary of the three Pop III models that we consider is given in Table 2.3.

2.2.4 The Pop III/II transition

As we have discussed in Sec. 1.4 and at the beginning of this Chapter, one of the goal of the first part of this Thesis is to investigate the potential of current observations of metal-poor stars in the MW halo to constrain the physical conditions that enable the formation of the first low-mass Pop II stars. The chemical evolution model described above allows to follow the evolution of the mass of gas-phase metals, dust grains, as well as the separate abundances of C, O, and Fe in the 2-phase ISM. Hence, it enables us to investigate the model predictions assuming different Pop III/II transition criteria. In particular:

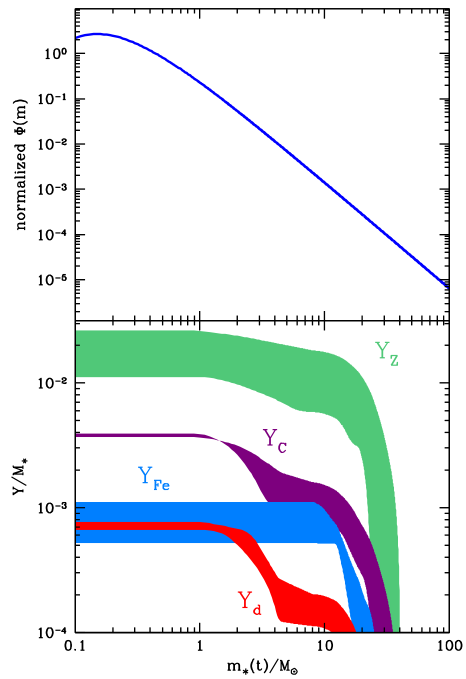

Figure 2.3 *Same as Fig. 2.2 but for Pop II stars. Shaded areas account for metallicity-dependent yields, with* $10^{-4}Z_{\odot} < Z < Z_{\odot}$ *(see text).*

1. *critical metallicity*: low-mass Pop II stars can form when the gas-phase metallicity of MC is larger than $Z_{cr} = 10^{-3.8}\,Z_{\odot}$ (Bromm et al., 2001);

2. *critical dust-to-gas ratio*: Pop II stars form when the dust-to-gas mass ratio of MC is larger than $\mathcal{D}_{cr} = 4.4^{+1.9}_{-1.8}\times10^{-9}$, where the errorbars take into account the modulation due to grain properties (Schneider et al., 2012a).

3. *transition discriminant*: Pop II stars form if the transition discriminant, $\mathrm{D_{tr}} = \log_{10}(10^{[\mathrm{C/H}]} + 0.9\times10^{[\mathrm{O/H}]})$, where [C/H] and [O/H] are the total (gas-phase + dust) C and O abundance in the MC, is larger than $\mathrm{D}_{tr,cr} = -3.5 \pm 0.2$ (Frebel & Norris, 2013).

Table 2.3 lists the models that we have explored using different Pop III/II transition criteria.

2.2.5 Population II stars

Once the criteria for low-mass star formation are met, Pop II stars are assumed to form according to a Larson IMF in the mass range [0.1 - 100] $\mathrm{M}_{\odot}$ with $m_{ch} = 0.35\ M_{\odot}$ (**?**) and we consider their evolution taking into account the mass- and metallicity-dependent stellar lifetimes (Raiteri et al., 1996). For stars with $m_* < 8\,M_{\odot}$, we adopt metal yields from van den Hoek & Groenewegen

Table 2.1 *Observational properties of the MW that we have used to calibrate the free parameters of the model. The existing total mass in metals and dust are derived using values in this Table. Values are taken from: (1) Stahler & Palla (2005); (2) Dehnen & Binney (1998), Brown et al. (2005); (3, 4) Planck Collaboration XXV (2011); (5) Salvadori et al. (2007); (6) Ganguly et al. (2005); (7) Jenkins (2009); (8) Chomiuk & Povich (2011).*

$M_{ISM}^{(1)}$	$M_*^{(2)}$	$M_d^{diff,(3)}$	$M_d^{MC,(4)}$
$(8.0 \pm 2.1)\times10^9 M_\odot$	$(6.3 \pm 1.7)\times10^{10} M_\odot$	$(8.07 \pm 4.56)\times10^7 M_\odot$	$(6.00 \pm 3.78)\times10^7 M_\odot$
$Z_{ISM}^{(5)}$	$Z_{IGM}^{(6)}$	$DtM_{diff}^{(7)}$	$SFR^{(8)}$
$Z_\odot$	$0.25\ Z_\odot$	0.57 ± 0.57	1 - 10 $M_\odot$/yr

(1997) and dust yields for intermediate-mass stars on the AGB phase of the evolution by Zhukovska et al. (2008). Metal and dust yields for massive stars ($12\,M_\odot < m_* < 40\,M_\odot$) have been taken from Woosley & Weaver (1995) and from Bianchi & Schneider (2007), using the proper mass-and metallicity-dependent values. For stars in the mass range $8\,M_\odot < m_* < 12\,M_\odot$, we interpolate between the AGB yields for the largest-mass progenitor and SN yields from the lowest-mass progenitor. Above 40 $M_\odot$, stars are assumed to collapse to black hole without contributing to the enrichment of the ISM. The chosen IMF and the resulting Pop II IMF-integrated yields are shown in Fig. 2.3 (upper and lower panels, respectively). The shaded areas represent how yields vary for different stellar progenitor metallicities (see also Valiante et al. 2009). Similarly to what has been assumed for Pop III dust yields, we take into account the partial destruction by the reverse shock of the newly formed dust in SN ejecta; with this choice, the resulting SN dust masses appear to be in good agreement with available observational data of SNe and SN remnants (Valiante et al., 2014; Schneider et al., 2014).

2.3 Milky Way global properties

Since the contribution of Pop III stars to the total SFR is only relevant at high redshifts, the model predictions for global MW properties and for its progenitors are fairly independent of the adopted Pop III IMF and Pop III/II transition criteria. Fig. 2.4 shows the result obtained for a model where the Pop III/II transition occurs when the dust-to-gas ratio in the dense phase of the ISM exceeds the critical value of $\mathcal{D}_{cr} = 4.4 \times 10^{-9}$ and Pop III stars form according to a Larson IMF with masses in the range $[10 - 140]M_\odot$, i.e. model (f) in Table 2.3. Hereafter we refer to this model as our reference model. Its is clear that metal and dust enrichment prevents Pop III stars from forming at $z \lesssim 12$ and that the star formation history is completely dominated by Pop II stars, with a final SFR in good agreement with the observed value.

The model presented in Sec. 2.2 relies on a number of free parameters, such as the star formation efficiency, ϵ_*, the SN-driven wind efficiency ϵ_w, and the parameters f and α_{MC} that control the 2-phase structure of the ISM. In addition, we have to define the typical density and temperature that characterize the dense phase of the ISM and that define the dust accretion timescale through

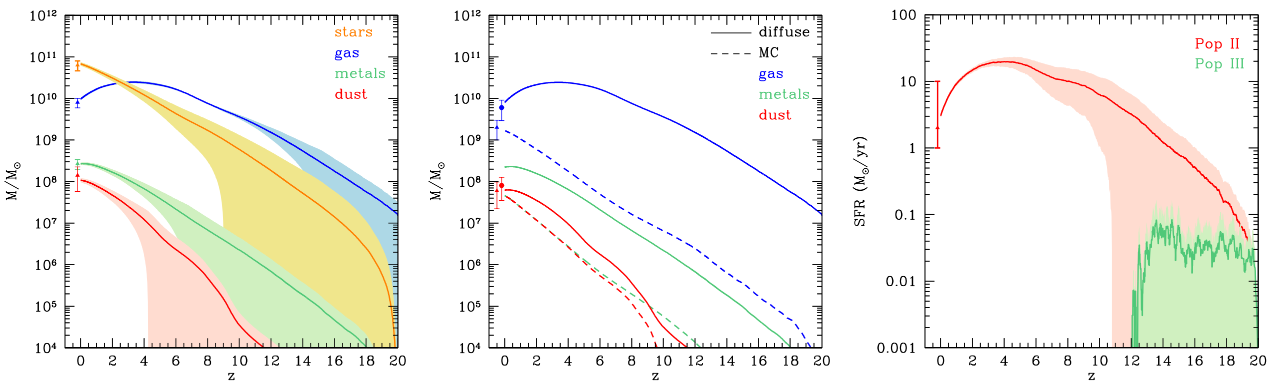

Figure 2.4 *Redshift evolution of the predicted global properties of the MW. Each line represents an average over 50 merger tree realizations with shaded areas representing $1-\sigma$ Poissonian errors. Left panel: gas (blue), star (yellow), metal (green) and dust (red) masses are shown for the fiducial model parameters of Table 2.2. Middle panel: separate evolution of gas (g), metals (m) and dust (d) in the diffuse (solid lines) and MC (dashed lines) ISM phase. Observed quantities at z = 0 are also shown (points with errorbars, see Table 2.1). Right panel: redshift evolution of Pop II (dashed red) and Pop III (solid green) star formation rate for model (f) (see text and Table 2.3).*

Eq. 2.17. Our approach is to constrain their values comparing the model predictions with some observed properties of the MW, such as the current SFR, the existing $M_{\rm ISM}$ and M_*, $M_{\rm ISM}^{\rm MC}$, Z, M_d inferred from observations targeting regions of larger column densities (that we associated to the MC phase) and regions of lower column density (that we associate to the diffuse phase). In Table 2.1, the observational data collected from the literature are listed. Fig. 2.4 shows the results obtained for the selected set of reference parameter values listed in Table 2.2. Each line plotted in the figures has been obtained averaging over 50 independent merger trees of the MW, with shaded regions (where present) showing the 1-σ dispersion. In the left panel of Fig. 2.4, we show the evolution of the total gas, stellar, metal and dust masses in the ISM of the MW, where at $z > 0$ the quantities have been obtained summing over all the individual MW progenitors present at the corresponding redshift. The set of reference parameters selected leads to a final MW stellar and gas masses of $\rm M_* = 7 \times 10^{10} M_\odot$ and $\rm M_{ISM} = 9 \times 10^{9} M_\odot$, in good agreement with the observational data (see Table 2.1). Similarly good is the agreement between the predicted final masses of metals, $\rm M_Z = 2.7 \times 10^8 M_\odot$, and dust $\rm M_d = 1.1 \times 10^8 M_\odot$, and the observational value; note that the data point representing the total mass in metals has been derived from the observed metallicity and gas mass, while the data point of the total dust mass has been computed as the sum of the observed dust masses of dense and diffuse phases (see Table 2.1). By looking at the predicted evolution of such a global properties we can see that at $z = 0$ the 1-σ dispersion among different merger histories becomes smaller than the observational errors. This implies that the global properties are well reproduced not only by the average mean values, but also by each single merger history.

The predicted redshift evolution of the gas, metal and dust masses in the two phases of the ISM are shown in the middle panel of Fig. 2.4. It is clear that the selected values for the f and $\alpha_{\rm MC}$ parameters lead to final masses of cold dense gas and dust masses in the two phase in very good

Table 2.2 *Model parameters adopted in the present study. The first four entries represent common parameters that have been fixed so as to match the observed global properties of the MW. The last three entries show the adopted values for the critical parameters that control the Pop III/II transition.*

ϵ_*	ϵ_w	$\alpha_{\rm MC}$	f	$Z_{\rm cr}$	$\mathcal{D}_{\rm cr}$	$D_{\rm tr,cr}$
0.8	0.0016	1.02	0.4	$10^{-3.8} Z_\odot$	4.4×10^{-9}	-3.5

agreement with the observations. Note that the metal mass shown in this figure represents the total mass in heavy elements, summing metals in the gas-phase and in dust grains. Hence, we find that in the cold dense phase dust accretion is maximally efficient, i.e. at the final redshift all the metals in the gas-phase are depleted on dust (the green-dashed and red-dashed curves overlap). In the right panel of Fig. 2.4, we also show the predicted redshift evolution of the SFR, separating the contribution of Pop III and Pop II stars to the total star formation rate. As already described in Sec. 2.2.1, we assume that only gas in the diffuse phase can be completely ejected out of the halo, as a consequence of mechanical feedback from SNe. Hence, while the gas in the dense molecular phase can be heated and dispersed in the diffuse phase, it is not ejected out of the halo. We explored different mass-loading prescriptions of SN-driven outflows (e.g. assuming that the ejected gas is composed by different mass fractions of diffuse and dense gas), and we find that the results of the model are very similar once a re-calibration of the parameter $\alpha_{\rm MC}$ is made so as to reproduce the existing molecular mass in the MW (see Table 2.1).

2.4 The Milky Way progenitors

Once the free parameters of the model are constrained, we can analyze the properties of the MW progenitors. The idea is to test if the relations between the dust/metal/gas masses predicted for the reference model at different evolutionary stages are consistent with the observed scaling relations. Most of the available data refer to galaxies of different masses in the Local Universe. Hence, a meaningful comparison between MW progenitors at different redshifts and present-day galaxies requires that sources with comparable stellar/dust/gas masses are identified. Hence, we apply different mass selection criteria to the MW progenitors depending on the specific data sample that we consider, as it will be discussed below.

The first sample that we compare with has been analyzed by Corbelli et al. (2012). It refers to galaxies in the Virgo Cluster that have been mapped by the Herschel satellite (HeViCS, Davies et al. 2010, observed at 21 cm and in the CO (1-0) line. The sample comprises 35 late-type galaxies in a dynamical range $\mathrm{Log}\,(M_{\rm gas}/M_\odot) = 8 - 10$. Selecting MW progenitors in the same dynamical range at all redshifts, in the left and middle panels of Fig. 2.5 we compare the model predictions with observations. The behaviour of the simulated progenitors is globally consistent with observed data, with a slope close to the proposed linear regression (dashed lines). The correlation between the dust mass and total gas mass shows that MW progenitors are generally more gas-rich than typical galaxies in the observed sample, probably as a consequence of the

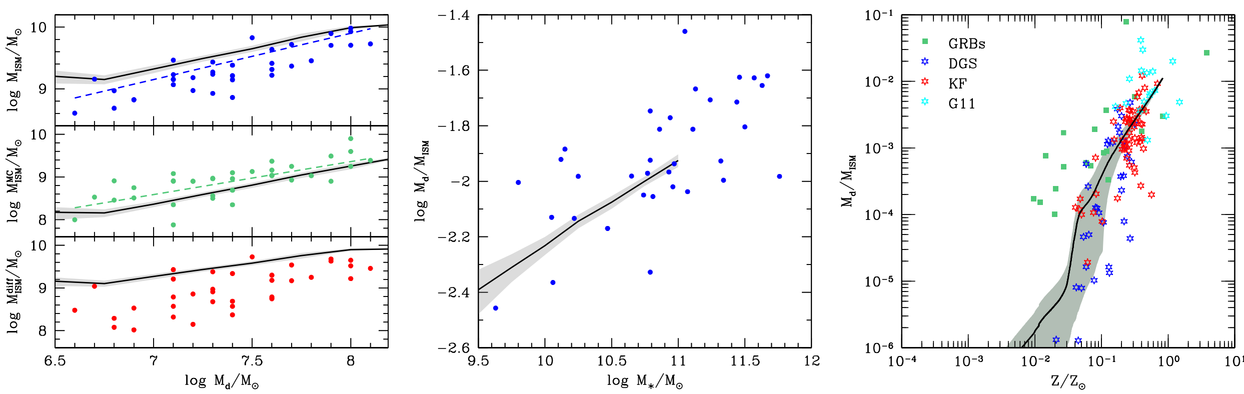

Figure 2.5 *Comparison between the predicted properties of MW progenitors and observations. Solid lines represent averages over 50 independent merger histories of the MW and shaded region the 1-σ dispersion. In the left and middle panels the observational data are taken from Corbelli et al. (2012) with dashed lines indicating the best-fit linear relation for the data. In the right panel, stars refer to the sample analyzed by Rémy-Ruyer et al. (2014) and squares indicate the GRB data sample of Zafar & Watson (2013, see text). Left panel: correlation between the dust mass and the diffuse, molecular and total gas masses (from bottom to top). Middle panel: dust-to-gas mass ratio as a function of the stellar mass. Right panel: dust-to-gas mass ratio as a function of the gas metallicity.*

earlier evolutionary stages of the model galaxies, which lie in the redshift range $0 < z < 4$. It is important to note that galaxies in the Corbelli et al. (2012) sample have been classified to be HI-deficient, probably due to galaxy interactions in the cluster environment where they are embedded. Indeed, the model galaxies show a correlation between the dust and molecular gas masses very close to the observations, while, for a given dust mass, the predicted HI masses are generally a factor ~ 2 larger than observed. This is further confirmed by looking at the middle panel of Fig. 2.5 where the correlation between the dust-to-gas mass ratio and the stellar mass is represented (for the same sample galaxies). Model predictions show that MW progenitors are characterized by a dust-to-gas ratio that grows with the stellar mass, consistent with the observations. Yet, predicted stellar masses are smaller than $M_* \leq 7 \times 10^{10} M_\odot$, which is the final stellar mass predicted for the MW at $z = 0$. Hence, we conclude that although the Corbelli et al. (2012) sample comprises late-type galaxies in the Virgo clusters, 30% of which have stellar masses larger than the MW progenitors investigated by the present model, the general scaling relations that have been inferred from the observations are well reproduced, with differences that can be ascribed to environmental and/or evolutionary effects.

Additional constraints on the model can be obtained by comparing the predicted correlation between the dust-to-gas ratio and the gas metallicity. Recently, this correlation has been measured over a large metallicity range using different samples of local galaxies, such as the KINGFISH survey (KF, Kennicutt et al. 2011), the sample collected by (Galametz et al., 2011, G11), and the Dwarf Galaxy Sample (DGS, Madden et al. 2013). In the right panel of Fig. 2.5, we show the data points from these three surveys as recently collected by Rémy-Ruyer et al. (2014). For a comparison, we also show in the same plot the data collected by Zafar & Watson

Table 2.3 *In this table we identify the models (first row) that we have investigated varying the Pop III stellar IMF, the adopted SN yields (second row), and the Pop III/II transition criterium (third row).*

(a)	(b)	(c)	(d)	(e)	(f)	(g)	(h)	(i)
PISN+cc	PISN+faint	faint	PISN+cc	PISN+faint	faint	PISN+cc	PISN+faint	faint
Z_{cr}	Z_{cr}	Z_{cr}	$\mathcal{D}_{cr}$	$\mathcal{D}_{cr}$	$\mathcal{D}_{cr}$	$D_{tr,cr}$	$D_{tr,cr}$	$D_{tr,cr}$

(2013) over a wide redshift range $0.1 < z < 6.3$ using GRB afterglows. Note that while the dust masses in local samples have been inferred from the FIR/sub-mm emission, GRB afterglows allow to investigate the evolution of dust content in their host galaxies using extinction data. In particular, following Kuo et al. (2013), for each GRB the best-fit extinction curve (LMC-, SMC- or MW-like) is considered and the dust-to-gas ratio is computed from the observed optical depth and gas column density, using the corresponding correction factor. The observed data points indicate that the dust-to-gas ratio grows with the metallicity but with a large scatter, particularly at the lowest metallicities. A similar behaviour is found for the simulated MW progenitors. At low metallicities, dust and metal enrichment proceed proportionally to the stellar yields. When $Z \sim 0.02\,Z_{\odot}$, the accretion timescale is $\tau_{acc} < 100$ Myr, gas-phase metals accretion on dust grains becomes efficient, steepening the correlation between the dust-to-gas ratio and the metallicity, which is mostly driven by grain growth in dense molecular clouds (Kuo et al., 2013; Asano et al., 2013; Zhukovska, 2014). Once all gas-phase metals are accreted, a saturation condition is reached and the simulated behaviour is driven again by the corresponding stellar yields.

2.5 Stellar Archaeology

Hence, we have identified 9 different models that we have tested against the observations: these models are characterized by a common set of parameters (calibrated to match the observed properties of the MW, as discussed in Sec. 2.3 and Table 2.2) but differ by the adopted Pop III stellar mass range and/or Pop III SN yields, and by the assumed criterium controlling the Pop III/II transition. In Table 2.3, we list the properties of each model, identified by a letter running from (a) to (i).

2.5.1 Constraints on the Pop III IMF

In Fig. 2.6, we show a comparison between the observed low-metallicity tail of the MDF and the theoretical prediction obtained by each of the 9 models. Note that we take into account the mass- and metallicity-dependent stellar lifetimes to predict the number of stars that survives down to $z = 0$. Since at [Fe/H] ≥ -2 disk stars can contaminate the sample, the simulated MDF is truncated above [Fe/H] $= -2$ and it is normalized to the total number of stars observed at [Fe/H] ≤ -2. We computed the mean theoretical MDF as the average number of stars in each [Fe/H] bin across the 50 merger histories. The 1-σ dispersion, or standard deviation, is then derived

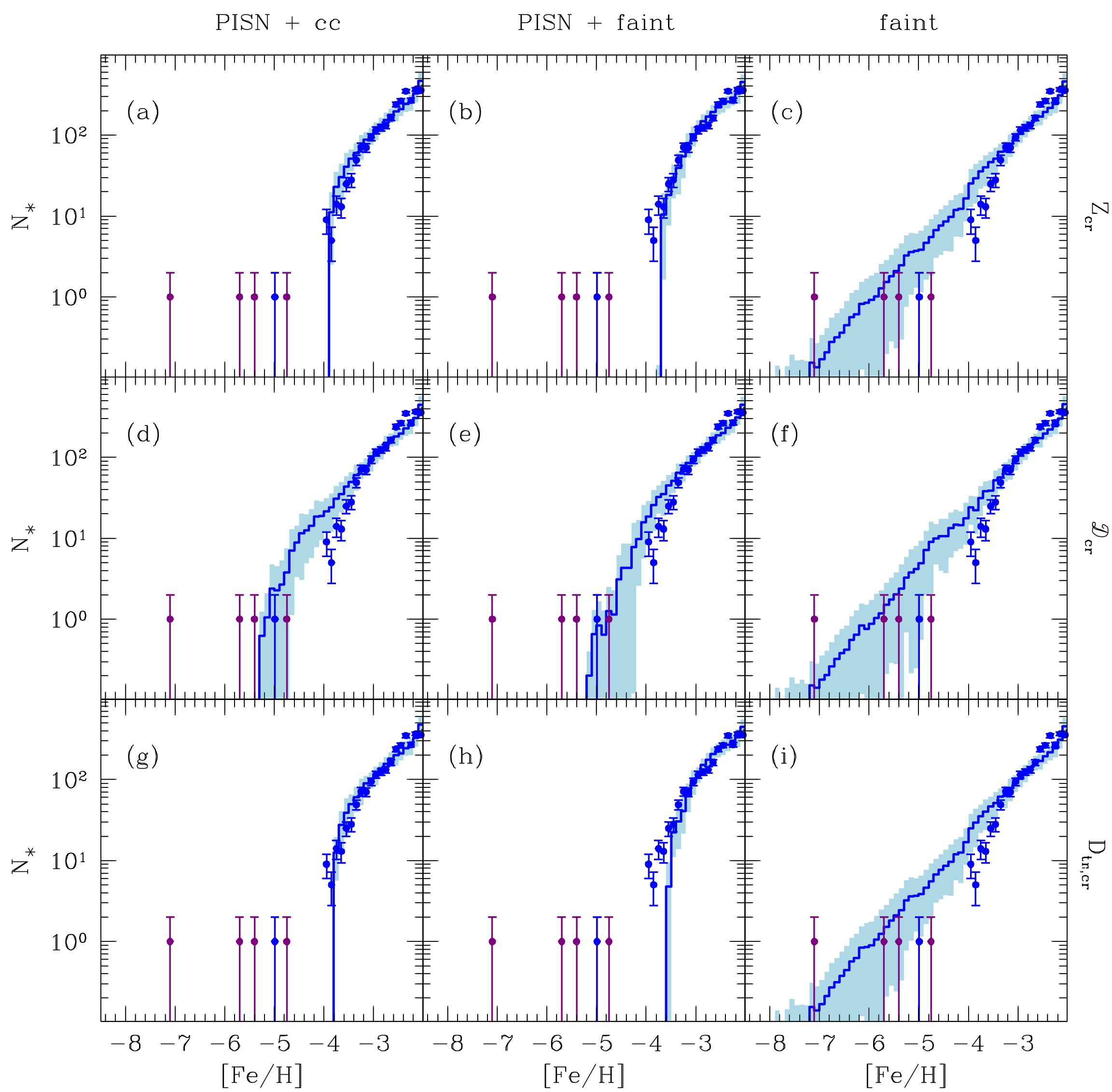

Figure 2.6 *Simulated MDF averaged over 50 merger trees (solid line) with 1-σ dispersion (shaded area) for different Pop III IMF (columns) and for different transition criteria (rows). Points are the observed MDF as in Salvadori et al. (2007) with Poissonian error bars, distinguishing between C-normal (blue) and CEMP (purple) stars. The Pop III/II transition is parametrized with: a critical metallicity (first row) $Z_{cr} = 10^{-3.8} Z_\odot$ (Salvadori & Ferrara, 2012); a critical dust-to-gas ratio (second row) $\mathcal{D}_{cr} = 4.4 \times 10^{-9}$ (Schneider et al., 2012a); a critical transition discriminant (third row) $\mathrm{D}_{tr,cr} = -3.5$ (Frebel & Norris, 2013). The Pop III IMF is taken to extend to: 300 $M_\odot$ with core-collapse SNe (first column); 300 $M_\odot$ with faint SNe (second column); 140 $M_\odot$ with faint SNe (third column). Note that three hyper-iron-poor stars are added with respect to the observed MDF in Salvadori et al. (2007): HE 0557-4840 ([Fe/H] ≈ -4.75, Norris et al. 2007); SDSS J102915+172927 ([Fe/H] ≈ -4.99, Caffau et al. 2011a; the only C-normal star among the hyper-iron-poor stars); SMSS J031300 ([Fe/H] $\lesssim$ -7.1, Keller et al. 2014).*

as the square root of the variance among the 50 merger histories. Once these quantities are evaluated the normalization is done by rescaling the total number of simulated star at [Fe/H] < -2 to the observed value. Note that the same results are obtained by first normalizing the simulated MDF of each realization, and then computing the average MDF and 1-σ dispersion. The data points refer to the joint HK/HES sample that has already been used in previous theoretical works (Salvadori et al., 2007; Salvadori & Ferrara, 2009). For completeness, we have added to the above sample the 5 hyper-iron-poor stars currently known at the time of the writing of this part the work: HE0557-4840 ([Fe/H] = -4.75, Norris et al. 2007), SDSSJ102915+1172927 ([Fe/H] = -4.99, Caffau et al. 2011a, 2012), HE1327-2326 ([Fe/H] = - 5.76, Frebel et al. 2005), HE0107-5240 ([Fe/H] = -5.54, Christlieb et al. 2004), and the recently discovered SMSS J031300 ([Fe/H] < - 7.1, Keller et al. 2014).

Let us focus on the first row of Fig. 2.6, which shows models where the Pop III/II transition is driven by a critical metallicity of $Z_{cr} = 10^{-3.8} Z_{\odot}$ (Salvadori et al., 2007), differing only for the adopted Pop III IMF and corresponding yields (see Table 2.3). In model (a) we assume that Pop III stars form in the mass range [10-300] $M_{\odot}$ according to a Larson IMF with $m_{ch} = 20\,M_{\odot}$. Hence, in this model the two mass ranges where Pop III stars contribute to metal and dust enrichment are $10 M_{\odot} \leq m_* \leq 40\,M_{\odot}$, where we adopt yields of ordinary core-collapse SNe, and $140 M_{\odot} \leq m_* \leq 260 M_{\odot}$, where the stars explode as PISNe. The resulting MDF is very similar to what was found by previous investigations (see Fig. 6 in Salvadori et al. 2007), where a 200 $M_{\odot}$ single-mass Pop III IMF was adopted. This is not surprising because even if we have enlarged the Pop III stellar mass range and relaxed the IRA, the IMF-weighted yields are very similar to those of a single 200 $M_{\odot}$ PISN. For this model, the bulk of observed stars at [Fe/H] $\gtrsim -4$ is very well reproduced, but no star is predicted with [Fe/H] < -4, at odds with the observations. Note that 4 out of the 5 stars currently known with [Fe/H] < -4.5 are CEMP, hence for these stars [Fe/H] is not a good metallicity indicator. Although the interpretation of the origin of CEMP stars is complicated by the fact that these stars do not represent a homogeneous class (see the discussion in Sec. 2.5.3), Pop III SNe in which mixing was minimal and fallback was large have been shown to provide a good match to the observed abundance pattern (Umeda & Nomoto, 2002; Tominaga et al., 2007; Joggerst et al., 2009; Kobayashi et al., 2011; Keller et al., 2014). In these so-called “faint” SNe, the small iron abundance reflects the fact that iron failed to be mixed sufficiently far out to be ejected.

Hence, in model (b) we have adopted the same Pop III IMF as in model (a), but assuming that Pop III stars with masses in the range $10 M_{\odot} \leq m_* \leq 40\,M_{\odot}$ explode as faint core-collapse SNe and contribute to metal and dust enrichment with their specific carbon-rich and iron-poor yields, that we take from the recent study by Marassi et al. (2014). The resulting MDF is shown in the second top panel of Fig. 2.6 and appears to be almost identical to that of model (a); in fact, PISN largely dominate the Fe production and (being more massive) are the first Pop III stars to enrich the ISM. By the time the first faint SNe explode, the gas is already enriched in Fe and their contribution to the low-[Fe/H] tail of the MDF becomes negligible. Hence, the lowest [Fe/H]-bin populated by stars in the theoretical MDF is related to the PISN iron yield, and the observed stars at [Fe/H]< -4.5 are still not reproduced by the model.

If we limit the mass range of Pop III stars to $[10-140]\,M_\odot$, excluding the PISN progenitors mass range, we find the results shown in the third top panel (model c). Iron enrichment is much slower than previous cases, being dominated by faint SNe. As a result, the tail of the MDF extends down to [Fe/H] ~ -8, well into the observed range of the most iron-poor stars. Although for this model the average MDF agrees with the observations at $[\mathrm{Fe/H}] \leq -4.75$ and at $[\mathrm{Fe/H}] \geq -3.5$, at least within the $1-\sigma$ scatter, there is a clear excess of stars with $-4.75 < [\mathrm{Fe/H}] < -3.5$ with respect to the data, which indicate a sharp change of slope in the MDF. The smooth, continuous growth of the simulated MDF for $-8 \leq [\mathrm{Fe/H}] \leq -2$ suggests that additional physical processes, beyond those implemented in the present study, are at work. Most notably, radiative feedback effects that may prevent the gas in the first mini-halos from cooling, delaying or inhibiting star formation (Karlsson, 2006; Salvadori & Ferrara, 2012).

2.5.2 Constraints on the Pop III/II transition

The second and third rows of Fig. 2.6 show (for the same set of Pop III IMF and SN yields discussed above), the predicted MDF when the Pop III/II transition occurs above a minimum dust-to-gas ratio or transition discriminant. Models (d) and (e) show that the condition $\mathcal{D} \geq \mathcal{D}_{\rm cr}$ allows to populate the MDF down to $[\mathrm{Fe/H}] \sim -5.4$ even when Pop III stars are assumed to form with masses [10 - 300] $M_\odot$ and independently of the adopted core-collapse SN yields. Yet, even in this case the mass range of PISN progenitors has to be excluded from the Pop III IMF in order to reproduce the low-[Fe/H] tail down to the lowest observed values (model f).

Finally, for a given Pop III IMF and SN yields, a Pop III/II transition occurring when $\mathrm{D}_{tr} > \mathrm{D}_{tr,cr}$ does not lead to appreciable differences in the MDF with respect to models where low-mass stars form when $Z > Z_{cr}$: compare models (g), (h), (i), with models (a), (b), (c), respectively. In conclusion, faint SNe are needed to reproduce the low-metallicity tail of the MDF.

In Fig. 2.7 we show the redshift evolution of the [Fe/H] within MW progenitor halos selected from a single merger-tree realization, whose results at $z = 0$ are most similar to the average ones. The three panels refer to models which adopt the same Pop III IMF ([10 -140] $M_\odot$ mass range with faint SNe) but different Pop III/II transition criteria: models (c), (f) and (i), from left to right. Depending on the gas properties, at each time, individual MW progenitors can either form Pop III stars (green starred points) or Pop II stars (C-normal or C-enhanced). Following the definition of Beers & Christlieb (2005), metal-poor stars are classified as CEMP if $[\mathrm{C/Fe}] \geq 1$. The solid black line represents the [Fe/H] evolution in the IGM. Points along this line identify halos that have virialized from the IGM and that form stars for the first time; hence their gas properties reflect the corresponding properties of the IGM at that redshift. At each given redshift, points above the black solid line represent halos that have been self-enriched by their stellar populations or that have inherited their [Fe/H] through mergers with highly enriched progenitors. Conversely, points below the black solid line represent progenitors whose [Fe/H] has been diluted below the IGM value by mergers with un-polluted halos (that have virialized at an earlier epoch but have not formed stars yet). The horizontal-dashed and vertical-dotted lines

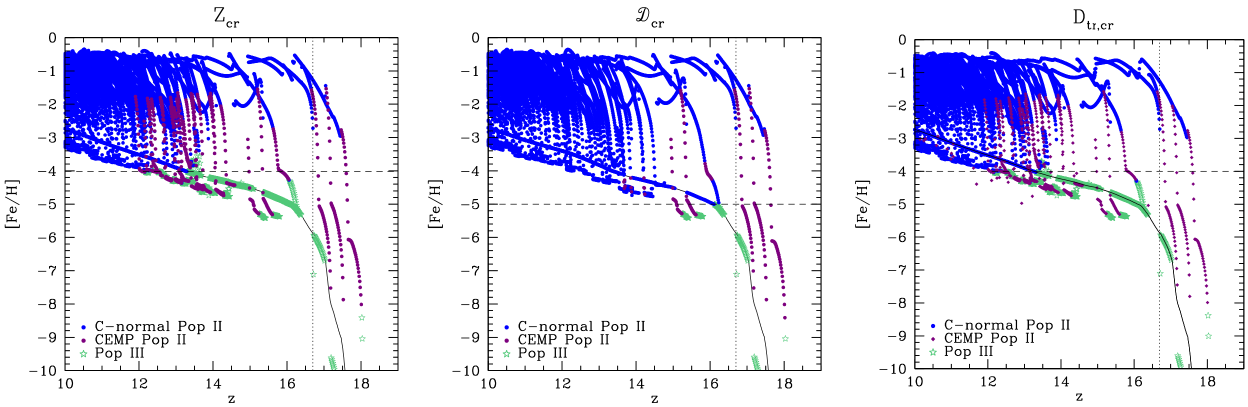

Figure 2.7 *Redshift evolution of the [Fe/H] within MW progenitors for a single merger tree realization for models (c), (f), and (i) (from left to right). Green stars identify MW progenitor halos that are forming Pop III stars, while filled purple diamonds and filled blue dots are progenitor halos forming carbon-enhanced and carbon-normal Pop II stars, respectively. The black solid line represents the evolution of the [Fe/H] of the IGM. The vertical dotted lines indicate the redshift at which the IGM is characterized by [C/Fe] > 1.0, so that the gas in halos virializing from the IGM after this redshift are characterized by a C-normal elemental abundance. The horizontal dashed lines represent the [Fe/H] at which the IGM exceeds the value of the critical parameter controlling the Pop III/II transition.*

mark two important evolutionary phases: the first one identify the [Fe/H] when the critical Pop III/II transition criterium is met in the IGM. Hence, halos that virialize after this epoch can only form Pop II stars (see the transition from starred points to dots along the IGM line). This occurs at different epochs in the three models as a consequence of the different Pop III/II transition criteria: at $z \sim 14$ for models (c) and (i), and at $z \sim 16$ for model (f). The nature of the first Pop II stars that form in newly virialized halos depends on the [C/Fe] content of the IGM: the vertical-dotted line marks the redshift at which [C/Fe] = 1; for all the three models, the first Pop II stars that form in newly virialized halos are always C-normal. The typical evolutionary tracks in the first progenitors show that Pop III stars continue to form until the first faint SNe explode and enrich the ISM above the critical threshold for Pop II star formation. The first Pop II stars are typically C-enhanced, reflecting the yields of faint-SNe. Once the first Pop II cc-SNe explode, the [C/Fe] is decreased to < 1 and the subsequent generations of Pop II stars are C-normal.

Comparing the three panels, it is evident that when [Fe/H] < -5 the evolutionary tracks do not depend on the transition criterium, resulting in a very similar low-[Fe/H] tail of the MDF. The major difference is in the duration of the Pop III star formation epoch, that is shorter when a dust-driven transition is adopted. As a result, in model (f) C-normal Pop II stars can form at $-5 <$ [Fe/H] < -4 due to early enrichment from Pop II cc-SNe. Conversely, in models (c) and (i) a larger fraction of Pop II stars are C-enhanced due to the larger contribution to gas enrichment from faint Pop III SNe. Hence, tighter constraints on the Pop III/II transition can be set by separating the contribution to the MDF of C-normal and C-enhanced stars. The

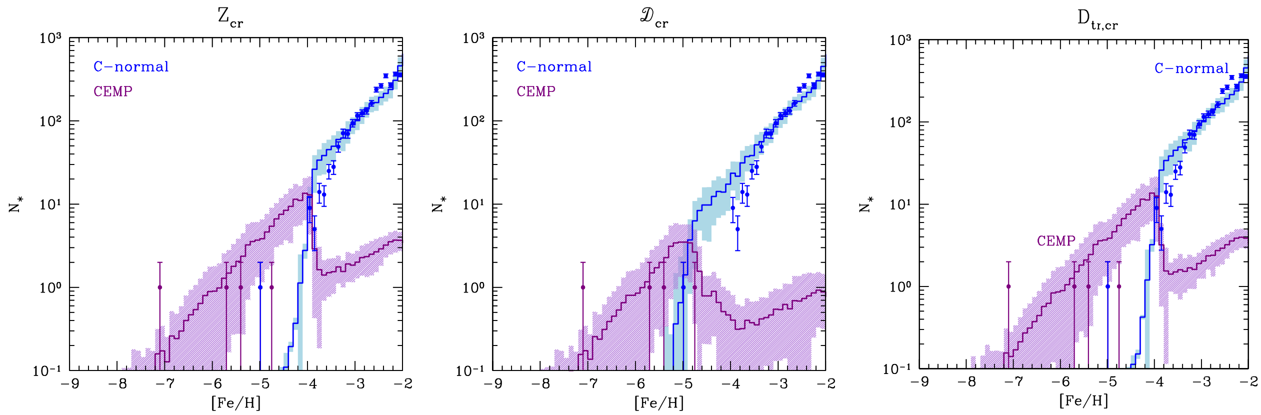

Figure 2.8 *The contribution of C-enhanced stars ([C/Fe] ≥ 1.0, purple line and shaded region) and C-normal stars ([C/Fe] < 1, blue line and shaded region) to the theoretical MDF for models (c), (f), and (i), from left to right (see text).*

results are shown in Fig.2.8. It is clear that CEMP stars dominate the low-[Fe/H] tail of the simulated MDF for all three models, as a result of the dominant role played by Pop III faint-SN in the first metal enrichment. However, it is only in model (f), where Pop II stars from when $\mathcal{D} \geq \mathcal{D}_{cr}$, that the MDF of C-normal stars extends to [Fe/H] ~ -5.4, accounting for the observed data point that corresponds to SDSS J102915+172927, the only C-normal star at these low-[Fe/H] currently known (Caffau et al., 2011a). Note that the predicted [C/Fe] for C-normal stars with [Fe/H] < -4.5 ranges between 0 and +1, consistent with the observed properties of SDSS J102915+172927 (Caffau et al., 2011a). Conversely, the MDF of C-normal stars predicted by models (c) and (i) do not extend below [Fe/H] ~ -4.5. Hence, as already discussed by Caffau et al. (2011a), Schneider et al. (2012b) and Klessen et al. (2012), the formation of SDSS J102915+172927 must have followed alternative pathways, beyond that associated to fine-structure line cooling.

We conclude that the observed MDF at [Fe/H] ≤ -2 and the relative fraction of C-normal and C-rich stars at [Fe/H] ≤ -4.5 seem to indicate model (f) as the best-fit scenario, where the transition is driven by the dust-to-gas ratio, Pop III stars preferentially form in the mass range [10 - 140] $M_{\odot}$ and explode as faint SNe. The contribution of PISNe to the first enrichment, if present, must have been largely sub-dominant. Finally, the formation of the first low-mass stars must have been triggered by processes occurring at metallicities below those normally assumed to enable efficient fine-structure line cooling, such as by dust cooling and fragmentation. Other models can be excluded because they do not predict the existence of stars and/or C-normal stars below [Fe/H] < -4, at odds with observations.

2.5.3 Carbon enhancement

Spectroscopic studies of metal poor stars in the HK, HES and more recently SDSS samples have convincingly shown that the frequency of CEMP stars grows with decreasing [Fe/H], being $\sim 20\%$ at $[Fe/H] < -2$ and as large as 80% at $[Fe/H] < -4$ (Yong et al., 2013b; Spite et al., 2013; Norris et al., 2013; Lee et al., 2013). However, the increasing frequency of CEMP stars with declining [Fe/H] is not equally important for the different sub-classes which characterize CEMP stars. Generally, CEMP stars are classified as CEMP-s/rs and CEMP-no (Beers & Christlieb, 2005) depending on the over-abundant presence of s or rs-process elements (such as Ba, Sr, Eu) or no-overabundance of neutron-capture elements. It has been suggested that these differences may provide clues to the nature of their likely progenitors. In particular, CEMP-s and CEMP-rs have abundance patterns that suggest mass-transfer from an AGB companion in a binary systems (Suda et al., 2004; Masseron et al., 2010). Indeed, long-term radial-velocity observations show that a large percentage of CEMP-s/rs stars are binaries (Lucatello et al., 2005). However, the abundance pattern of the CEMP-no stars is difficult to explain as caused by a mass transfer from an AGB companion and the nature of their progenitors is still largely debated. Using a homogeneous chemical analysis of 190 metal-poor stars Yong et al. (2013a) and Norris et al. (2013) have recently investigated a sample of CEMP-no stars with $[Fe/H] < -3$. They conclude that the observed chemical abundances are best explained by models which invoke the nucleosynthesis of Pop III SNe with mixing and fallback, the so-called "faint" SNe that we have discussed in Sections 1.4 and 2.5.1. In addition, observations show that the relative fraction of CEMP-no and CEMP-r/rs stars depends on [Fe/H], with CEMP-no stars representing the large majority ($\sim 90\%$) of CEMP stars at $[Fe/H] < -3$ (Aoki et al., 2007; Masseron et al., 2010).

In the left panel of Fig. 2.9 we show [C/H] as a function of [Fe/H] for 86 stars with $[Fe/H] < -3$ out of the full sample of 190 stars analyzed by Yong et al. (2013a, see their Table 1), to which we have added SDSSJ102915+1172927 (Caffau et al., 2011a) and SMSS J031300 (Keller et al., 2014), that were not present in the original sample. Following Norris et al. (2013), we have divided the sample into CEMP-no and CEMP-r/s stars, where the latter class includes CEMP-s, CEMP-r, and CEMP-rs stars. The grey shaded area marks the region of the plane where the stars are classified as C-normal ($[C/Fe] < 1$, according to our definition). It is clear from the figure that CEMP-no stars represent the dominant population of CEMP stars at $[Fe/H] < -4.5$, but that the number of CEMP-r/s stars grows with [Fe/H] and become the dominant class of CEMP stars at $[Fe/H] > -3.5$. This is clearly seen in the right panel of the same figure, where we plot the observed fraction of CEMP stars (number of CEMP stars divided by the total number of stars) and of CEMP-no stars for four different [Fe/H] bins. To be consistent with Yong et al. (2013b), we have considered a single bin for the 5 hyper-iron-poor stars with $[Fe/H] < -4.5$ and then three bins in the $-4.5 \leq [Fe/H] \leq -3$ range, chosen to contain an almost equal number of stars (~ 28, 27, and 28 from the lowest to the highest [Fe/H]-bin). Empty data points refer to the fraction of CEMP stars and filled data points to the fraction of CEMP-no stars only. We find that the fraction of CEMP stars decreases from 0.8 to 0.3, but that the decrease becomes much steeper when only CEMP-no stars are considered, going from $\sim 80\%$ to less than 5%. Yet, the predicted fraction of CEMP stars for the fiducial case (f) shows an even steeper decline. It is important to stress that in our model CEMP stars can form only as a result of the enrichment from Pop III faint SNe, as we do not consider mass-transfer effects in stellar binaries. Hence, strictly speaking, we can not predict the existence of CEMP-r/s stars and the simulated data must be compared only to the CEMP-no fraction. However, while the model is consistent with the data (within 1-σ) for three out of the four [Fe/H]-bins, it under-predicts the fraction of CEMP-no stars at $[Fe/H] \geq -4.5$. We will further discuss this point in the next section. Here we comment on the fact that we have conservatively assumed that only Pop III stars can end their life as faint SNe, whereas faint SNe have been directly observed in the local Universe, like SN1997D (Turatto et al., 1998), which has been considered as a prototype for this class of objects, and many more examples (see the compilation in Pastorello et al. 2006 and Fraser et al. 2011), including the dimmest sources SN 1999br (Pastorello et al., 2004) and SN 2010id (Gal-Yam et al., 2011). Additional indication that a population of faint SNe may exist come from the non-detection of SNe associated with low-redshift long-GRBs (Della Valle et al. 2006). It is difficult to directly estimate the fraction of faint SN from current SN data, due to the bias against dim sources in present samples. Using very local ($\leq$ 10Mpc) data, Horiuchi et al. (2011) have estimated that the fraction of dim SNe, defined as SNe with an absolute magnitude of M > -15, ranges between 3%-20%. However, they also find that a fraction as large as 30%-50% is required in order to reconcile the observed SN rate with that predicted from the observed cosmic SFR. Assuming a similar fraction of Pop II faint-SNe we can better match the observed data points, as shown in Fig. 2.9.

2.6 Discussion

Several theoretical models aimed to investigate the early enrichment and star formation history of the MW have been developed and compared to observations of the most metal-poor stars in the Galactic halo and nearby dwarf galaxies.

Tumlinson (2006) and Salvadori et al. (2007) first applied semi-analytic approaches to hierarchical structure formation to follow the chemical enrichment of the Milky Way and to put constraints on the properties of the first stars. Tumlinson (2006) explored different Pop III IMFs and found good agreement with the Galactic halo MDF for top-heavy IMFs sharply peaked in the mass range of core-collapse SNe, [12-70] $M_{\odot}$, and for $Z_{cr} \sim 10^{-4} Z_{\odot}$. Salvadori et al. (2007) investigated the Pop III/II transition by adopting different Z_{cr} values and Pop III masses. They showed that the persistent non-detection of metal-free stars implies that Pop III stars have masses $m > 0.9\,M_{\odot}$, or that $Z_{cr} > 0$. By assuming that Pop III stars explode as PISN, moreover, they found that a value of $Z_{cr} \sim 10^{-4} Z_{\odot}$ is required to correctly reproduce the observed MDF at $[Fe/H] > -4$, although the existence of hyper-iron-poor stars cannot be explained. By using an upgraded version of the model, which includes the physics of mini-haloes along with an analytical prescription to account for the inhomogeneous reionization and metal enrichment of the Galactic Medium, Salvadori & Ferrara (2012) showed that the low-Fe tail of the Galactic halo MDF shifts towards lower [Fe/H] values when Pop III stars are assumed to explode as faint SNe of $m = 25\,M_{\odot}$ (Kobayashi et al., 2011). By studying the chemical abundances of very metal-poor damped Lyα absorption systems in the context of the Milky Way formation, these authors

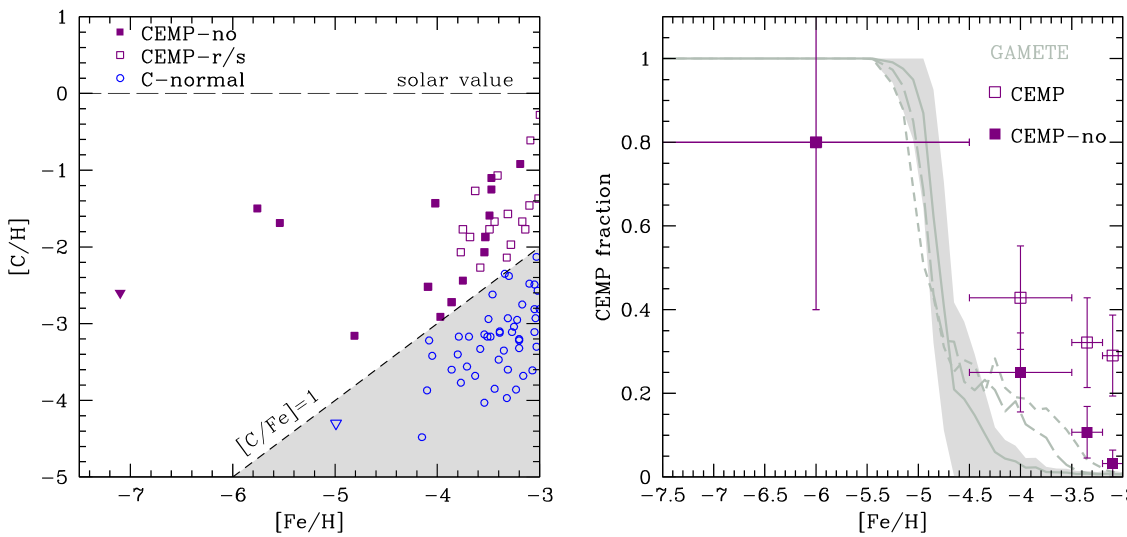

Figure 2.9 *Left panel: C abundance as a function of [Fe/H] for the C-normal (empty blue points), CEMP-no (filled purple squares) and CEMP-r/s (empty purple squares) stars taken from the sample of Yong et al. (2013a). We also added to their sample the CEMP-no SMSS J031300 star (purple filled triangle, Keller et al., 2014) and the C-normal SDSSJ102915+1172927 star (blue empty triangle, Caffau et al., 2011a, 2012). The dashed line corresponding to [C/Fe] = 1 marks the separation between C-normal (grey area) and C-rich stars, following the definition of Beers & Christlieb (2005). The horizontal dashed line shows the solar C-abundance. Right panel: observed fraction of CEMP (empty squares) and CEMP-no (filled squares) stars in four different [Fe/H]-bins. Errorbars on the y-axis represent Poissonian errors on the number of stars in each bin and on the x-axis reflect the amplitude of the [Fe/H] bin (see text). The grey solid line shows the predicted fraction of CEMP-no stars for the fiducial model (f) averaged over 50 merger trees. The shaded region shows the 1-σ dispersion among different merger histories. The long-dashed and dashed lines show the results obtained when 30% and 50% of the SN type II progenitors are assumed to explode as faint SNe, respectively.*

demonstrate that faint SNe dominate the chemical enrichment at [Fe/H] < −5, while at higher [Fe/H] the gas (and stars) chemical abundances are only partially imprinted by this pristine stellar generation.

Tumlinson (2007) considered an IMF dependent on the temperature of the CMB as a way to explain the [Fe/H]-dependence of CEMP-s/rs stars, assumed to form in stellar binaries. Komiya et al. (2009, 2010); Komiya (2011) addressed the difference between the hyper-iron-poor stars at [Fe/H] < -4.5 and stars with [Fe/H] > -4.5 in the context of hierarchical galaxy formation: they examine the possibility that hyper-iron-poor stars could originate by low-mass Pop III stars whose surface is polluted by accretion of enriched gas from the halo ISM. They discussed the total number of stars with [Fe/H] < -3 as well as the shape of the MDF and found the best agreement for a high-mass IMF (assumed to be the same for all stellar populations) and accounting for the formation of stellar binaries, without evoking a transition in the stellar IMF.

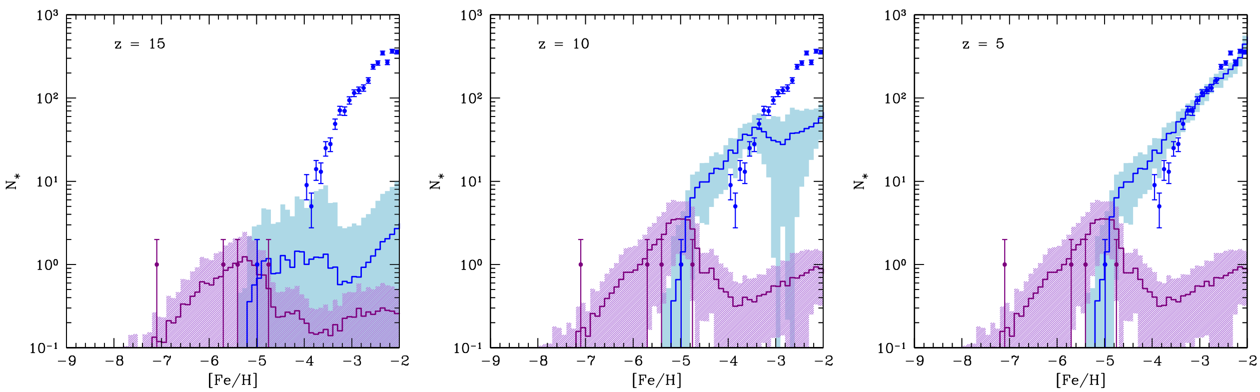

Figure 2.10 *Redshift evolution of the MDF for the fiducial model (f), separating the contribution of CEMP and C-normal stars (z = 15, 10, 5 from left to right).*

Additionally, they explored different SN yields obtaining good fit to the MDF for all adopted SNe nucleosynthesis model.

More recently, Cooke & Madau (2014) have suggested that carbon-enhanced metal poor stars may originate in mini-halos polluted by low-energy supernovae which produce a super-solar ratio of [C/Fe]. Conversely high-energy SNe that produce a near-solar ratio of [C/Fe] completely unbound the gas in the first mini-halos, thereby suppressing the formation of a second generation of stars (Sec. 1.3). The recent detection of SDSS J001820.5-093939.2, a truly second-generation star at [Fe/H] ~ -2.5 exhibiting the clear imprint of PISNe (Aoki et al., 2014), suggests that this is not the case. This observation demonstrates that these stars do exist but they are extremely rare and they are likely hidden at higher [Fe/H], as already suggested by Salvadori et al. (2007).

In this Chapter we investigate the hierarchical formation of the MW and its chemical enrichment in metals, Fe, C and O. For the first time, we develop and apply a chemical evolution model in a 2-phase ISM, to account for grain growth in cold, dense clouds and grain destruction in the hot, diffuse medium. This allows us to investigate the Pop III/II transition under different physical conditions, including the effect of line-cooling (Z_{cr} or $D_{tr,cr}$), and dust-grains ($\mathcal{D}_{cr}$). We explore different IMFs and different SNe yields for Pop III stars. The existence of hyper-iron-poor, carbon-enhanced stars is a strong indication that faint SNe (rather than PISNe and cc SNe, which give a too strong Fe enrichment) dominate the nucleosynthetic output of Pop III stars. The assumption of Pop III faint SNe is crucial not only to extend the tail of the MDF down to [Fe/H] < -7 , but also to reproduce the dependence of the CEMP fraction on [Fe/H]. In the present study, we have not considered a binary origin of CEMP stars. For this reason, we have compared our results with observed samples excluding CEMP-s/r/rs stars; yet, as shown in Fig. 2.9, the fraction of CEMP stars predicted in our simulated samples tends to under-predict the observed data at $-4.5 <$ [Fe/H] < -3. As we have discussed in the previous section, the observations could be reproduced if 30%-50% of Pop II SNe are assumed to be faint, consistent with the observational indication of local SN samples (Horiuchi et al., 2011). The inclusion of mini-haloes into the model is also expected to increase the number of carbon-enhanced stars, providing a better agreement with the data. However, we should note that the $-4.5 <$ [Fe/H] < -3

range is where the simulated MDF provides the worst agreement with the observations, showing no sign of the observed change of slope between the roughly constant tail at [Fe/H] < -4 and the steep rise at [Fe/H] > -4. On the contrary, even for the best-fit model, the simulated MDF is characterized by a single slope in the range $-7 <$ [Fe/H] < -2, although with an increasing scatter between different merger tree realizations at [Fe/H] < -4. This is not surprising given that we have assumed that radiative feedback has suppressed star formation in mini-halos, which are instead predicted to be the progenitors of today lived ultra-faint dwarf galaxies (Salvadori & Ferrara, 2009) and to have played a major role in the early metal enrichment and reionization of the Milky Way environment (Salvadori et al., 2014). In the present study, instead, stars form only in halos with virial temperatures $T_{vir} \geq 2 \times 10^4$K that can cool via Ly-$\alpha$ cooling. Hence the shape of the MDF at low [Fe/H] mostly reflects the efficiency of star formation and metal enrichment in these more massive progenitors. Yet, Fig. 2.10 shows that Pop II stars that populate the bins at $-5 <$ [Fe/H] < -3 in the simulated MDF mostly form at redshifts $15 \leq z \leq 10$, where we expect radiative feedback to play a major role in self-regulating the efficiency of star formation and metal enrichment in mini-halos (Salvadori & Ferrara, 2012).

2.7 Conclusions

In this Chapter, we have presented a new version of the semi-analytical code GAMETE and some first applications of this new model to Stellar Archaeology. For the first time, we follow the star formation history and the enrichment in metals and dust of the MW galaxy along its hierarchical evolution. Using a 2-phase description of the ISM in each progenitor galaxy of the MW, we can follow the evolution of the atomic and molecular gas components and the separate evolution of metals and dust grains in these two phases. In particular, dust grains are destroyed by interstellar SN shocks in the hot diffuse phase, but are shielded against destruction and grow in mass by accreting gas-phase metals in the dense, molecular phase. We show that:

- The model is characterized by 4 free parameters (efficiencies of star formation and SN winds and two additional parameters which regulate the mass transfer between the diffuse and molecular phases) that have been calibrated so as to reproduce the observed properties of the MW at $z = 0$.

- Using this fiducial set of parameters, the simulated progenitors of the MW follow the scaling relations between the gas (total, dense and diffuse) and dust, and between the dust-to-gas ratio and stellar mass inferred from observations of Virgo cluster galaxies (Corbelli et al., 2012); in addition, it also predicts a relation between the dust-to-gas ratio and metallicity that is in very good agreement with observations of different samples of local galaxies (Rémy-Ruyer et al., 2014) and GRB-host galaxies at $0.1 \leq z \leq 6.3$ (Zafar & Watson, 2013).

- When applied to Stellar Archaeology, the simulated MDF is very sensitive to the adopted Pop III IMF and metal yields. Current observations seem to require a largely sub-dominant contribution from Pop III PISN to early metal enrichment, favouring Pop III stars with masses in the range [10 - 140] $M_{\odot}$ which explode as faint SNe.

- The separate contribution of C-normal and CEMP stars to the MDF is sensitive to the critical conditions that are assumed to control the Pop III/II transition. This analysis confirms the expectations that C-normal stars with [Fe/H] < -4.5, such as J102915+172927 (Caffau et al., 2011a), can form only if the transition is driven by dust, when $\mathcal{D} \geq \mathcal{D}_{cr} = 4.4 \times 10^{-9}$.

- Our fiducial model predicts a steep decline of the CEMP fraction with [Fe/H], consistent with the data, but under-predicts the fraction of CEMP stars in the range $-4.5 \leq$ [Fe/H] ≤ -3, suggesting the additional contribution from Pop II faint SNe to C-enrichment.

- The change of slope in the low-[Fe/H] tail of the observed MDF can not be explained by chemical and mechanical feedback effects, and may be due to additional physical processes that regulates the efficiency of star formation in the first star-forming regions. Most likely, radiative feedback associated to the rising UV-background that inhibits star formation by photo-dissociating molecular hydrogen and/or suppressing gas infall in the first mini-halos (Sec. 1.3).

According to this last point and to what described in Sec. 2.6, in the next Chapter we will analyze how the incluson of star forming mini-halos and of a self-consistent description of their Pop III star formation, affect the shape of the MDF and the number and the relative fraction of CEMP-no stars.

3

Limits on Pop III star formation with the most iron-poor stars

In the previous Chapter we discussed the possibility to reproduce the Galactic halo MDF by means of the data-constrained semi-analytical code GAMETE, which reconstructs the possible merger trees of a MW-like DM halo from $z = 20$ to $z = 0$. GAMETE follows the star formation process and the chemical enrichment of the MW along the merger tree, accounting for both metals and dust. The code has been calibrated to reproduce the global properties of the MW (Sec. 2.3) and has been used to set some possible constraints on the nature of the Pop III stars by means of careful comparisons with available observations of ancient and metal-poor stars in the Galactic halo (Sec. 2.5).

In the study presented in Ch. 2, however, we limited the analysis to the star formation in Ly-α cooling halos, although in the standard ΛCDM model for structure formation, the first stars formed at $z \approx 20$ in low-mass DM "mini-halos", with total masses $M \approx [10^6 - 10^7]\,M_{\odot}$ and virial temperatures $T_{vir} < 10^4$ K (e.g. Abel et al., 2002; Bromm, 2013, for a recent review), where stellar feedback has stronger effects (Sec. 1.3): H_2 photo-dissociated by Lyman Werner photons (LW, $E = 11.2 - 13.6$ eV) and gas infall suppression in low temperature mini-halos born in ionized ($T > 10^4$ K) cosmic regions. Hence many galaxy formation models neglect star-formation in these low-mass systems (e.g. Bullock et al. 2015). However, mini-halos likely played an important role in the early Universe, being the nursery of the first stars and the dominant halo population, which likely regulated the initial phases of reionization and chemical-enrichment (e.g. Salvadori et al., 2014; Wise et al., 2014). Accounting for the star-formation in mini-halos is thus an essential step to study the early phases of galaxy evolution and the impact on current stellar sample of "second-generation" stars, which formed out of gas polluted by the first stars.

In this Chapter, we investigate the impact of the Pop III IMF on the properties of CEMP and C-normal stars by accounting for star-forming mini-halos. To this aim, we further develop the model to catch the essential physics required to self-consistently trace the formation of stars in mini-halos by including:

1. a star-formation efficiency that depends on the gas temperature, gas metallicity, and formation redshift of mini-halos, and on the average value of the LW background;
2. a random sampling treatment of the IMF of Pop III stars, which inefficiently form in mini-halos;
3. a suppression of gas infall in mini-halos born in ionized regions, using a self-consistent calculation of reionization.

This Chapter is organized as follows: in Sec. 3.1 we summarize the main features of our cosmological model, mainly focusing on the new physics implemented here. Model results are presented in Sec. 3.2, where we show the effects of different physical processes on the Galactic halo MDF and on the fraction of Carbon-enhanced vs Carbon-normal stars. Finally, in Sec. 3.3, we critically discuss the results and provide our conclusions.

3.1 Description of the model

Here we briefly recap the main features of the semi-analytical code GAMETE which were extensively treated in Ch. 2 (see Sec.2.1 and 2.2 for a more detailed description) and introduce in full detail the model implementations that we made for the purpose of this work.

The cosmological merger tree model GAMETE traces the star-formation history and chemical evolution of MW-like galaxies (i.e. $M_{\rm MW} = 10^{12} M_{\odot}$) from redshift $z = 20$ down to the present-day, by reconstructing a statistical significant sample of 50 independent merger histories of the MW dark matter halo by using a binary Monte Carlo code (Sec. 2.1) based on the EPS theory (e.g. Bond et al., 1991) and accounting for both halo mergers and mass accretion (Salvadori et al., 2007). The 50 possible MW merger histories we reconstruct resolve mini-halos down to a virial temperature $T_{vir} = 2 \times 10^3 K$.

The star-formation and chemical evolution history of the MW is then traced along the merger trees (see Sec. 2.2 for a more detailed description). Due to less efficient gas cooling, the star formation efficiency in mini-halos ($T_{vir} < 10^4$K), ϵ_{MH}, is smaller than that of Ly-α cooling halos ($T_{vir} \geq 10^4$K), ϵ_* (see Sec. 3.1.1).

Once stars are formed, we follow their subsequent evolution using mass- and metallicity-dependent lifetimes (Raiteri et al., 1996), metal (van den Hoek & Groenewegen, 1997; Woosley & Weaver, 1995; Heger & Woosley, 2002) and dust (Schneider et al., 2004; Bianchi & Schneider, 2007; Marassi et al., 2014, 2015) yields. Chemical evolution is followed in all star-forming halos and in the surrounding MW environment enriched by SN-driven outflows regulated by a wind efficiency ϵ_w, which represents the fraction of SN explosion energy converted into kinetic form (Salvadori et al., 2008). While ϵ_w is assumed to be the same for all dark matter halos, the ejected mass is evaluated by comparing the SN kinetic energy with the halo binding energy. Following

Eq. 9 of Salvadori et al. (2008), we thus have:

$$\frac{dM_{ej}}{dt} \propto \frac{\epsilon_w}{v_c^2} \tag{3.1}$$

where v_c is the halo circular velocity (Eq. 1.11).

As discussed in 2.2, the evolution of the ISM in each progenitor halo is described as follows:

- we assume the ISM to be characterized by two phases: (*i*) a cold, *dense* phase that mimic the properties of molecular clouds (MCs). In this dense phase star-formation occurs and dust grains accrete gas-phase metals. (*ii*) A hot, *diffuse* phase that exchanges mass with the MW environment through gas infall and SN winds. In this diffuse phase, SN reverse shocks can partially destroy newly produced dust grains (Bianchi & Schneider, 2007; Marassi et al., 2015; Bocchio et al., 2016).

- Chemical evolution is described separately in the two phases, but the mass exchange between the dense and diffuse ISM is taken into account, through the condensation of the diffuse phase and the dispersion of MCs which return material to the diffuse phase. These processes are regulated by two additional free parameters, as described in Sec. 2.2.1.

- According to the results presented in Sec. 2.5.2, the transition from massive, Pop III stars to "normal" Pop II stars is assumed to be driven by dust grains (e.g. Schneider et al., 2002) and to occur when the dust-to-gas mass ratio in the dense phase exceeds the critical value $\mathcal{D}_{cr} = 4.4 \times 10^{-9}$ (Schneider et al., 2012a)

- Pop III stars form with masses in the range $[10-300]\, M_\odot$ according to a Larson-type IMF:

$$\Phi(m) = \frac{dN}{dm} \propto m^{\alpha-1} \exp\left(-\frac{m_{ch}}{m}\right) \tag{3.2}$$

  with $m_{ch} = 20\, M_\odot$ and $\alpha = 1.35$. We assume that chemical enrichment (metals and dust) is driven by Pop III stars with masses $[10 - 40]\, M_\odot$, that explode as faint SNe, and by stars with masses $[140 - 260]\, M_\odot$, that explode as PISNe (e.g. Heger & Woosley, 2002; Schneider et al., 2004; Takahashi et al., 2016), as described in Sec. 2.2.3. We recall that these "faint SNe" experience mixing and fallback during their evolution (Bonifacio et al., 2003). As a consequence, when they explode as SNe, they eject small amounts of Ni^{56} (and hence Fe) with respect to other light elements, such as C (e.g. Umeda & Nomoto, 2003; Iwamoto et al., 2005; Tominaga et al., 2007; Marassi et al., 2014; Ishigaki et al., 2014). The Fe and C yields adopted in this work (Marassi et al., 2014, 2015) are in agreement with the findings of other groups that assumed similar faint SN models (e.g. Iwamoto et al., 2005; Tominaga et al., 2007; Ishigaki et al., 2014). Note that other scenarios have been proposed for the evolution of Pop III stars in this relatively low mass range, such as the rapidly rotating "spinstars" (e.g. Meynet et al., 2006; Maeder et al., 2015). Still, even in these cases, the yields of Fe and C are very similar to those produced by the faint SNe adopted in this work.

- Pop II stars form according to a Larson IMF with $m_{ch} = 0.35\, M_\odot$, $\alpha = 1.35$, and masses in the range $[0.1 - 100]\, M_\odot$. Their contribution to chemical enrichment is driven by AGB stars ($2\, M_\odot \leq m_{\rm PopII} \leq 8 M_\odot$) and by ordinary core-collapse SNe ($8\, M_\odot < m_{\rm PopII} \leq 40\, M_\odot$).

A detailed description of the basic features of the model can be found in the aforementioned papers. In the next subsections we illustrate how we implemented star-formation in H_2 cooling mini-halos.

3.1.1 Gas cooling in mini-halos

The gas cooling process in mini-halos relies on the presence of molecular hydrogen, H_2, which can be easily photo-dissociated by photons in the LW band. Several authors have shown that ineffective cooling by H_2 molecules limits the amount of gas that can be converted into stars, with efficiencies that decrease proportional to T^3_{vir} (e.g. Madau et al., 2001; Okamoto et al., 2008). For this reason, models that account for mini-halos, typically assume that in these small systems the star-formation efficiency is reduced with respect to more massive Lyman-α cooling halos, and that the ratio between the two efficiencies is a function of the virial temperature, $\epsilon_{MH}/\epsilon_* = 2[1 + (T_{vir}/2 \times 10^4\,{\rm K})^{-3}]^{-1}$ (e.g. Salvadori & Ferrara, 2009, 2012). This simple relation is illustrated in the right panels of Fig. 3.1 (dashed lines).

However, the ability of mini-halos to cool down their gas not only depends on T_{vir}, but also on their formation redshift, on the gas metallicity, and on the LW flux, $J_{\rm LW}$, to which these systems are exposed. In this work, we compute the mass fraction of gas that is able to cool in one dynamical time following a simplified version of the chemical evolution model of Omukai (2012). For a more detailed description of the model and of the gas-cooling processes that we have considered, we refer the reader to the Appendix A of Valiante et al. (2016)[1].

In Fig. 3.1 we show the resulting efficiencies, ϵ_{MH}, normalized to ϵ_* for different gas metallicities (left), mini-halo virial temperatures (right) and LW flux. The different lines show different mini-halo formation redshifts. When the LW background is neglected, i.e. $J_{21} = J_{LW}/(10^{-21}{\rm erg/cm^2/s/Hz/sr}) = 0$ (upper panels), we can clearly see the dependence of ϵ_{MH}/ϵ_* on: (*i*) the formation redshift, (*ii*) the gas metallicity (left), and (*iii*) the virial temperature (right). As a general trend, we find that the smaller are these quantities, the lower is the gas-cooling efficiency of mini-halos. At $T_{vir} \geq 10^4$ K, Lyman-α cooling becomes efficient and $\epsilon_{MH}/\epsilon_* = 1$. When $J_{21} \sim 1$ (middle panels), gas cooling is partially suppressed due to H_2 photo-dissociation. When $z > 8$, the gas is dense enough to self-shield against the external LW background, and ϵ_{MH} decreases only by $\approx$1 dex with respect to the $J_{21} = 0$ case. When $z \leq 8$, gas cooling is completely suppressed in $T_{vir} < 10^4$ K systems, unless they are already enriched to $Z \sim Z_\odot$. This

[1]Here we correct the derivation of the cooling time (Eq. A2 in Valiante et al. 2016) by dividing Eq. 19 of Madau et al. (2001) for Ω_m. This enhances the star formation efficiencies shown in their Fig. A1-A4 (see Fig. 3.1).

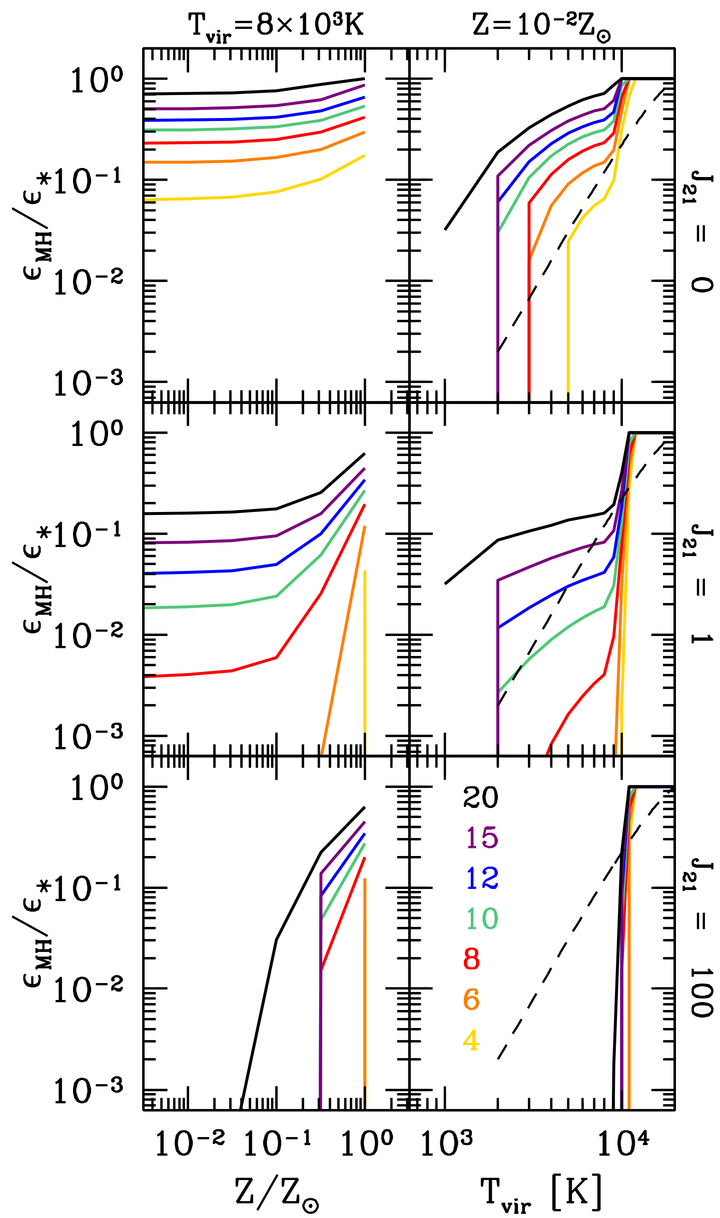

Figure 3.1 *The ratio between the star-formation efficiency in mini-halos, ϵ_{MH}, and the constant efficiency of Lyman-α cooling halos ϵ_* (see text). The colored lines represent different mini-halos formation redshifts (z = 20, 15, 12, 10, 8, 6, 4, from top to bottom, as explained in the legenda). Upper, middle and lower panels show the results assuming $J_{21} = J_{LW}/(10^{-21}\mathrm{erg/cm^2/s/Hz/sr})$ = 0, 1 and 100, respectively. Left panels: dependence on the gas metallicity for a fixed T_{vir} = 8×10^3 K; at $Z < 10^{-2.5} Z_\odot$ the ratio ϵ_{MH}/ϵ_* is constant. Right panels: dependence on the virial temperature, for a fixed Z = $10^{-2} Z_\odot$. The dashed lines show the z-independent relation used in Salvadori & Ferrara (2009, 2012).*

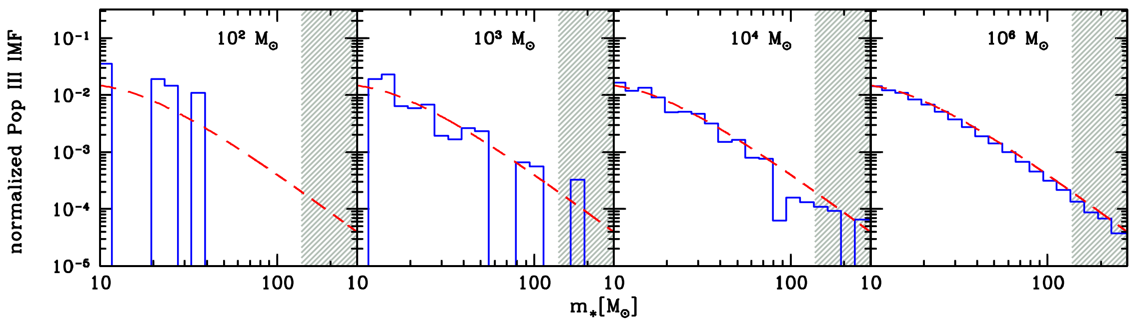

Figure 3.2 *Comparison between the intrinsic IMF of Pop III stars (red dashed lines) and the effective mass distribution resulting from the random sampling procedure (blue histograms). In each panel, the IMF is normalized to the total stellar mass formed, with* $M^{\rm tot}_{\rm PopIII} = (10^2, 10^3, 10^4, 10^6)\, M_\odot$ *(from left to right). The grey shaded areas indicate the progenitor mass range of PISNe (see text).*

is consistent with the minimum halo mass to form stars assumed in Salvadori & Ferrara (2009, 2012). Similarly, when mini-halos are exposed to a stronger LW flux, $J_{21} \sim 100$ (lower panels), gas cooling is allowed only at $z > 8$ in highly enriched mini-halos, which have $Z \gtrsim 10^{-1.5} Z_\odot$. In what follows, we will use the results shown in Fig. 3.1 to self-consistently compute the star-formation efficiency of mini-halos in our merger trees.

3.1.2 Stochastic Pop III IMF

The mass of newly formed stars in a given dark matter halo depends on the gas mass and star formation efficiency. In low-mass systems the available mass of gas can be strongly reduced with respect to the initial mean cosmic value, Ω_b/Ω_M, because of SN-driven outflows and radiative feedback processes (e.g. Salvadori & Ferrara, 2009). Furthermore, due to the reduced cooling efficiency mini-halos (see Fig. 3.1), the total stellar mass formed in each burst is small, $M^{\rm tot}_{\rm PopIII} < 10^4\, M_\odot$. In these conditions, the resulting stellar mass spectrum will be affected by the incomplete sampling of the underlying stellar IMF. This effect can be particularly relevant for Pop III stars, which have masses in the range $[10 - 300] M_\odot$ (e.g. Hirano et al., 2014). Hence, we adopt a random-selection procedure, the result of which is illustrated in Fig. 3.2.

The stars produced during each burst of star-formation are randomly selected within the IMF mass range, and they are assumed to form with a probability that is given by the IMF normalized to the total mass of stars formed in each burst. In Fig. 3.2 we show the comparison between the randomly-selected and the intrinsic IMF for total stellar masses of $M^{\rm tot}_{\rm PopIII} = (10^2, 10^3, 10^4, 10^6)\, M_\odot$. When $M^{\rm tot}_{\rm PopIII} \gtrsim 10^5\, M_\odot$ the overall mass range can be fully sampled and the intrinsic IMF is well reproduced. On the other hand, the lower is the stellar mass formed, the worse is the match between the sampled and the intrinsic IMF. In particular, when

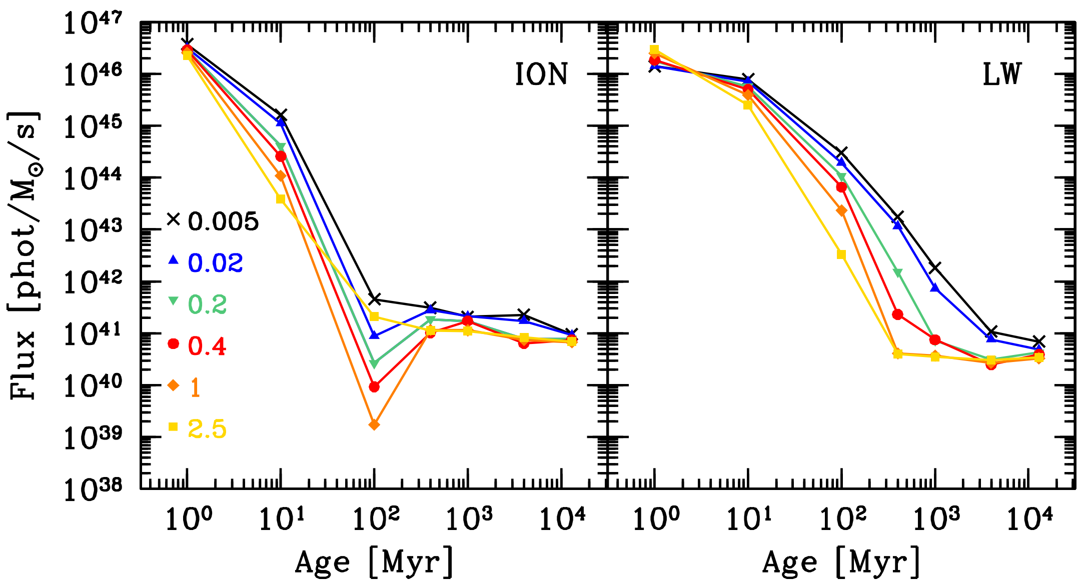

Figure 3.3 *Ionizing (left) and LW (right) photon luminosities per unit stellar mass of Pop II stars as a function of stellar age (Bruzual & Charlot, 2003). Different colors refer to different metallicities as shown by the labels: $Z/Z_\odot$ = 0.005, 0.02, 0.2, 0.4, 1, 2.5 (black crosses, blue up-triangles, green down-triangles, red dots, orange diamonds, gold squares).*

$M^{\rm tot}_{\rm PopIII} \leq 10^3\,M_\odot$, it becomes hard to form Pop III stars with $m_{\rm PopIII} = [140-260]M_\odot$ (PISN progenitor mass range). We find that while almost 100% of the halos forming $10^4 \rm M_\odot$ Pop III stars host ≈ 9 PISNe each, only 60% of the halos producing $10^3 \rm M_\odot$ of Pop III stars host *at most* 1 PISN. Thus, we find that the number of PISN is naturally limited by the incomplete sampling of the stellar IMF.

3.1.3 Radiative feedback

To self-consistently account for the effect of radiative feedback processes acting on mini-halos, we compute the amount of radiation in the LW band (11.2-13.6 eV) and ionizing (> 13.6 eV) bands produced by star-forming halos along the merger trees. We take time- and metallicity-dependent UV luminosities from Bruzual & Charlot (2003) for Pop II stars and from Schaerer (2002) for Pop III stars[2].

Input values used for Pop II stars of different stellar metallicities are shown in Fig. 3.3 as a function of stellar ages. As expected, the UV luminosity is largely dominated by young stars and depends on stellar metallicity, as more metal poor stars have harder emission spectra. In the first 10 Myr, the ionizing photon rate drops from $> 2\times10^{46}$ phot/s/$M_\odot$ to $< 2\times10^{45}$ phot/s/$M_\odot$,

[2]We use the photon luminosities from Table 4 of Schaerer (2002) for metal-free stars.

while the rate of LW photons remains approximately constant at $\sim 10^{46}$ phot/s/$M_{\odot}$. Therefore, although initially lower, after 10 Myr the rate of LW photons emitted becomes higher than that of ionizing photons.

In the following, we describe how we compute the LW and ionizing background and how we account for reionization of the MW environment. Given the lack of spatial information, we assume that the time-dependent LW and ionizing radiation produced by stars build-up a homogeneous background, which (at each given redshift) affects all the (mini-)halos in the same way.

LW background

The cumulative flux observed at a given frequency $\nu_{\rm obs}$ and redshift $z_{\rm obs}$ can be computed by accounting for all stellar populations that are still evolving at $z_{\rm obs}$ (Haardt & Madau, 1996):

$$J(\nu_{\rm obs}, z_{\rm obs}) = (1 + z_{\rm obs})^3 \frac{c}{4\pi} \int_{z_{\rm obs}}^{\infty} dz \left|\frac{dt}{dz}\right| \epsilon(\nu', z)\, e^{-\tau(\nu_{\rm obs}, z_{\rm obs}, z)} \tag{3.3}$$

where

$$\left|\frac{dt}{dz}\right| = \{H_0(1 + z)[\Omega_{\rm m}(1 + z)^3 + \Omega_\Lambda]^{1/2}\}^{-1}, \tag{3.4}$$

$\nu' = \nu_{\rm obs}(1 + z)/(1 + z_{\rm obs})$, $\epsilon(\nu', z)$ is the comoving emissivity at frequency ν' and redshift z, and $\tau(\nu_{\rm obs}, z_{\rm obs}, z)$ is the MW environment optical depth affecting photons emitted at redshift z and seen at redshift $z_{\rm obs}$ at frequency $\nu_{\rm obs}$ (Ricotti et al., 2001).

To obtain the average flux in the LW band, we integrate Eq. (3.3) between $\nu_{\rm min} = 2.5 \times 10^{15}$ Hz (11.2 eV) and $\nu_{\rm max} = 3.3 \times 10^{15}$ Hz (13.6 eV):

$$J_{\rm LW}(z_{\rm obs}) = \frac{1}{\nu_{\rm max} - \nu_{\rm min}} \int_{\nu_{\rm min}}^{\nu_{\rm max}} d\nu_{\rm obs}\; J(\nu_{\rm obs}, z_{\rm obs}). \tag{3.5}$$

Following Ahn et al. (2009), we write the mean attenuation in the LW band as:

$$e^{-\tau(z_{\rm obs}, z)} = \frac{\int_{\nu_{\rm min}}^{\nu_{\rm max}} e^{-\tau(\nu_{\rm obs}, z_{\rm obs}, z)}\, d\nu_{\rm obs}}{\int_{\nu_{\rm min}}^{\nu_{\rm max}} d\nu_{\rm obs}}, \tag{3.6}$$

so that,

$$J_{LW}(z_{\rm obs}) = (1 + z_{\rm obs})^3\; \frac{c}{4\pi} \int_{z_{\rm obs}}^{z_{\rm screen}} dz \left|\frac{dt}{dz}\right| \epsilon_{LW}(z)\, e^{-\tau(z_{\rm obs}, z)}. \tag{3.7}$$

where $\epsilon_{LW}(z)$ is the emissivity in the LW band. Eq. 3.7 is integrated up to $z_{\rm screen}$, that is the redshift above which photons emitted in the LW band are redshifted out of the band (the so-called "dark screen" effect).

In the top panel of Fig. 3.4, we show the redshift evolution of the LW background predicted by the fiducial model (see Sec. 3.1.4 and 3.2). We find that at $z \sim 18$ the average LW background is already $J_{21} \approx 10$, thus strongly reducing the star-formation in $T_{vir} < 10^4$ K mini-halos. The point shown at $z = 0$ is the average LW background in the Galactic ISM, and it has been computed from Eq. 2 of Sternberg et al. (2014). The value refers to a LW central wavelength of 1000 Å, while the errorbar represents the variation interval of J_{21} corresponding to all wavelengths in the LW band (i.e. from 912 Å to 1108 Å). Although the J_{21} background we have obtained is consistent with this data, at high-z our calculations likely overestimate J_{21}. In fact, at any given redshift all LW photons are assumed to escape from star-forming galaxies but they are retained into the MW environment. Yet, the mean free path of LW photons ($\approx$ 10 Mpc, e.g. Haiman et al., 1997) is larger than the physical radius of the Milky Way. In particular, we assume that the MW and its progenitor halos evolve in a comoving volume $\approx 5\ \mathrm{Mpc}^3$, which we estimate at the turn-around radius (see Salvadori et al., 2014). Hence our code simulates a biased region of the Universe, the high density fluctuation giving rise to the MW and its progenitors. For this reason, the LW flux we obtain is consistent with that found by Crosby et al. (2013) who consider a similar volume. On the other hand, the predicted J_{21} is larger than those obtained by cosmological simulations of the Universe, which account for larger volumes (e.g. Ahn et al., 2009; O'Shea et al., 2015; Xu et al., 2016). However, as we will show in Sec. 3.2, such a strong difference in the LW background has a very small impact on our results.

Reionization
Photons with energies > 13.6 eV are responsible for hydrogen (re)ionization. At any given redshift, we compute the ionizing photon rate density, $\dot{n}_{\rm ion}(z)$, by summing the ionizing luminosities over all active stellar populations and dividing by the MW volume, $\approx 5\ \mathrm{Mpc}^3$. The filling factor $Q_{\rm HII}$, i.e. the fraction of MW volume which has been reionized at a given observed redshift $z_{\rm obs}$, is computed following Barkana & Loeb (2001):

$$Q_{\rm HII}(z_{\rm obs}) = \frac{f_{\rm esc}}{n^0_{\rm H}} \int_{z_{\rm obs}}^{z_{\rm em}} dz \left|\frac{dt}{dz}\right| \dot{n}_{\rm ion}\, e^{F(z_{\rm obs},z)} \tag{3.8}$$

with

$$F(z_{\rm obs}, z) = -\alpha_{\rm B}\, n^0_{\rm H} \int_{z_{\rm obs}}^{z} dz' \left|\frac{dt}{dz'}\right| C(z')\,(1+z')^3 \tag{3.9}$$

where $f_{\rm esc}$ is the escape fraction of ionizing photons, $F(z_{\rm obs}, z)$ accounts for recombinations of ionized hydrogen, and $n^0_{\rm H}$ is the present-day hydrogen number density in the MW environment, which is $\approx$ 5 times larger than in the IGM. In Eq. 3.9, α_B is the case B recombination coefficient[3], and $C(z)$ is the redshift-dependent clumping factor, which is assumed to be equal to $C(z) = 17.6\, e^{(-0.10\, z+0.0011\, z^2)}$ (Iliev et al., 2005).

Following Salvadori et al. (2014), we assume an escape fraction for ionizing photons $f_{\rm esc}$=0.1, which provides a reionization history that is complete by $z \sim 6.5$, fully consistent with recent data. This is illustrated in the lower panels of Fig. 3.4, where we show the redshift evolution of the volume filling factor of ionized regions and the corresponding Thomson scattering optical depth. In addition, Salvadori et al. (2014) show that the same reionization history appears consistent with the star-formation histories of dwarf satellites of the MW.

[3]We assume $\alpha_B = 2.6 \times 10^{-13}\ \mathrm{cm}^3/\mathrm{s}$, which is valid for hydrogen at $T = 10^4$ K, e.g. Maselli et al. (2003).

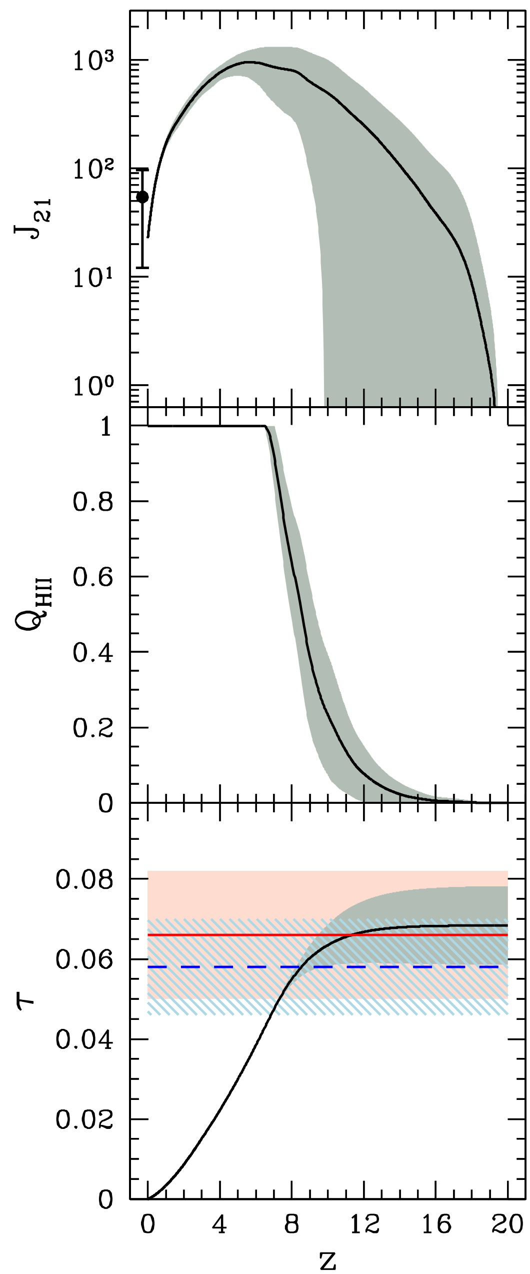

Figure 3.4 *Redshift evolution of the LW flux (upper panel), the volume filling factor of ionized regions (middle panel) and the corresponding Thomson scattering optical depth (lower panel) predicted by the fiducial model and obtained by averaging over 50 MW merger histories (solid lines). The shaded areas show the 1-σ dispersion among different realizations. The point with error bar at $z = 0$ represents an estimate of the specific intensity of the isotropic UV radiation field in the Galactic ISM (Sternberg et al., 2014). The red-solid horizontal line shows the Planck measurement (Planck Collaboration et al., 2015) with 1-σ dispersion (horizontal filled shaded area). The more recent measurement (Planck Collaboration et al., 2016) is plotted as a blue-dashed horizontal line with 1-σ dispersion (horizontal striped-dashed shaded area).*

3.1.4 Model calibration

The free parameters of the model are assumed to be the same for all dark matter halos of the merger trees and they are calibrated by comparing the "global properties" of the MW as observed today with the average mean value over 50 independent merger histories. In particular, we match the observed mass of stars, metals, dust and gas, along with the star formation rate (see Table 2.1). All these observed properties are simultaneously reproduced by assuming the same model free parameters of Table 2.2.

3.2 Results

In this section we present the results of our models by focusing on the MDF and on the properties of CEMP-no stars at [Fe/H] < -3. Since we did not model mass transfer in binary systems, we will completely neglect CEMP-s/(rs) stars in our discussion (see also Salvadori et al., 2015). Note that in this Chapter we select CEMP stars as those stars which show [C/Fe] > 0.7, following the definition of Aoki et al. (2007), while in the previous Chapter we adopted the definition of Beers & Christlieb (2005) with [C/Fe] > 1. In addition, here we use a coherent sample of high resolution data in the [Fe/H] < -3 range, including all the 9 CEMP stars currently known at the time of writing this part of the work (with respect to the 5 stars used in Sec. 2.5) at [Fe/H] < -4.5 (see Sec. 1.4.1).

The comparison between simulated and observed MDFs is shown in Fig. 3.5 where the two functions have been normalized to the same number of observed stars at [Fe/H] < -3.

By inspecting all the panels, from left to right, we can see how the different physical processes included in the models affect the shape of the MDF, along with the predicted number of CEMP-no stars. For each model, the figure shows how the results vary when we assume Pop III stars to form with masses in the range $[10 - 140]\, M_{\odot}$ (top panels), where only faint SNe can contribute to metal enrichment, and $[10 - 300]\, M_{\odot}$ (bottom panels), where both faint SNe and PISNe can produce and release heavy elements.

Panels (a, e) show the results for models with "sterile" mini-halos, i.e. assuming that systems with $T_{vir} < 10^4$ K are not able to form stars. As discussed in Sec. 2.5, we see that both the low-Fe tail of the MDF, at [Fe/H] < -5, and the number of CEMP-no stars, can only be reproduced when the Pop III stars have masses $m_{\rm PopIII} = [10 - 140]\, M_{\odot}$ (panel a). This is because CEMP-no stars form in environments enriched by the chemical products of primordial faint SNe, which produce large amount of C and very low Fe. These key chemical signatures are completely washed out if PISNe pollute the same environments (panel e), because of the large amount of Fe and other heavy elements that these massive stars produce ($\approx 50\%$ of their masses). Panel (a) also shows that, although the overall trend is well reproduced, the model predicts an excess of C-normal stars at [Fe/H] < -4, and it underestimates the observations at [Fe/H] < -6. In other

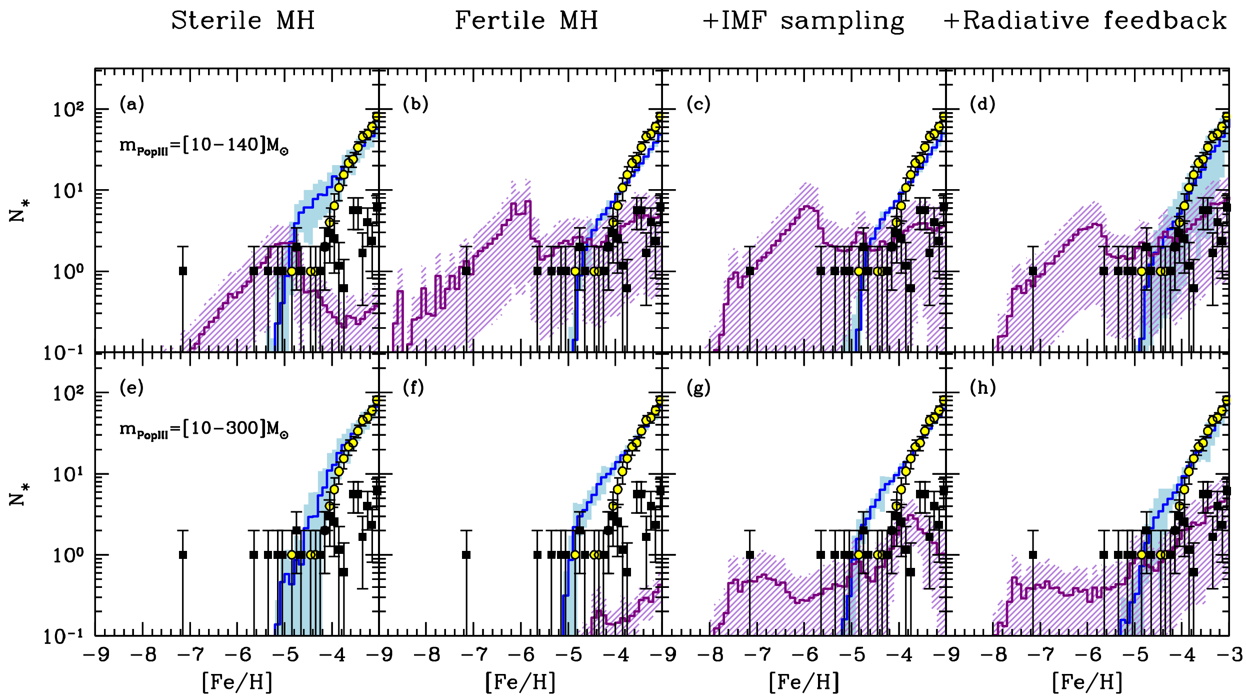

Figure 3.5 *Comparison between observed (points with poissonian errorbars) and simulated (histograms with shaded areas) Galactic halo MDFs, where we differentiate the contribution of C-enhanced (purple histograms with striped-dashed shaded areas and black filled squares) and C-normal (blue histograms with filled shaded areas and yellow filled circles) stars. Pop III stars are assumed to form either in the range [10-140] $M_\odot$ (top panels) or [10-300] $M_\odot$ (bottom panels, see also labels). From left to right we show the results for models with: sterile mini-halos (panels a-e); fertile mini-halos with a temperature-regulated star-formation efficiency (panels b-f); fertile mini-halos with a temperature-regulated star-formation efficiency and a stochastically sampled Pop III IMF (panels c-g); fertile mini-halos with a star-formation efficiency regulated by radiative feedback and a stochastically sampled Pop III IMF (panels d-h).*

words, the slope of the total MDF (blue+purple histograms) is predicted to be roughly constant, at odds with observations (see also Sec. 1.4.1 and 2.6).

The results change when mini-halos are assumed to be "fertile" (panels b, f) and their star formation efficiency is assumed to be simply regulated by their virial temperature (see Sec. 3.1.1). Note that the evolution of the minimum halo mass for star-formation assumed in this case (Salvadori & Ferrara, 2009, 2012) is consistent with the mass threshold for efficient H_2-cooling obtained by adopting the LW background of Ahn et al. (2009), as it has been shown by Salvadori et al. (2014).

Panel (b) shows that the overall MDF has a different shape with respect to panel (a): it rapidly declines around [Fe/H] ≈ -4.5 and shows a low-Fe tail that extends down to [Fe/H] ≈ -8 and that is made by CEMP-no stars *only*. Such a discontinuous shape, which is consistent with observations, reflects the different environment of formation of CEMP-no and C-normal stars (see also the discussion in Salvadori et al. 2016). CEMP-no stars are formed in low-mass mini-halos at a very low and almost constant rate (e.g. Salvadori et al. 2015). C-normal stars, instead, predominantly form in more massive systems, which more efficiently convert gas into stars, producing the rapid rise of the MDF at [Fe/H] > -5.

The comparison between panel (b) and (c) shows that when $m_{\rm PopIII} = [10-140]\,M_{\odot}$ the MDF does not depend on the incomplete sampling of the Pop III IMF (see Sec. 3.1.2). However, the picture changes when $m_{\rm PopIII} = [10-300]\,M_{\odot}$ (panel g). Because of the poor sampling of the Pop III IMF in mini-halos, the formation of stars in the faint SN progenitor mass range is strongly favored with respect to more massive PISN progenitors (Fig. 3.2). As a consequence, the chemical signature of primordial faint SNe is retained in most mini-halos, where CEMP-no stars at [Fe/H] < -4 preferentially form. Furthermore, because of the reduced number of Pop III halos imprinted by primordial faint SN *only*, the amplitude of the low-Fe tail is lower than in panel (c), and thus in better agreement with observations.

Panels (d, h) show the results obtained by self-consistently computing the star-formation efficiency in mini-halos (Sec. 3.1.1). We note that there are no major changes with respect to panels (c, g), meaning that our implementation of the radiative feedback described in Sec. 3.1.3 is consistent with the simple analytical prescriptions used in panels (c, g). In other words, our model results do not depend strongly on the LW flux (upper panel of Fig. 3.4), which in such a biased region of the Universe is expected to be larger than in the average cosmic volume (e.g. Ahn et al., 2009; Xu et al., 2016). Still, three important differences can be noticed by inspecting panels (d, h): (*i*) the number of C-normal stars shows a larger scatter than previously found, (*ii*) their excess with respect to the data is partially reduced, and (*iii*) the number of CEMP-no star with [Fe/H] > -4 is larger, and thus in better agreement with available data. These are consequences of the modulation of mini-halos star-formation efficiency, which declines with cosmic time as a consequence of the decreasing mean gas density and of the increasing radiative feedback effects by the growing LW background (Fig. 3.1). This delays metal-enrichment, preserving the C-rich signatures of faint SNe in the smallest Lyman-α cooling halos, where CEMP-no stars with [Fe/H] > -4 can form with higher efficiency.

We finally note that in all models the scatter of the MDF is much larger for the CEMP component than for the C-normal one. This is due to the broad dispersion among different merger histories at $z > 10$ (see Fig. 2.4), where the CEMP MDF is built (see Fig. 2.10).

When $m_{\rm PopIII} = [10-140]\,M_{\odot}$, furthermore, a bump in the simulated CEMP MDF is observed. This is due to the fact that in this case Pop III stars evolve only as faint SNe, polluting the ISM of their their hosting (mini-)halos around $[{\rm Fe/H}]_{Pop\ III} \approx -6$, a value that is settled by the Fe yields of faint SNe and mean star-formation efficiency of mini-halos (for more massive Ly-α cooling halos $[{\rm Fe/H}]_{PopIII} \sim -5$). Once normal Pop II stars begin to evolve as core-collapse SNe, the Fe enrichment is much faster because of the larger Fe yields. Thus, the ISM is enriched up to higher [Fe/H], giving origin to the bump of CEMP stars.

When we assume $m_{\rm PopIII} = [10-300]\,M_{\odot}$, we obtain a better agreement with the data at [Fe/H]>

-4, i.e. where the statistics of observed stars is higher. However at lower metallicities, $-5 <$ [Fe/H]< -4, we can see that both models over-predict the total number of stars with respect to current data. But how significant is the number of observed stars at these [Fe/H]? In the top panel of Fig. 3.6 we plot the result of our fiducial model for $m_{\rm PopIII} = [10-300]\,M_{\odot}$, also including the *total* MDF and the intrinsic errors induced by observations (grey shaded area). These errors are evaluated by using a Monte Carlo technique that randomly selects from the theoretical MDF a number of stars equal to the observed one (see Sec. 5 of Salvadori et al., 2015). The results, which represent the average value $\pm 1-\sigma$ errors among 1000 Monte Carlo samplings, allow us to quantify the errors induced by the limited statistics of the observed stellar sample. We can see that at [Fe/H]< -4 these errors are larger than the spread induced by different realizations, implying that the statistics should increase before drawing any definitive conclusions (see also Sec. 3.3 for a discussion). We can then have a look to other observables.

3.2.1 CEMP and carbon-normal stars

In the middle panel of Fig. 3.6 we compare our model results with the available measurements of the [C/Fe] ratio for Galactic halo stars at different [Fe/H]. Our findings show a decreasing [C/Fe] value for increasing [Fe/H], in good agreement with observations. According to our results, stars at [Fe/H]< -5 formed in mini-halos polluted by primordial faint SNe (see also Fig. 3.7). When these stars explode, they release large amounts of C and very small of Fe, i.e. $[{\rm C/Fe}]_{\rm ej} > 4$, thus *self-enriching* the ISM up to total metallicities $Z > 10^{-4} Z_{\odot}$. The subsequent stellar generations formed in these mini-halos are thus "normal" Pop II stars. Their associated core-collapse SNe further enrich the ISM with both Fe and C, i.e. $[{\rm C/Fe}]_{\rm ej} \approx 0$, thus producing a gradual decrease of [C/Fe] at increasing [Fe/H]. Such a trend is reflected in the chemical properties of long-lived CEMP-no stars that formed in these environments (see middle panel of Fig. 3.6).

When and where do the most metal-poor C-normal stars form? We find that at $[{\rm Fe/H}] < -4.5$, C-normal stars can only form in halos with a dust-to-gas ratio above the critical value, and that have *accreted their metals and dust from the surrounding MW environment*. When this occurs, normal Pop II SNe in self-enriched halos have already become the major contributors to the metal enrichment of the external MW environment, leading to $[{\rm C/Fe}] < 0.7$ (see also the middle panel of Fig. 2.7). As star-formation proceeds in these Pop II halos, more core-collapse SNe contribute to self-enrichment of these environments, thus further increasing [Fe/H] with an almost constant [C/Fe]. This creates the horizontal branch shown in the middle panel of Fig. 3.6 within [Fe/H]$\approx [-5, -3]$. In this region of the plot, we note that the model predicts a larger concentration of C-normal stars than currently observed.

In the bottom panel of Fig. 3.6 we compare the expected frequency of CEMP-no stars at different [Fe/H] with the available data (see Sec. 1.4.1). We can see that our models over-estimate the contribution of C-normal stars at [Fe/H]< -4. Interestingly, a better agreement is obtained when the mass of Pop III stars is limited to the range $m_{\rm PopIII} = [10-140]\,M_{\odot}$, since more

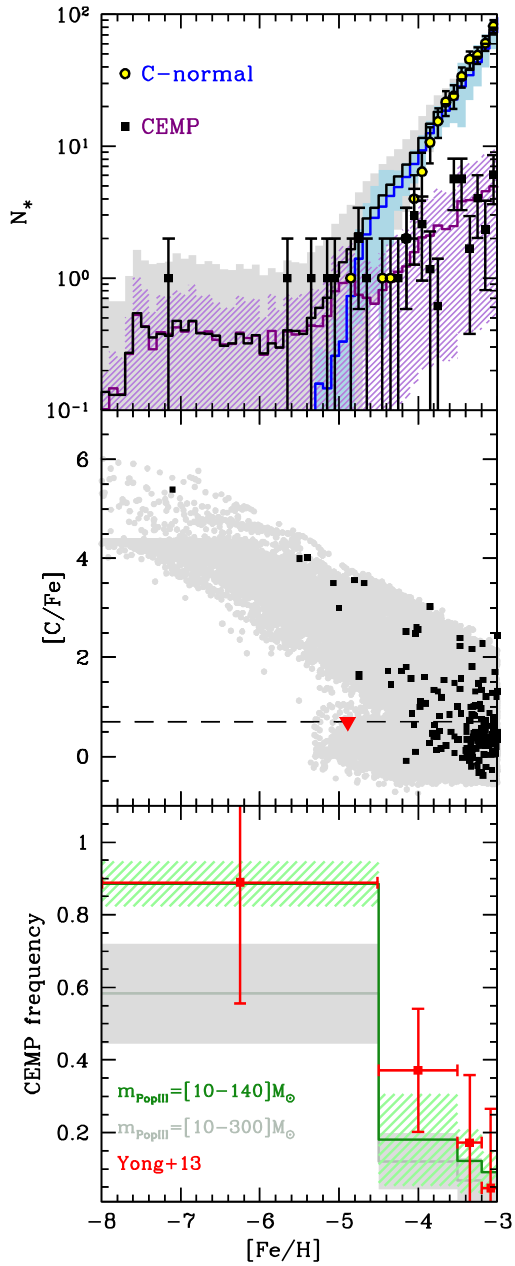

Figure 3.6 *Top: same as panel (h) in Fig. 3.5, but with the inclusion of the total MDF and errors induced by the observations, which have been obtained using a Monte Carlo selection procedure (see text). Middle: stellar [C/Fe] vs [Fe/H] measured in Galactic halo stars (black squares, see Fig. 1 of Salvadori et al. 2015) and obtained in 50 realizations of our fiducial model for $m_{\rm PopIII}$ = [10-300] $M_\odot$ (grey dots). The red triangle at [Fe/H]~-5 shows the upper limit for the only C-normal metal-poor star observed at [Fe/H]≲-4.5 so far (Caffau et al., 2011a). The line shows the value of [C/Fe]=* 0.7*, which discriminates between CEMP-no and C-normal stars. Bottom: comparison between the observed fraction of CEMP-no stars (points with Poissonian errorbars as explained in Sec. 1.4.1) and the fraction predicted by our fiducial models for different Pop III mass ranges; $m_{\rm popIII}$ = [10-140] $M_\odot$ as green histogram with striped-dashed shaded area; $m_{\rm popIII}$ = [10-300] $M_\odot$ as grey histogram with filled shaded area.*

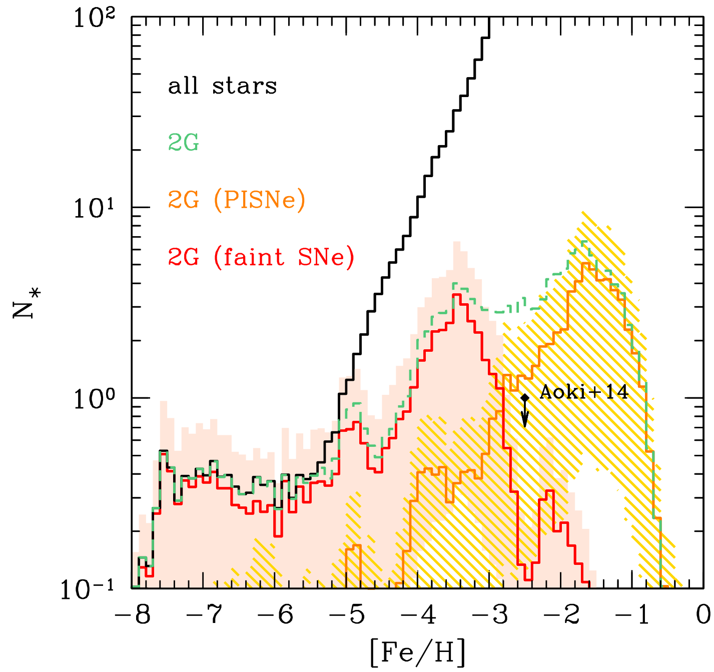

Figure 3.7 *Simulated average MDF for all stars (black histogram) and for 2G stars (dashed green histogram), selecting them as stars formed in environments where metals come mostly (> 50%) from Pop III stars. The red (orange) histogram represents 2G stars with a dominant (> 50%) metal contribution from Pop III faint SNe (PISNe) and the filled (striped-dashed) shaded region represents the 1-σ dispersion. The upper limit at [Fe/H] = -2.5 represents the recent observation of a star with chemical imprint of PISNe Aoki et al. (2014).*

faint SNe are produced. The number of stars observed at [Fe/H]< -4 is limited to $\approx$ 10 (see Sec. 1.4.1). Furthermore, such a discrepancy between model and data might also be connected to some underlying physical processes that cannot be captured by the model, as we will extensively discuss in Sec. 3.3. In conclusion, Pop III stars with masses $m_{\rm PopIII}$ = [10 − 300] $M_{\odot}$ are favored by our analysis. Such a model better matches the overall shape of the MDF of CEMP-no and C-normal stars, and it is also in better agreement with data at [Fe/H]> -4 (compare panels d and h of Fig. 3.5). Only at these high [Fe/H] the intrinsic observational errors are lower than the dispersion induced by different merger histories (see top panel of Fig. 3.6), making the difference between model and data statistically significant.

3.2.2 Predictions for second-generation stars

Our analysis of the Galactic halo MDF and properties of CEMP-no vs C-normal stars supports the most recent findings of numerical simulations for the formation of the first stars, which indicate that Pop III stars likely had masses in the range $m_{\rm PopIII}$ = [10 − 300] $M_{\odot}$. We make one step further, and we quantify the expected number and typical [Fe/H] values of second-

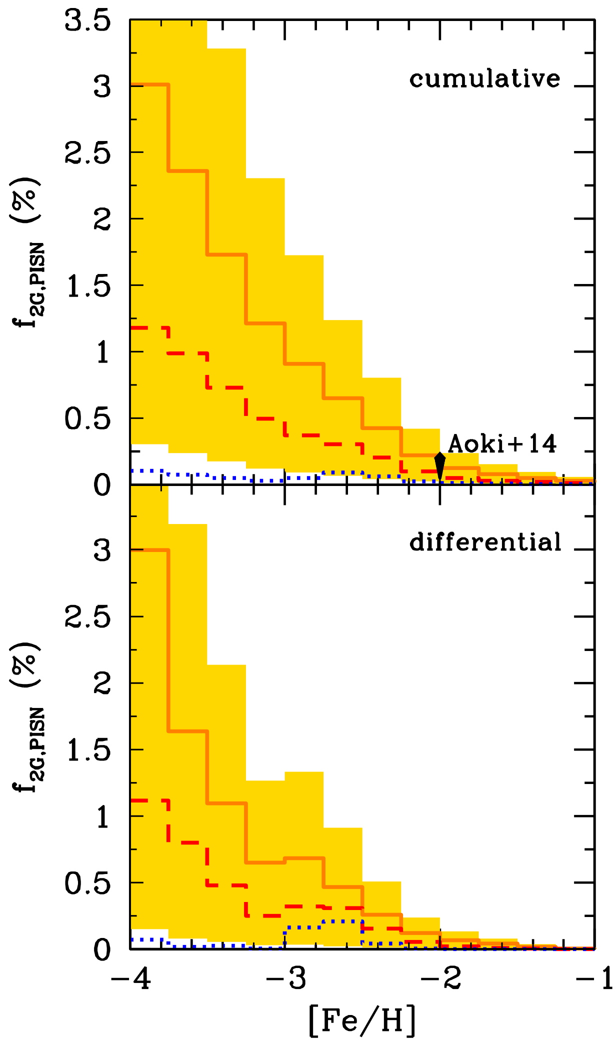

Figure 3.8 *Cumulative (top) and differential (bottom) fraction (%) of 2G stars imprinted by PISNe with respect to the total number of stars in different [Fe/H] bins. The colors show the percentage of 2G stars formed in environments where metals from PISNe correspond to at least 50% (solid orange), 80% (dashed red) and 99% (dotted blue) of the total. The yellow shaded area is the 1-σ dispersion for the 50% case. The data point is from Aoki et al. (2014), who possibly detected the chemical imprint of PISNe (upper limit) in 1 out of 500 stars at [Fe/H]< -2.*

generation (2G) stars, i.e. stars that formed in gaseous environments that were predominantly polluted by Pop III stars (Salvadori et al., 2007).

In Fig. 3.7 we show the predictions for our fiducial model with $m_{\rm PopIII} = [10 - 300]\, M_\odot$. The figure illustrates the total distribution of 2G stars formed in environments in which Pop III stars provided $\geq$ 50% of the total amount of metals (green). Furthermore, it shows the individual distributions for 2G stars imprinted by faint SNe (red) and PISNe (orange). It is clear that the total number of 2G stars represents an extremely small fraction of the Galactic halo population, in full agreement with previous studies (Salvadori et al., 2007; Karlsson et al., 2008). Furthermore, we can see that the distributions of 2G stars polluted by faint SNe and PISNe are extremely different. Because of the low amount of Fe released by faint SNe, 2G stars enriched by this stellar population predominantly appear at [Fe/H]< -3. Interestingly, we find that their distribution essentially matches that of CEMP-no stars (see Fig. 3.6), representing $\approx 100\%$ of the observed stellar population at [Fe/H]< -5. In other words, *our model predicts that all CEMP-no stars in this [Fe/H] range have been partially imprinted by Pop III faint SNe*. On the contrary, we see that the distribution of 2G stars polluted by PISNe is shifted towards higher [Fe/H] values. This is because massive PISNe produce larger amount of iron than faint SNe, thus self-enriching their birth environments up to [Fe/H]> -4. In fact, for $m_{\rm PopIII} = [10-300]\,M_\odot$, the Fe yielded by PISN per total stellar mass formed, M_*, is $Y_{Fe}^{\rm PISN} \approx M_{Fe}/M_* \approx 2.7\times10^{-2}$, which is several orders of magnitude larger than the one produced by faint SNe. As described in Sec. 3.1.2 a mini-halo can likely host a PISN if it forms a stellar mass $M_* \gtrsim 10^4 M_\odot$ which implies a Fe production of $M_{Fe} \gtrsim 270 M_\odot$. According to our prescription for star-formation, the typical mass of such a mini-halo is $\sim 10^8 M_\odot$, meaning that this amount of Fe can be dispersed in a gaseous environment of $\sim 10^7 M_\odot$, assuming the cosmological baryon fraction. This leads to an ISM polluted at [Fe/H]~-1.8, which is consistent with the peak of 2G stars with PISN imprint predicted by our model (see Fig. 3.7). Unfortunately, at these [Fe/H] the Galactic halo population is dominated by stars formed in environments mostly polluted by normal Pop II SNe (see Sec. 3.2.1). This makes the detection of 2G stars imprinted by PISNe very challenging.

In the upper (lower) panel of Fig. 3.8 we quantify the cumulative (differential) fraction of 2G stars imprinted by PISNe with respect to the overall stellar population as a function of [Fe/H]. In both panels we identify 2G stars that formed in environments where 50%, 80%, and 99% of the metals were coming from PISNe. We can clearly see that 2G stars always represent $< 3\%$ of the total stellar population. Furthermore, the cumulative fraction of 2G stars polluted by PISN at 50% (80%) level, strongly decreases with increasing [Fe/H]: around [Fe/H]$= -2$, in particular, these 2G stars are predicted to represent 0.25% (0.1%) of the total stellar population, which is fully consistent with current observations (see point in Fig. 3.8). Indeed, among the ≈ 500 Galactic halo stars analyzed so far at [Fe/H]< -2, there is only one candidate at [Fe/H]≈ -2.4 that might have been imprinted by a PISN (Aoki et al., 2014). This rare Galactic halo star shows several peculiar chemical elements in its photo-sphere, which might reflect an ISM of formation enriched by both massive PISNe and normal core-collapse SNe (Aoki et al., 2014). In Fig. 3.8 we can see that 2G stars imprinted by the chemical products of PISNe *only*, represent $< 0.1\%$ of the total Galactic halo population (top), and they are predicted to be more frequent at $-3 <$[Fe/H]< -2 (bottom).

3.2.3 Varying the Pop III IMF

We can finally analyze the dependence of our findings on the slope and mass range of the Pop III IMF. These results are shown in Fig. 3.9, where we compare our reference model (left), with

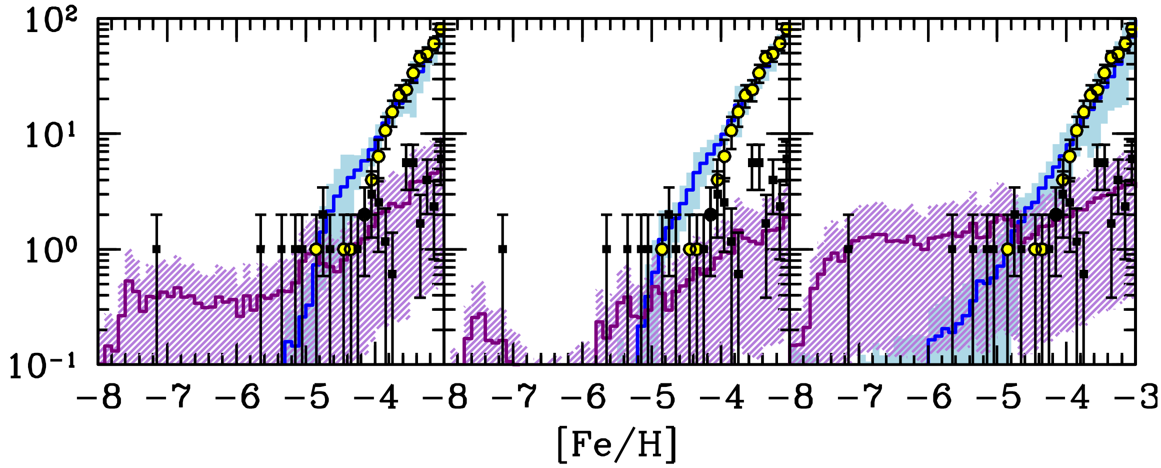

Figure 3.9 *Comparison between the observed and simulated Galactic halo MDFs (see Fig. 3.5) obtained by using different IMF for Pop III stars: a Larson IMF with $m_{\rm PopIII}$=[10-300]$M_\odot$ and m_{ch} = $20M_\odot$ (left), a Flat IMF with $m_{\rm PopIII}$=[10-300)]$M_\odot$ (middle), and a Larson IMF with $m_{\rm PopIII}$=[0.1-300]$M_\odot$ and m_{ch} = $0.35M_\odot$ (right).*

two alternative choices of the Pop III IMF, inspired by numerical simulations: a flat IMF with $m_{\rm PopIII} = [10-300]\,M_\odot$ (e.g. Hirano et al., 2014), and a Larson IMF with $m_{\rm PopIII} = [0.1-300]\,M_\odot$ and a characteristic mass $m_{ch} = 0.35\,M_\odot$ (e.g. Stacy et al., 2016).

The low-Fe tail of the MDF, and thus the number and distribution of CEMP-no stars, strongly depends on the Pop III IMF. When a flat IMF is considered (middle panel of Fig. 3.9), less CEMP-no stars are produced with respect to the reference case (left panel), both at low and at high [Fe/H]. This is due to the smaller fraction of faint SNe with respect to the total mass of Pop III stars formed. This is equal to $\approx$ 1.5% for a flat IMF, and $\approx$ 70% for a Larson IMF, where these numbers have been obtained by integrating the normalized IMFs in the mass range $[8-40]\,M_\odot$. Such a large difference is partially mitigated by the incomplete sampling of the Pop III IMF in inefficient star-forming mini-halos (see Sec. 3.1.2). Still, the different IMF slope decreases substantially the number of CEMP-no stars, making the flat IMF model *partially inconsistent* with current data-sets.

On the other hand, when the Pop III IMF is extended down to lower masses, $m_{\rm PopIII} = [0.1-300]\,M_\odot$, the number of CEMP stars increases with respect to the reference model (right vs left panels of Fig. 3.9). However, if we make the same calculation as before, we find faint SNe to represent $\approx$ 1% of the total Pop III stellar mass, substantially less than in our reference model. The larger number of CEMP stars at low [Fe/H] must then have a different origin.

At [Fe/H] < -5, we predict that $\approx 35\%$ [4] of second-generation CEMP stars ($\approx 15\%$ of the total number of stars) have been imprinted by a mixed population of Pop III stars, including AGB stars with $m_{\rm PopIII} = [2 - 10]\, M_{\odot}$. In particular we find that these Pop III AGB stars might provide from ≈ 10 to ≈ 30 % of the total amount of heavy elements polluting the birth environment of these 2G stars. These CEMP stars, therefore, might also retain the peculiar chemical signature of Pop III AGB stars, such as the slow-neutron capture elements (e.g. Goriely & Siess, 2001, 2004). In other words $\approx 35\%$ of these [Fe/H]< -5 stars might be CEMP-s stars rather than CEMP-no stars. This seems to be in contrast with current observational findings (e.g. Norris et al., 2010; Bonifacio et al., 2015) although more work needs to be done to rule out this Pop III IMF model. On the one hand detailed theoretical calculations are required to understand if Pop III AGB stars produce s-process elements at observable levels. On the other hand, a larger stellar sample at [Fe/H] < -5 is mandatory to robustly constrain the low-mass end of the Pop III IMF.

Furthermore the model predicts the existence of metal-free stars, as long as stars with $Z < 10^{-5}\, Z_{\odot}$, that should respectively correspond to $\approx 0.15\%$ and $\approx 0.3\%$ of the total number of stars at [Fe/H]< -3. As already discussed and quantified by several authors (Tumlinson, 2006; Salvadori et al., 2007; Hartwig et al., 2015), this result might be in contrast with the current *non-detection* of metal-free stars. Yet, given the total number of stars collected at [Fe/H]< -3, which is ≈ 200, the fraction of zero-metallicity stars should be $< 1/200 = 0.5\%$, which is still consistent with our findings.

3.3 Summary and discussion

In this Chapter, we investigate the role that Pop III star-forming mini-halos play in shaping the properties of the MDF of Galactic halo stars and the relative fraction of CEMP-no and C-normal stars observed at [Fe/H]< -3. To this end, we use the merger tree code GAMETE (Salvadori et al., 2007, 2008), which we further implement with respect to studies for Galactic halo stars presented in Ch. 2 to resolve H_2-cooling mini-halos with $T_{vir} < 10^4$ K, which are predicted to host the first, Pop III stars (e.g. Abel et al., 2002; Hirano et al., 2014). We initially assumed Pop III stars to have masses in the range $[10 - 300]\, M_{\odot}$, and to be distributed according to a Larson IMF (Fig. 3.2). We subsequently explored the dependence of our results on different IMF slope and Pop III mass range. In all cases, we assumed that Pop III stars with masses $m_{\rm PopIII} = [10 - 40]\, M_{\odot}$ evolved as faint SNe that experience mixing and fallback (e.g. Bonifacio et al., 2003; Umeda & Nomoto, 2003; Iwamoto et al., 2005; Marassi et al., 2014, 2015).

To accurately model the formation of Pop III stars, we introduce a new random IMF selection procedure, which allows us to account for the incomplete sampling of the Pop III IMF in inefficiently star-forming mini-halos (Sec. 3.1.2). To compute the star-formation efficiency of these low-mass systems, we exploit the results of numerical simulations by Valiante et al.

[4] This is an average value for $-8 <$[Fe/H]< -5. Within this [Fe/H] range the percentages can vary from ≈ 20 to ≈ 60 %.

(2016), who evaluate the cooling properties of H_2-cooling mini-halos as a function of: (*i*) virial temperature, (*ii*) formation redshift, (*iii*) metallicity, and (*iv*) LW background (Sec. 3.1.1). To this end, we self-consistently compute the LW and ionizing photon fluxes produced by MW progenitors, along with the reionization history of the MW environment (Sec. 3.1.3), which is consistent with recent theoretical findings (Salvadori et al., 2014) and new observational data (Planck Collaboration et al., 2015, 2016).

The main results of this work, and their implications for theoretical and observational studies, can be summarized as follows:

- the shape of the low-Fe tail of the Galactic halo MDF is correctly reproduced only by accounting for star-formation in mini-halos, which confirms their key role in the early phases of galaxy formation.
- We demonstrate that it is fundamental to account for the poor sampling of the Pop III IMF in mini-halos, where inefficient Pop III starbursts, with $< 10^{-3}\,M_\odot\,\mathrm{yr}^{-1}$, naturally limit the formation of $> 100\,M_\odot$ stars and hence change the "effective" Pop III IMF.
- CEMP-no stars observed at [Fe/H]< -3 are found to be imprinted by the chemical products of primordial faint SNe, which provide $> 50\%$ of the heavy elements polluting their birth environment, making them "second-generation" stars
- Second-generation stars imprinted by PISNe, instead, emerge at $-4 <$ [Fe/H]< -1, where they only represent a few % of the total halo population, which makes their detection very challenging.
- At [Fe/H]≈ -2, only 0.25% (0.1%) of Galactic halo stars are expected to be imprinted by PISNe at $> 50\%$ ($> 80\%$) level, in good agreement with current observations.
- The low-Fe tail of the Galactic halo MDF and the properties of CEMP-no stars strongly depends on the IMF shape and mass range of Pop III stars.

A direct implication of our study is that the Galactic halo MDF is a key observational tool not only to constrain metal-enrichment models of MW-like galaxies and the properties of the first stars (Tumlinson, 2006; Salvadori et al., 2007), but also the star-formation efficiency of mini-halos. These observations, therefore, can be used to complement data-constrained studies of ultra-faint dwarf galaxies aimed at understanding the properties of the first star-forming systems (e.g. Salvadori & Ferrara, 2009; Bovill & Ricotti, 2009; Bland-Hawthorn et al., 2015; Salvadori et al., 2015).

A key prediction of our model concerns the properties and frequency of second-generation (2G) stars formed in gaseous environments imprinted by $> 50\%$ of heavy elements from PISNe. In agreement with previous studies (Salvadori et al., 2007; Karlsson et al., 2008), we find that these 2G stars are extremely rare, and we show that their MDF peaks around [Fe/H]$= -1.5$ (Fig. 3.7).

In particular, 2G stars imprinted by PISNe *only* ($>99\%$ level) are predicted to be more frequent at $-3 <$[Fe/H]< -2, where they represent $\approx 0.1\%$ of the total. In the same [Fe/H] range, 2G stars polluted by PISNe at $> 50\%$ ($> 80\%$) level, constitute $\approx 0.4\%$ ($\approx 0.2\%$) of the stellar population. These numbers are consistent with the unique detection of a rare halo star at [Fe/H]≈ -2.5 that has been possibly imprinted *also* by the chemical products of PISNe (Aoki et al., 2014).

On the other hand, we show that *C-enhanced stars at [Fe/H] < -5 are all truly second generation stars*. Hence, the number and properties of these CEMP stars can provide key indications on the Pop III IMF.

Given the current statistics, we show that a flat Pop III IMF with $m_{\rm PopIII} = [10-300]\,M_\odot$ is disfavored by the observations. Furthermore, by assuming a Larson IMF with $m_{\rm PopIII} = [0.1-300]\,M_\odot$ and $m_{ch} = 0.35\,M_\odot$, we find that on average $\approx 35\%$ of 2G CEMP stars at [Fe/H]< -5 are imprinted *also* by the chemical products of zero metallicity AGB stars. Such Pop III AGB stars can provide up to 30% of the metals polluting the ISM of formation of these CEMP stars, which therefore might show the typical enhancement in s-process elements. This provides a prediction for the existence of Pop III stars with $m_{\rm PopIII} < 10 M_\odot$, that can be tested by increasing the statistics of CEMP stars with available s-process measurements at [Fe/H]< -5 (e.g. Bonifacio et al., 2015).

As a final point, we recall that, with our fiducial model, we find a larger number of C-normal stars with $-5 <$[Fe/H]< -4 than observed. As a consequence, in this [Fe/H] range the fraction of CEMP-to-C-normal stars is also lower than observed, although consistent with the data at $1-\sigma$ level (Fig. 3.6). Several solutions for this small discrepancy do exist:
(*i*) the global contribution of Pop III stars to metal-enrichment might have been underestimated in the model, which do not account for the *inhomogeneous mixing of metals* into the MW environment. Including this physical effect would natural delay the disappearance of Pop III stars (Salvadori et al., 2014);
(*ii*) a fraction of Pop II stars with $m_{\rm popII} = [10-40]\,M_\odot$ may evolve as faint SNe rather than normal core-collapse SNe, thus further contributing to enrich the gaseous environments with C, and reducing the formation of C-normal stars (de Bennassuti et al., 2014);
(*iii*) another solution concerns *chemical feedback*. If we exclude the Caffau's star, the low-Fe tail of C-normal stars is consistent with $Z_{cr} \approx 10^{-4.5}\,Z_\odot$, which means that these low-mass relics form *thanks to dust* but in environments that might correspond to higher $\mathcal{D}_{cr}$ (or lower $f_{\rm dep}$) than we assumed here, where $Z_{cr} = \mathcal{D}_{cr}/f_{\rm dep}$ and $\mathcal{D}_{cr}$ can be expressed as (Schneider et al., 2012b):

$$\mathcal{D}_{cr} = [2.6-6.3]\times 10^{-9}\left[\frac{T}{10^3\mathrm{K}}\right]^{-1/2}\left[\frac{n_{\rm H}}{10^{12}\mathrm{cm}^{-3}}\right]^{-1/2}. \tag{3.10}$$

Here we have assumed the total grain cross section per unit mass of dust to vary in the range $2.22 \leq S/10^5\mathrm{cm}^2/\mathrm{gr} \leq 5.37$, and a gas density and temperature where dust cooling starts to be effective equal to $n_{\rm H} = 10^{12}\,\mathrm{cm}^{-3}$ and $T = 10^3$ K . Since S could vary in a broader interval depending on the properties of the SN progenitor, this might lead to a larger variation of the value of $\mathcal{D}_{cr}$;
(*iv*) since C-normal stars at $-5 \leq$ [Fe/H] ≤ -4 predominantly form in MW progenitors which

have $\mathcal{D} \geq \mathcal{D}_{cr}$ and have accreted their heavy elements from the MW environment (as opposed to halos that have been self-enriched by previous stellar generations), we might have overestimated the $\mathcal{D}$ of *accreted material*. In fact, no destruction is assumed to take place in SN-driven outflows, when the grains are mixed in the external medium, or during the phase of accretion onto newly formed halos. Indeed, the null detection of C-normal stars with [Fe/H] < -4.5, beside the Caffau's star and despite extensive searches, might be an indication that, at any given Z, halos accreting their heavy elements from the MW environment might be less dusty than self-enriched halos;
(*v*) a final possibility pertains the effect of *inhomogeneous radiative feedback*, which might reduce (enhance) the formation of C-normal (C-enhanced) stars in mini-halos locally exposed to a strong (low) LW/ionizing radiation. These effects are expected to be particularly important at high-z, i.e. before the formation of a global uniform background (see the next Chapter).
Although all these solutions are plausible, we should not forget that our comparison is actually based on 10 stars at [Fe/H]< -4, which makes the intrinsic observational errors larger than those induced by different merger histories of the MW (Fig. 3.6, upper panel). This underlines the quest for more data to better understand the intricate network of physical processes driving early galaxy formation.

In order to account for point (*v*) a different approach must be followed since semi-analytical models coupled with EPS-generated merger trees cannot account for the spatial information. However, we can couple them with N-body simulations of a MW-analogues (e.g. Salvadori et al. 2010). If radiative transfer can also be included, then the propagation of photons from the MW progenitors can be followed, allowing to estimate the inhomogeneous pattern of ionized gas and its effect on the star-formation. This is what we will present in the following Chapter.

4

Galaxy formation with radiative and chemical feedback

In this Chapter we study the effect of inhomogeneous radiative feedback processes on the star forming properties of the MW progenitors. In order to do this, we introduce GAMESH, a new pipeline integrating the latest release of cosmological radiative transfer (RT) code CRASH (Graziani et al., 2013) with the semi-analytic model of galaxy formation GAMETE, powered by a N-body simulation (Salvadori et al., 2010b, hereafter SF10). By following the star formation, metal enrichment and photo-ionization in a self consistent way, GAMESH is an ideal tool to study the effects of photo-ionization and heating in galaxy formation simulations. Into the bargain, the radiative transfer model adopted by GAMESH relies on a Monte Carlo scheme and not only naturally accounts for the inhomogeneities of the ionization process, but also allows a deep investigation of other radiative transfer effects, a self consistent calculation of the gas temperature, and a more accurate description of the stellar populations responsible for the MW environment reionization.

For this part of the work the GAMESH pipeline will be applied to the Galaxy formation simulation introduced in Scannapieco et al. (2006) and successfully post-processed by the semi-analytic code GAMETE (SF10), to derive the properties of the central galaxy and to compare them with the available observations of the MW system. It should be pointed out that the version of GAMETE used in this Chapter is much simpler with respect to that described in Sec. 2.2, in order to allow a better comparison with the results in SF10 Although the mass resolution of the adopted N-body does not provide a sufficient statistics of mini-halos to study the missing satellite problem, the robust set of results already obtained with the previous semi-analytic approach offers an excellent validation framework for the GAMESH pipeline and allows to appreciate the many advantages of the accurate radiative transfer treatment of CRASH coupled with the semi-analytic approach of GAMETE. In the next Chapter we will focus on high resolution simulations.

The Chapter is organized as follows. In Sec. 4.1 we describe the GAMESH pipeline by briefly introducing its components and by providing details on the feedback implementation. The MW reionization simulation is introduced in Sec. 4.2 and the results discussed in Sec. 4.3. Sec. 4.4 finally summarizes the conclusions of this part of the work.

4.1 The GAMESH pipeline

Here we describe the work-flow of the GAMESH pipeline which integrates a N-body simulation, the semi-analytic code GAMETE (see Sec. 4.1.1 for more details), and the radiative transfer code CRASH (see Sec. 4.1.2); more details on each pipeline module can be found in dedicated subsections.

GAMESH models the galaxy formation process concatenating a series of snapshots provided by a N-body run at given redshifts $z_{i=0,...,N}$: the pipeline uses the physical quantities calculated at z_i as initial conditions for the successive calculation at z_{i+1}. Along the redshift evolution, the feedback between star formation and RT is handled by two software modules called interactors I_0 (detailed in Sec. 4.1.3) and I_1 (see Sec. 4.1.4). I_0 transforms the galaxy star formation rate (SFR) predicted by GAMETE into a list of ionizing sources for CRASH, while I_1 uses the gas ionization and temperature determined by the RT to establish a star formation prescription for the semi-analytic model implemented in GAMETE. Hereafter we focus on the pipeline logic at fixed z_i (see Fig. 4.1); for an easier reading we also generically refer to the ionization of the gas as $x_{\rm gas}$, while a more specific notation will be adopted in Sec. 4.3 to discuss the ionization fractions of hydrogen and helium.

The initial conditions of the pipeline (ICs) are provided by the N-body simulation which assigns the simulation redshift z_i to all the components, sets up the N-body merger-tree into I_1 and the gas number density $n_{\rm gas}$ in the grid used by CRASH to map the physical domain.

Once the ICs are set up, I_1 starts the simulation by creating a list of galaxies found in the merger-tree: each galaxy is identified by a unique ID and it associates the values of $x_{\rm gal}$ and $T_{\rm gal}$ found in the cell of the grid containing the galaxy center of mass (see Sec. 4.1.4 for more details). This list is then processed by GAMETE to establish which galaxy can form stars, self-consistently with the metallicity, temperature and ionization of the accreting gas.

As output of GAMETE we obtain a sub-sample of star forming galaxies, their SFR, stellar metallicity (Z_*) and population type. I_0 converts this sample into a list of CRASH sources by evaluating the galaxy positions on the grid, their spectrum integrated ionization rate $\dot{N}_\gamma$ and the spectral shape S_ν. A stellar synthesis database has been implemented in I_0 (see Sec. 4.1.3) to derive $\dot{N}_\gamma$ and S_ν from the stellar metallicity and the SFR.

Once the properties of the radiating galaxies are established, the radiative transfer simulation starts propagating photons for a simulation duration corresponding to the Hubble time separating two snapshots, and it obtains the gas ionization $x_{\rm gas}$ and temperature $T_{\rm gas}$ at redshift z_i. These quantities are finally used for the subsequent redshift z_{i+1}, by repeating the same algorithm.

Before moving to a more detailed description of the GAMESH components, we want to emphasize the advantages of our approach. We point out that the use of CRASH allows us to follow with accuracy the process of reionization of the MW progenitors along the redshift evolution, by taking into account the intrinsic inhomogeneities due to the gas clumps and by calculating the temperature history self-consistently. Moreover, radiative transfer effects, which

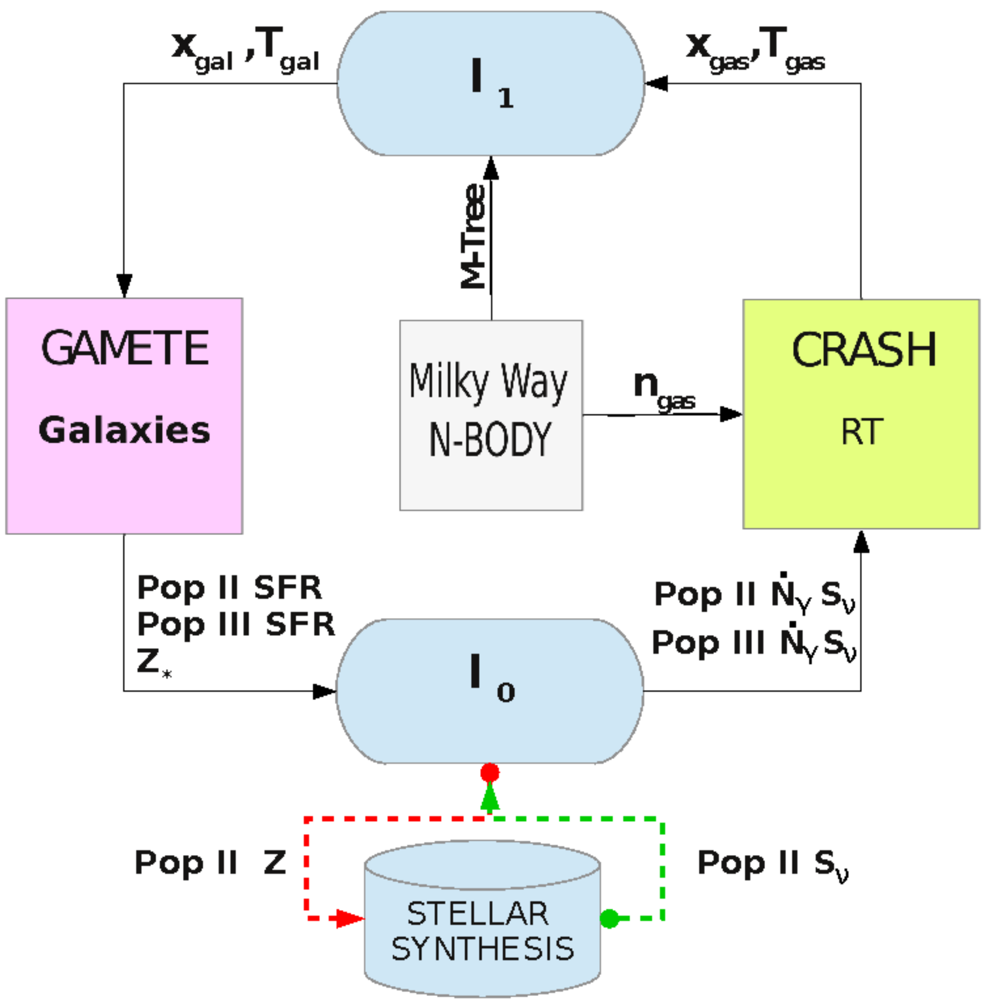

Figure 4.1 GAMESH *pipeline logic at fixed redshift z_i. The quantities $x_{\rm gal}$, $T_{\rm gal}$, $x_{\rm gas}$ and $T_{\rm gas}$ refer to the ionization fractions and temperatures of the gas in the grid cells containing galaxies and in the simulated domain, respectively. The gas number density projected into the grid used by* CRASH *is indicated as $n_{\rm gas}$ and the global set of information provided by the N-body merger tree as M-Tree. The quantities used by interactor I_0 are the star formation rates (SFRs) and the metallicity of the stars (Z_*), while the computed ionization rates and spectral shapes per galaxy and population are indicated as $\dot{N}_\gamma$ and S_ν. See text for more details.*

generally lead to spectral hardening that may preferentially heat gas in over-dense regions, will be accounted for by the RT simulation without pre-assuming any propagation model.

The adoption of GAMETE allows us to fully explore the interplay between reionization, radiative feedback and chemical evolution which can have very interesting and testable consequences (Schneider et al. 2008). Using this approach, we can break the degeneracy between having gradual suppression and constant star formation efficiency or sharp suppression and mass-dependent star formation efficiency.

In the following sections more details on the pipeline components are provided.

4.1.1 GAMETE

As already pointed out in Ch. 2, GAMETE (Salvadori et al., 2007) is a data-constrained semi-analytic model for the formation of the MW and its dwarf satellites (Salvadori & Ferrara, 2009), whose algorithm has been designed to study the properties of the first stars and the early chemical enrichment of the Galaxy. Since for this part of the work a simplified version of GAMETE has been used, here we briefly summarize the hypotheses assumed to trace the evolution of gas and stars inside each galactic halo (identified as a group of DM particles) of the merger-tree hierarchy:

- at the highest redshift of the merger tree, the gas has a primordial composition;
- in each galaxy the star-formation rate is proportional to the mass of cold gas;
- the contribution of radiative feedback is accounted for by adopting different prescriptions, depending on the problem at hand. When the code runs in stand-alone mode (i.e. not in pipeline) GAMETE assumes instant reionization (IReion, SF10), i.e. stars form only in galaxies of mass $M_h > M_4(z) = 3 \times 10^8 M_\odot (1+z)^{-3/2}$ ($M_h > M_{30}(z) = 2.89 \times M_4(z)$) prior to (after) reionization (assumed complete at $z = 6$). When GAMETE runs coupled with CRASH, star formation is not regulated by the halo mass but by exact radiative feedback effects as predicted by the RT simulation and detailed in Sec. 4.1.4. In this case the star formation efficiency in mini-halos (i.e. halos with $T_{vir} < 2 \times 10^4$K) is decreased $\propto T_{vir}^{-3}$ as already detailed in Salvadori & Ferrara (2012), to mimic the effects of a LW background;
- according to the critical metallicity scenario (Schneider et al., 2002, 2006) already discussed in Sec. 1.2, low-mass stars form according to a standard, Salpeter-like IMF when the gas metallicity $Z \geq Z_{cr} = 10^{-4} Z_\odot$; otherwise, for $Z < Z_{cr}$ we assume that massive Pop III stars form with a mass $m_{\rm PopIII} = 200 M_\odot$;
- the enrichment of gas within the galaxies and in the diffused MW environment (i.e. the IGM) is calculated by including a simple description of supernova (SN) feedback (Salvadori et al., 2008). Metals and gas are assumed to be instantaneously and homogeneously mixed by adopting the Instantaneous Recycling Approximation (IRA, Tinsley, 1980); a discussion on the implications of this choice can be found in Salvadori et al. (2007, 2010b).

The interplay between the N-body scheme and semi-analytic calculation, along the redshift evolution of the simulation, is detailed below. At each time-step the mass of gas, metals and stars within each halo is equally distributed among all its DM particles, and used in the next integration step as ICs. The same technique is applied to metals ejected into the IGM so that the chemical composition of newly virializing halos depends on the enrichment level of the environment out of which they form. To recover the spatial distribution of the long-living metal-poor stars at $z = 0$, we also store their properties per DM particle.

4.1.2 CRASH

CRASH (Ciardi et al., 2001; Maselli et al., 2003; Maselli & Ferrara, 2005; Maselli et al., 2009; Graziani et al., 2013) is a Monte Carlo based scheme implementing 3D ray tracing of ionizing radiation through a gas composed by H and He and metals in atomic form (e.g. C, O, Si). The code propagates ionizing packets with N_γ photons per frequency along rays crossing an arbitrary gas distribution mapped onto a Cartesian grid of N_c^3 cells. At each cell crossing, CRASH evaluates the optical depth τ along the casted path and the amount of absorbed photons $N_{abs} = N_\gamma(1 - e^\tau)$. N_{abs} is used to calculate the ionization fractions of the species $x_{\rm gas} = x_{\rm i} \in (x_{\rm HII}, x_{\rm HeII}, x_{\rm HeIII})$ and the gas temperature $T_{\rm gas}$ of the crossed cell.

A CRASH simulation is defined by assigning the initial conditions on a regular three-dimensional Cartesian grid and a physical box linear size of L_b, specifying:

- the number density of H ($n_{\rm H}$) and He ($n_{\rm He}$), the gas temperature $T_{\rm gas}$ and the ionization fractions $x_{\rm i}$ at the initial time t_0[1];
- the number of ionizing point sources (N_s), their position in Cartesian coordinates, ionization rate ($\dot{N}_\gamma$ in photons s^{-1}) and spectral energy distribution (SED, S_ν in erg s^{-1} Hz^{-1}) assigned as an array whose elements provide the relative intensity of the radiation as frequency bins;
- the simulation duration t_f and a given set of intermediate times $t_j \in \left\{t_0, \ldots, t_f\right\}$ to store the values of the relevant physical quantities;
- the intensity and spectral energy distribution of a background radiation, if present.

More technical information about the latest implementation of CRASH and references on its variants can be found in Graziani et al. (2013).

[1] $n_{\rm gas}$ is calculated by projecting the particle distribution of the simulation on a Cartesian grid of N_c^3 cells and by deriving the gas component via the universal baryon fraction.

4.1.3 Radiation sources

As explained above, CRASH requires the list of all the ionizing sources present in the box grid. This is provided in the GAMESH framework by the GAMETE-to-CRASH module I_0, responsible of converting the properties of the star forming galaxies (Pop II/Pop III SFR, Z_*) into CRASH sources with specific spectral properties.

I_0 first maps the center of mass of each galaxy onto grid coordinates and then converts the star formation rates into spectrum-integrated quantities $\dot{N}_\gamma$ depending on the stellar population.

For Pop II stars we calculate ionization rates and spectral shapes accordingly to Bruzual & Charlot (1993) and we assume a IMF in the mass range $[0.1 - 100]M_\odot$. A different spectral shape and ionization rate is then associated with each of the Pop II star forming galaxy depending on its population lifetimes t_* and stellar metallicity Z_*. The spectrum and ionization rate is derived from a grid of pre-computed spectra integrated in specific lifetime bins $t_* \in \{0.001, 0.01, 0.1, 0.4, 1.0, 4.0, 13.0\}$ Gyr and stellar metallicity $Z_* \in \{0.005, 0.2, 0.4, 1.0, 2.5\}Z_\odot$.

For Pop III stars we assume an ionization rate per solar mass, $\dot{N}_\gamma = 1.312\times10^{48}$ [photons $s^{-1}/M_\odot$] (Schaerer, 2002) corresponding to a stellar mass $M_* \sim 200M_\odot$, averaged on a lifetime of about 2.2 Myr. The SED of Pop III stars is simply assumed as black body spectrum at temperature $T_{BB} = 10^5$ K.

4.1.4 Radiative feedback

The radiative feedback on the star formation is implemented by the pipeline module I_1. This module is responsible for setting up the ionization and temperature ($x_{\rm gal}$, $T_{\rm gal}$) of the gas in the galaxies, successively processed by GAMETE to establish their star formation.

At the first redshift z_0 it is simply assumed that the medium is fully neutral (i.e. $x_{\rm gal} = 0$) and $T_{\rm gal} = T_0(1 + z_0)$, where T_0 is the value of the CMB temperature at $z = 0$. During the redshift iterations I_1 computes $x_{\rm gal}$ and $T_{\rm gal}$ by first finding the cell containing the galaxy center of mass in the CRASH grid. As second step, it evaluates which of the surrounding cells best describe the environment from which the galaxy can get the gas to fuel star formation.

The effective environment scale from which cold gas is fueled into star forming galaxies is crucial to calculate the values of $x_{\rm gal}$, $T_{\rm gal}$ and to apply the radiative feedback. As in our pipeline the gas distribution surrounding halos relies on the spatial resolution of the RT (i.e. the cell size in CRASH: $\Delta L = L_b/N_c$), we compare the virial radius R_{vir} of the galactic halo with $\Delta L/2$. We simply assume that if $2R_{vir}/\Delta L \leq 0.1$, the galactic environment is mainly set up in the cell containing its center of mass and we assign $x_{\rm gal} = x_{\rm cell}$, $T_{\rm gal} = T_{\rm cell}$. When, on the other hand, $2R_{vir}/\Delta L > 0.1$ the gas reservoir of the galaxy could extend to the surrounding cells and then $T_{\rm gal}$ is assigned to their volume averaged value; the value of $x_{\rm gal}$ remains instead the one taken from the central cell. It should be noted though, that the threshold value 0.1 depends on the resolution of the CRASH grid and must be tuned for increased resolutions grids, when necessary [2].

Once the temperature and ionization fractions affecting the galactic star formation have been assigned, we first use $x_{\rm gal}$ to evaluate the mean molecular weight μ of the gas and then to calculate the virial temperature of the galactic halo T_{vir} (see Eq. 1.12).

Star formation in the galaxy is finally admitted in GAMETE if the condition $T_{\rm gal} < T_{vir}$ applies, allowing accretion of cold gas in the galaxy to form stars.

4.2 Milky Way Reionization simulation

Here we describe the set-up of our MW reionization simulation. After a brief description of the N-body simulation and its parameters we detail the radiative transfer assumptions and the initial conditions.

Following Scannapieco et al. (2006), we adopt a ΛCDM cosmological model with $h = 0.71$, $\Omega_0 h^2 = 0.135$, $\Omega_\Lambda = 1 - \Omega_0$, $\Omega_b h^2 = 0.0224$, $n_s = 1$ and $\sigma_8 = 0.9$.

4.2.1 The N-body simulation

To study the MW reionization we adopt the snapshots and merger tree from a cosmological N-body simulation of the MW-sized galaxy halo carried with GCD+ (Kawata & Gibson, 2003a), which were used in Scannapieco et al. (2006). The specific details of the simulation are described in Scannapieco et al. (2006); here we briefly summarize the simulation parameters necessary to understand the global GAMESH run.

The mass adopted for the N-body particles is $M_p = 7.8 \times 10^5 M_\odot$ and the softening length used is 540 pc. The simulated system consists of about 10^6 particles within the virial radius $R_{vir} = 239$ kpc for a total virial mass $M_{vir} = 7.7 \times 10^{11} M_\odot$. Note that the virial mass and virial radius estimated by observations for the MW are $M_{vir} = 10^{12} M_\odot$ and $R_{vir} = 258$ kpc respectively (Battaglia et al., 2005).

Using a multi-resolution technique (Kawata & Gibson, 2003b), the initial conditions at $z = 56$ are set up to resolve the region in a sphere within the radius of $R = 4R_{vir}$ with the high-resolution N-body particles of mass $M_p = 7.8 \times 10^5 M_\odot$ and with the softening length of 540 pc; the other region is resolved instead with lower resolution particles.

[2] Improving the accuracy of the galactic environment description would ideally require to selectively resolve the halo structures (i.e. a cell size $\Delta L << R_{vir}$), as obtained by using cell refinements around the galaxies. The adopted spatial resolution is documented in Sec. 4.2.2

The simulation snapshots are provided with regular intervals every 22 Myr between $z = 8$ and 17 and every 110 Myr for $z < 8$. The virialized DM halos are then identified by friend-of-friend group finder by assuming a linking parameter $b = 0.15$ and a threshold number of particles of 50; the resulting minimum mass halo is $M = 3.75 \times 10^7 M_\odot$.

A validating N-body simulation at lower resolution, also including a star formation recipe, has also been performed to confirm that the assumed initial condition lead to a disc formation (see Brook et al. 2007).

4.2.2 The RT set-up

The radiative transfer simulation is performed at each redshift z_i, on a box size of $2h^{-1}$ Mpc comoving, by emitting $N_p = 10^6$ photon packets from each star-forming galaxy[3]. The box is mapped on a Cartesian grid of $N_c = 128$ cells per cube side, providing a cell resolution of $\Delta L \sim 15.6h^{-1}$ kpc. The gas in the box is assumed of cosmological composition (92% H and 8% He) and we neglect the metal ions and the effects of the metal cooling around the star-forming halos. For a gas of cosmological composition (i.e. $n_{\rm HI} \sim 92\%\ n_{\rm gas}$) the ionizing spectrum is usually assigned in the energy range 13.6 eV $\leq E \leq$ 140 eV. Note that the spectral database could be extended at any time to include harder spectra accounting for sources emitting higher energy photons. Note also that the CRASH calculation adopts the same cosmological parameters as in the N-body simulation to maintain consistency across the pipeline life-cycle.

The convergence of the Monte Carlo sampling is guaranteed by an identical run with a factor of ten larger N_p and providing the same numbers within the fourth decimal of the volume average ionization and temperature created in the box.

The simulation starts at $z_0 \sim 16$[4] with uniform temperature $T_0 \sim 46$ K and we assume that the reionization is completed when the volume-averaged ionization fraction of the hydrogen reaches the value $x_{\rm HII} \geq 0.995$ against the gas recombination. Due to the large excursion in Hubble time, a gas recombination CASE-B is adopted in the simulation and the diffuse re-emission is neglected.

In the absence of a model for the UV background (UVB) on the scale of the MW formation, we avoid using an external cosmological UV background as done in other works presented in the literature, and prefer to mimic a flux entering our box by applying periodic boundary conditions to the escaping radiation. While this choice guarantees that the photon mean free path is conserved when the box ionization is advanced and the gas becomes transparent to the

[3] Note that according to the pipeline algorithm each source could have a 'a priori' different spectrum assigned by I_0 as function of its lifetime and stellar metallicity.

[4] This is the first redshift in which the applied FoF is able to identify the first halos. This redshift value depends on the mass resolution of the simulation.

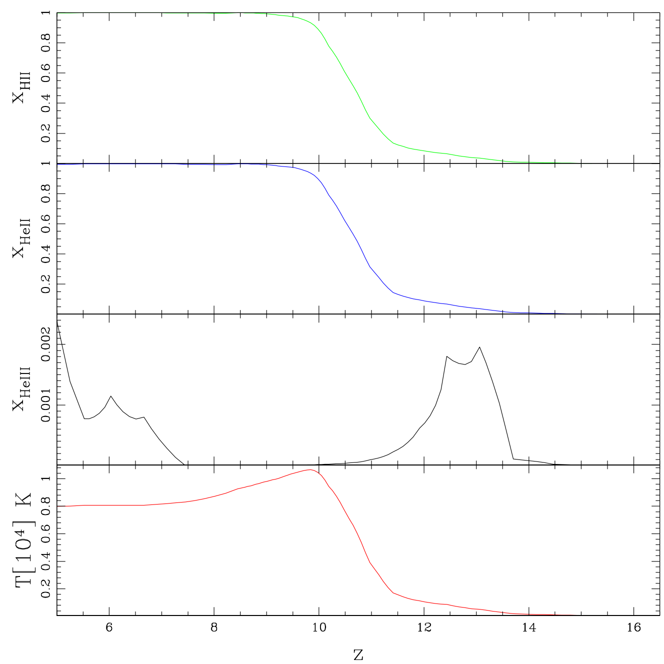

Figure 4.2 *Redshift evolution of the volume averaged ionization fractions and temperature of the gas, down to $z \sim 5$. From top to bottom the values of $x_{\mathrm{HII}}, x_{\mathrm{HeII}}, x_{\mathrm{HeIII}}, T$ are shown in solid green, blue, black and red lines respectively.*

hydrogen-ionizing radiation, it should be noted that we do not account for an external ionizing flux likely emitted by the background of QSO sources established below $z \sim 4$.

4.3 Results

In this section we discuss the results of our simulation, also comparing them with trends obtained adopting the assumption of instant reionization at $z \sim 6$ as discussed in SF10. Hereafter, for an easier reading, we omit the label "*gas*" in the variable names referring to ionization fractions and temperature of the gas and we comment on the single ionized species $x_{\mathrm{i}} \in (x_{\mathrm{HII}}, x_{\mathrm{HeII}}, x_{\mathrm{HeIII}})$.

4.3.1 Reionization and temperature histories

Here we investigate the evolution in redshift of the volume averaged ionization fractions and temperature (i.e. $x_i(z), T(z)$ in this section) resulting from the radiative transfer simulation.

In Fig. 4.2 we show the redshift evolution of x_{HII} (top panel) and $x_{\mathrm{HeII}}, x_{\mathrm{HeIII}}$ (second and third panels from top) down to $z = 5$[5]. $x_{\rm HII}$ remains below $x_{\rm HII} \sim 0.1$ when $z > 12$, afterwards it rapidly rises up to $x_{\rm HII} \sim 0.5$ at $z \sim 11$ and reaches $x_{\rm HII} \sim 0.9$ when $z \sim 10$. The sudden increase in the hydrogen ionization fraction in the redshift range $10 < z \leq 12$ can be ascribed both to the rising in the comoving SFR (Fig. 4.4) and in the total number of emitting galaxies (Fig. 4.5) but more likely to an advanced stage of overlapping of ionized regions, which makes the reionization process intrinsically non-linear.

Below $z \sim 10$ the hydrogen reionization wades through and $x_{\rm HII}$ increases up to 0.99 by $z \sim 9$ and up to 0.999 by $z \sim 5$. Even if not visible in the Figure, we point out that below $z \sim 8.5$ the value of the third decimal of $x_{\rm HII}$ continues to oscillate in $0.997 \leq x_{\rm HII} \leq 0.999$ due to the continuous unbalance in the gas ionization, created by the ongoing gas collapse that enhances the recombination rate at the center, and by the in-homogeneous reionization/recombination occurring in the volume. We consider the hydrogen reionization completed at $z \sim 6.4$ when $x_{\rm HII} > 0.995$, neglecting these fluctuations.

The second and third panels from top, show the ionization histories of helium. It is immediately evident that the He II reionization can be sustained only by the Pop II stars dominating below $z \sim 12$ while the reionization of He III never occurs at the considered MW scale (here $2h^{-1}$ Mpc comoving) without the contribution of an external background of harder spectra (e.g. QSO). In fact, while the redshift trend of $x_{\rm HeII}$ follows the one of the hydrogen, $x_{\rm HeIII}$ never reaches values higher than $x_{\rm HeIII} = 0.002$ along the entire redshift range. As also pointed out for $x_{\rm HII}$, the volume averaged ionization fraction of He II continues to oscillate in $0.97 < x_{\rm HeII} < 0.99$ below $z \sim 8.5$, confirming that a harder spectral component is required to sustain full helium ionization against gas recombination. Note that a bump in the value of $x_{\rm HeIII}$ (third panel from top) occurs in the redshift range $12 < z < 15$, tracing the presence of Pop III stars (see also Fig. 4.4) with their harder spectral shapes. Note also that the volume averaged value of $x_{\rm HeIII}$ remains always negligible over the entire simulation: after the transition from Pop III to Pop II stars the presence of full ionized helium is so closely confined to the sources that is not visible in the panel, except at z < 7, when hydrogen ionization is complete and harder photons ($E > 54.4$ eV) are free to cross the box many times and to create a very small ionization fraction of fully ionized helium.

The redshift evolution of the volume-average temperature is shown in the bottom panel of Fig. 4.2 in 10^4 K units. Before $z \sim 10$, the temperature rises from the initial value $T \sim 50$ K up to $T \sim 10^4$ K; note that the rapid evolution of Pop III stars in this redshift range is so small (not visible in the plot) that it cannot change the global trend of the average temperature. In the redshift interval $9 < z < 10$ the gas stabilizes at a average photo-ionization equilibrium temperature of $T \sim 10^4$ K, before its average value starts decreasing by some 10^3 K during the successive evolution. Oscillations of the order of 10^3 K are present below $z \sim 5$ (not shown in the plot), due to the competitive effects of gas clumping toward the center, adiabatic cooling due to the cosmological expansion, and finally in-homogeneous distribution and properties of the ionizing galaxies. Even if not visible in this plot we report a final average temperature of $T = 7.9 \times 10^3$ K at $z = 0$ but we

[5]Below this redshift a uniform ionized pattern of hydrogen is created and the values are less indicative. Note that we cannot discuss the helium reionization due to the absence of a harder radiation background.

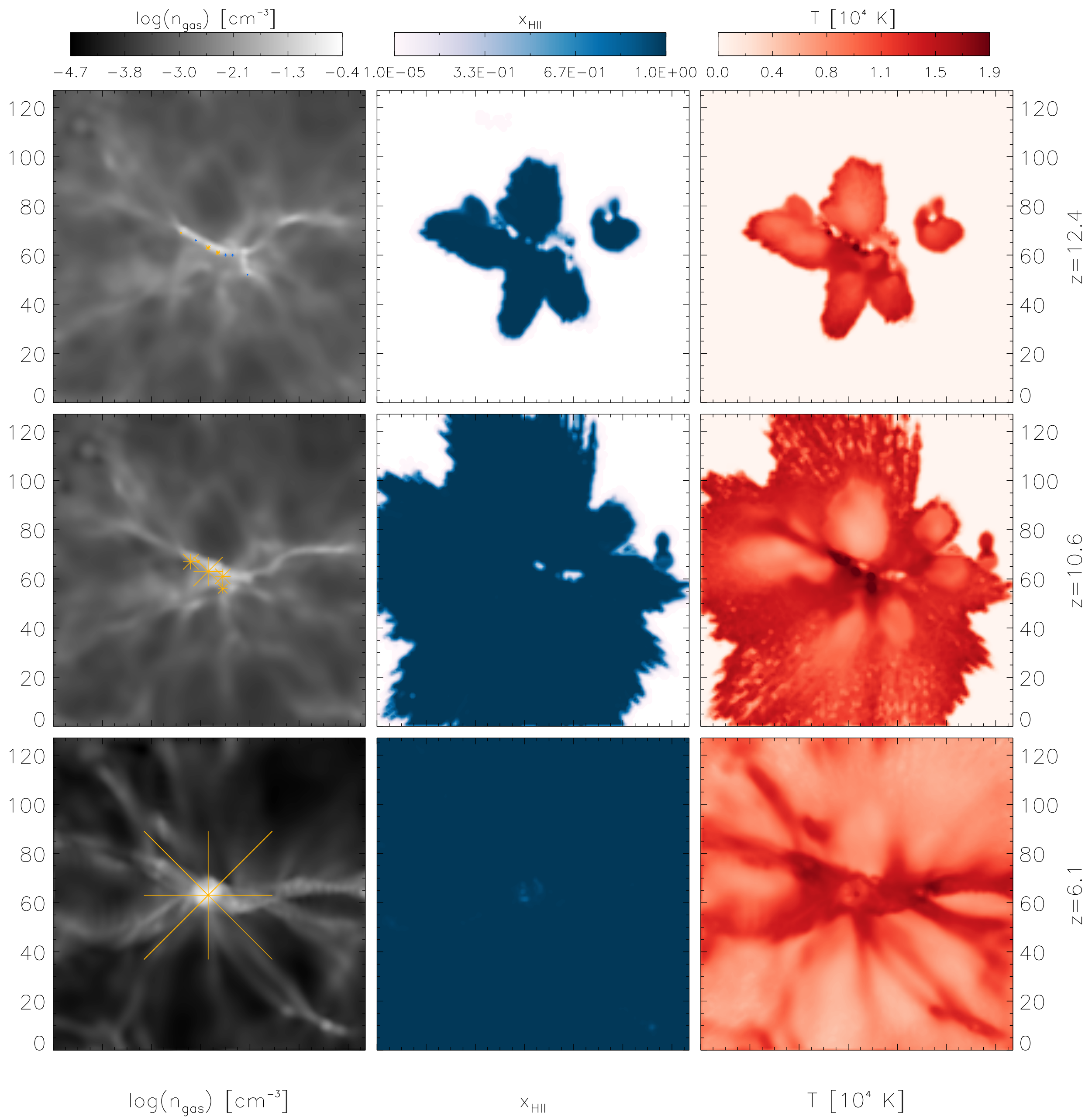

Figure 4.3 *Slice cuts of n_{gas} (first column), $x_{\rm HII}$ (second column), T (third column) at three different redshifts: $z \sim 12$ (top panels), $z \sim 11$ (middle panels), $z \sim 6$ (bottom panels). The value of the fields in the plane are represented as color palettes and the distance units are expressed in number of grid cells along the x and y axis ($\sim 15.6h^{-1}$ kpc per cell). In the first-column panels star forming galaxies are symbolized as blue crosses when forming Pop III stars, while as gold-yellow asterisks for Pop II stars; the sizes of the symbols are scaled with the galaxy ionization rate $\dot{N}_\gamma$.*

remind that this value is certainly underestimated in our simulation due to the absence of high energy photons from the QSO background established on the large scale below $z \sim 4$.

To visually illustrate how the reionization process evolves in space and redshift, we show in Fig. 4.3 three slice cuts of our volume (of $2h^{-1}$ comoving Mpc side length) taken at redshifts $z \sim 12, 11, 6$ (see panels from top to bottom). Panels in the first column show $log(n_{gas}(z))$ as gray gradient from black ($n_{gas} \sim 2 \times 10^{-5}$ cm^{-3}) to white ($n_{gas} \sim 0.4$ cm^{-3}); in the second column $x_{\rm HII}(z)$ is shown by a color palette from white ($x_{\rm HII} < 10^{-5}$) to dark-blue ($x_{\rm HII} = 1.0$), and finally the pattern of $T(z)$ is drawn in the third column with a different color palette from light-red ($T \sim 50$ K) to dark-red ($T \sim 1.9 \times 10^4$ K). In all the panels, the distances are shown in cell units ($\sim 15.6h^{-1}$ kpc per cell) along the x and y directions.

Superposed to the number density maps we also show the star forming galaxies (SFG) present in the surface of choice: galaxies forming Pop III stars are symbolized as blue crosses (top panel), while gold-yellow asterisks are associated with the presence of Pop II stars. Also note that the size of each symbol is scaled with its $\dot{N}_\gamma$ and the position of star forming galaxies perfectly correlates with the gas filaments, falling toward the center where the central galaxy is progressively forming along the redshift evolution.

As consequence of the central position of the ionizing sources, the reionization proceeds inside-out. At high redshift (top panels), the low density regions surrounding the center of the box (black regions, first column) are easily ionized by the sources (blue pattern, second column). At the center of the image note that high-density clumps (white regions) are able to suppress photo-ionization with a high gas recombination rate (light-blue patterns). The average gas temperature (third column) tends to stabilize around $T \sim 1.4 \times 10^4$ K in the regions involved by the overlap of ionized bubbles (light- and dark-red), mainly driven by the contribution of Pop III stars. T rapidly decreases down to $T \sim 10^2$ K at the border of the ionized region (light-red patterns) not reached by stellar radiation. Consistently with the ionized pattern, few high-density structures remain self-shielded and settle at very low temperature at the center image. Note that the presence of helium in our simulation significantly changes the gas photo-heating enhancing the contrasts between over-dense regions and voids. At $z \sim 11$ (middle panels) the reionization process is already quite advanced and the ionizing radiation involves a large fraction of the box, including the under-dense regions far away from the center (light-blue patters). Voids are rapidly ionized and their temperature stabilizes around $T \sim 6 \times 10^3$ K, well below the central value $T \sim 10^4$ K. Finally, at $z \sim 6$ the entire volume reaches photo-ionization equilibrium and its average temperature stabilizes around $T \sim 8.0 \times 10^3$ K but the spatial pattern continues to show large variations from the gas filaments (branching off the central MW-type galaxy) and from the under-dense regions.

Note that at the final redshift ($z \sim 6.1$) the central galaxy is seen as single source with highest ionization rate of about $\dot{N}_\gamma = 2 \times 10^{54}$ photons/s and SFR $\sim 13 M_\odot$/yr (the total SFR of the emitting objects is $\sim 20 M_\odot$/yr). In the other galaxies laying on the plane, the star formation is suppressed by radiative feedback (see Sec. 4.3.2.1 for more details)

As final comment, we point out that our simulation lacks the ionizing contribution of an

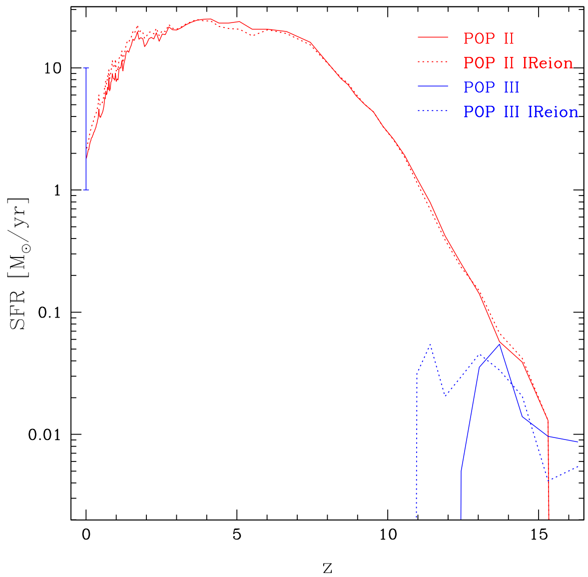

Figure 4.4 *Star formation rate for Pop II (solid red lines) and Pop III (solid blue) as function of z. As reference the values obtained with the instant reionization approximation (IReion) are shown dotted lines and same colors for the two populations. The value of the SFR estimated by observation at $z = 0$ is reported as error bar. See text for more details.*

external UV background, especially at the helium ionizing frequencies. While periodic boundary conditions are adopted to preserve the photon mean free path at all frequencies, the external UVB may play a relevant role because of the small size of the simulation box and its coarse mass resolution. On the other hand, the inclusion of a UVB is neither trivial nor straightforward. First, the available UVB models (see for example Haardt & Madau 2012 and references therein) are computed and calibrated on the large scale structure. Therefore, on the scales of MW formation, both the intensity and the spectral shape of the UVB may be modified by RT effects. Here we only point out that an external UVB could only impact hydrogen ionization above $z \sim 11$. In fact, Fig. 4.2 shows that below this redshift the internal flux is sufficient to sustain hydrogen ionization.

4.3.2 Feedback on star formation

The redshift evolution of the comoving SFR is shown in Fig. 4.4, where the red lines refer to the contribution from Pop II stars (highest curve) and the blue lines to Pop III. Dotted lines, with same colors, show the values obtained by adopting the instantaneous reionization prescription (see Sec. 4.1.1). In the redshift interval $12.4 < z \lesssim 16$ the total SFR of our simulation (solid lines) increases up to $1.7 M_{\odot}$/yr thanks to both Pop III and Pop II stars, but note that at the highest redshift $z \sim 16.5$ (when the gas is mostly primordial) only Pop III objects contribute to the total SFR. Feedback from Pop III forming galaxies, both radiative and chemical, acts efficiently

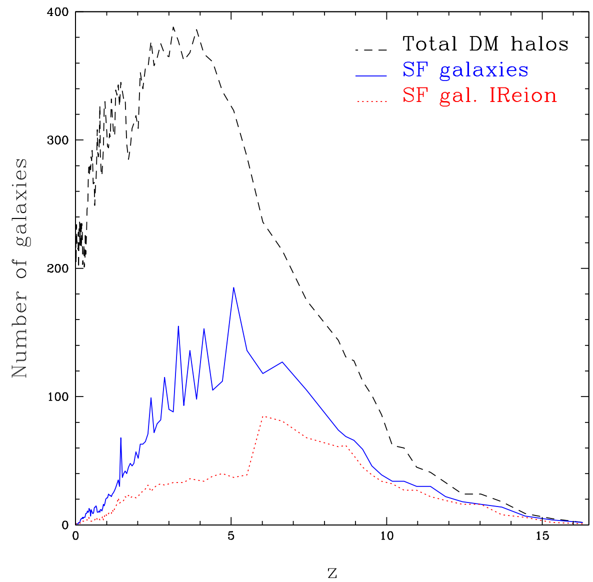

Figure 4.5 *Number of star forming galaxies as function of z in the simulation (solid blue line). The dotted red line refers to the IReion case, while the dashed black line shows, as reference, the total number of DM halos found in the N-body simulation.*

on the surrounding medium: their hard spectra locally increase the IGM temperature inhibiting star formation in unpolluted clouds, while mechanical feedback rapidly pollutes the IGM up to the critical metallicity $Z_{cr} = 10^{-4} Z_{\odot}$. Both effects contribute to their sudden disappearance, triggering the formation of Pop II stars below $z \sim 12.4$. At lower redshift Pop II stars cause an increase of the total SFR up to a value of SFR $\sim 25 M_{\odot}$/yr at the peak redshift $z \sim 4$. The successive evolution proceeds with an irregular but progressive decrease down to a value of SFR $\sim 1.8 M_{\odot}$/yr at $z = 0$, in good agreement with the observed data (Chomiuk & Povich, 2011).

It is interesting to compare these results with the ones obtained with the IReion approximation for both populations. We remind that in IReion approximation GAMETE accounts for feedback by assuming that only Lyman-α halos having $M > M_4$ can form stars at $z > 6$, while at $z \sim 6$ the volume is suddenly ionized and a different threshold applies. For $z < 6$ only halos with circular velocity greater than 30 km s^{-1} (i.e. $M > M_{30}$) can trigger the star-formation (see SF10).

By comparing the solid and dotted lines in Fig. 4.4 we immediately conclude that the suppression of star formation operated by the IReion is quite appropriated to reproduce the SFR of Pop II stars in a wide redshift range but it over-estimates the SFR at $z = 0$ by 15%. Note also that the stronger radiative feedback effects at high redshift in Ireion lower the SFR of Pop III stars and delay the transition between the two stellar populations.

4.3.2.1 Feedback statistics

The effects of the radiative feedback on the statistics of star forming galaxies are shown in Fig. 4.5 as function of redshift z. The solid blue line indicates the number of SFG computed in our simulation, while the dotted red line refers to the IReion case. The total number of DM halos found in the N-body simulation in use is shown as dashed black line.

By comparing solid and dotted lines, we first note that at the current resolution of the simulation, which does not resolve the full range of masses that sample the mini-halos regime, the condition $M > M_4$ could appear quite appropriate to reproduce the statistics of the galaxies with suppressed star formation at very high redshifts ($z > 10$). On the other hand, a careful comparison with Fig. 4.4 immediately shows a different star formation rates of Pop III galaxies (compare blue lines in Fig. 4.4).

This discrepancy can be ascribed to a combination of reasons which involve radiative, mechanical, and chemical feedback. Also note that the IReion model cannot account for in-homogeneous feedback on high-redshift low mass objects (which are likely to host Pop III stars) but indiscriminately applies to *all* the galaxies with $M > M_4$ present in the volume. At high redshift this assumption is particularly incorrect because the SFG are still quite separated in space and then their radiative feedback acts very selectively, only affecting their surrounding neighbourhoods. See for example how dis-homogeneous is the bubble overlap in the third panels of Fig. 4.3 and how many regions of the simulated volume remain unaffected by photo-heating.

Note that the current mass resolution of the N-body simulation does not allow to draw robust conclusions on the radiative feedback effects at high-redshift.

At lower redshifts the efficiency of the radiative feedback increases with the progress of reionization in both models. In the redshift interval $6 < z \lesssim 9$ the GAMESH run predicts that around 50% of the galaxies have been affected by radiative feedback and this value increases up to 65% by $z \sim 4$, with a jagged trend due to both oscillations in the number of potential galaxies (dashed black line) and the in-homogeneous heating in space induced by the RT[6]. Below $z = 4$ the suppression of star formation in small galaxies progresses rapidly allowing few remaining objects in the box to form stars, as observed in the MW environment.

Note the difference in the statistics of SFG below $z \sim 6$ obtained in the IReion approximation. In fact a realistic radiative feedback operates with a more gradual suppression in time, due to the in-homogeneous nature of the bubble overlap in space. In $3 < z < 6$ this difference induces an error in the number of SFG as high as 40% between the two cases (compare solid blue line with dotted red line). On the other hand this statistical discrepancy between models is not reflected in both the total SFR (Fig. 4.4) and the IGM enrichment (see Fig. 4.8) which are very similar in this redshift range, also indicating that the high-mass galaxies surviving the IReion prescription

[6]As commented in the previous paragraph, only with a higher mass and spatial resolution simulation we can fully understand the impact of an in-homogeneous reionization process on the statistics of SF galaxies

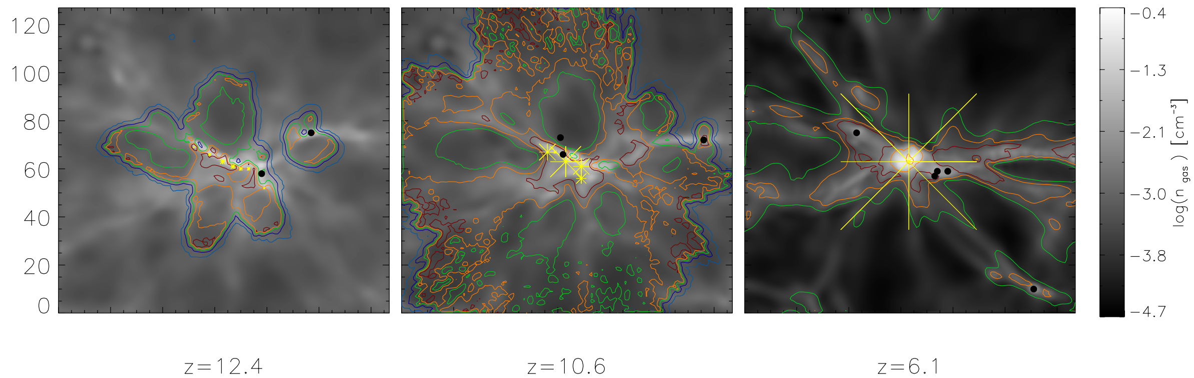

Figure 4.6 *Slice cuts of the gas number density n_{gas} with superposed temperature contour-plots: $T \sim 100$ K (cyan), $T \sim 4 \times 10^3$ K (blue), $T \sim 10^4$ K (green), $T \sim 1.3 \times 10^4$ K (orange) and $T \sim 1.5 \times 10^4$ K in dark-red. All the star forming halos in the plane are represented by yellow asterisks, while black dots indicate halos in the plane in which star formation is suppressed by radiative feedback.*

provide a dominant contribution to these quantities.

Fig. 4.6 visually shows how the in-homogeneous radiative feedback operates in space, by comparing the same slice cuts and redshift sequence commented in Fig. 4.3. Here, on top of the gas number density field we have traced few solid line iso-contours of the gas temperature: $T \sim 100$ K in cyan, $T \sim 4 \times 10^3$ K in blue, $T \sim 10^4$ K in green, $T \sim 1.3 \times 10^4$ K as orange and finally $T \sim 1.5 \times 10^4$ K in dark-red. All the star forming galaxies are symbolized by yellow asterisks, while the galaxies in which star formation has been suppressed by radiative feedback are shown as black filled circles.

By comparing the three panels it is immediately evident how the inhomogeneities in the reionization process induce large differences in randomly suppressing star formation (left and middle panel) before a UVB is fully established (right panel). At high redshifts few suppressed SFGs (black circles) are trapped in regions with $T \sim 10^4$ K, not necessarily connected with the emitting galaxies. Note for example the galaxy on the right side of the middle panel: even far from the center it is surrounded by gas with high temperature, that likely originates from more complicated three-dimensional effects created by the RT. On the other hand at $z \approx 6$ (right panel) the medium is already pervaded by a quasi-homogeneous UVB and then all the galaxies below a critical mass are easily suppressed in the entire domain. To study if a critical mass for the suppression of SFGs is statistically restored against the non-linearity induced by the RT, we should rely on a higher resolution simulation providing a better statistics for both Lyman-α and H_2-cooling halos, as well as better spatial resolution. With this study we will able to provide a numerically motivated recipe for semi-analytic models. Here we limit the discussion to this figure, as an illustrative example of how radiative feedback implemented in GAMESH works.

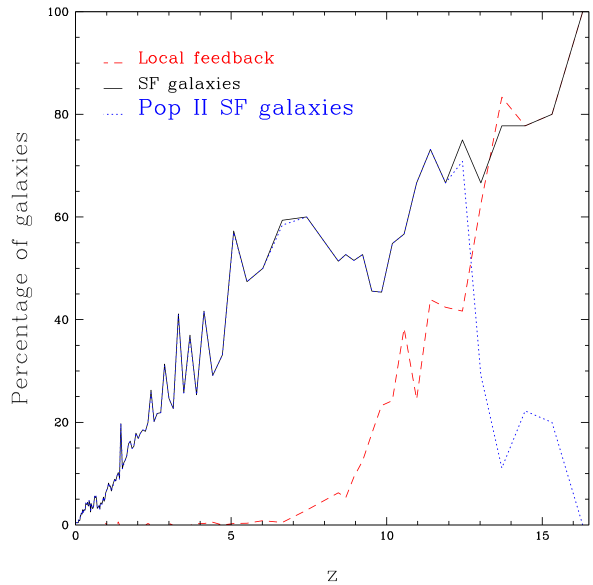

Figure 4.7 *Percentage of star forming galaxies as function of z (solid black line) and percentage of galaxies affected by radiative feedback in their own cell (dashed red line). The blue dotted line shows the percentage of galaxies forming mainly Pop II stars.*

4.3.2.2 Local versus environmental feedback

As introduced in Sec. 4.1.4, the radiative feedback defined in GAMESH depends on the spatial extension of the galactic environment feeding cold gas for star formation. Depending on the virial radius of the dark matter halo hosting each galaxy and the spatial resolution of the RT grid, the feedback could act *locally* to the sources (i.e. accounting just for the temperature in the galaxy cell ($2R_{vir} \leq 0.1\Delta L$)) or it could act *globally* involving larger scales (i.e. cells surrounding the one containing the galaxy) when $2R_{vir} > 0.1\Delta L$.

The statistics of these two mechanisms can help to understand the importance of 'local' versus 'global' feedback along the progress of reionization, establishing a H-ionizing uniform UVB. In Fig. 4.7 we show the percentage of SFG (solid black line) together with the percentage of galaxies that are influenced by 'local' feedback (dashed red line) [7]. To understand which stellar population is affected by local or environmental effects we also show in blue dotted line the percentage of galaxies forming Pop II stars.

As already commented in the previous figure, the percentage of SFG (solid black line) rapidly decreases from high to low redshifts following the progress of reionization with a spiky and irregular trend down to $z \sim 4$. The presence of a "plateau" in the redshift interval $6 < z < 9$ could mark the existence of an extended reionization epoch in which the gas is kept in photo-ionization equilibrium in the entire box at $T \sim 10^4$ K and the hydrogen ionization fraction increases from

[7] These number are calculated with respect to the total number of halos found in the simulation.

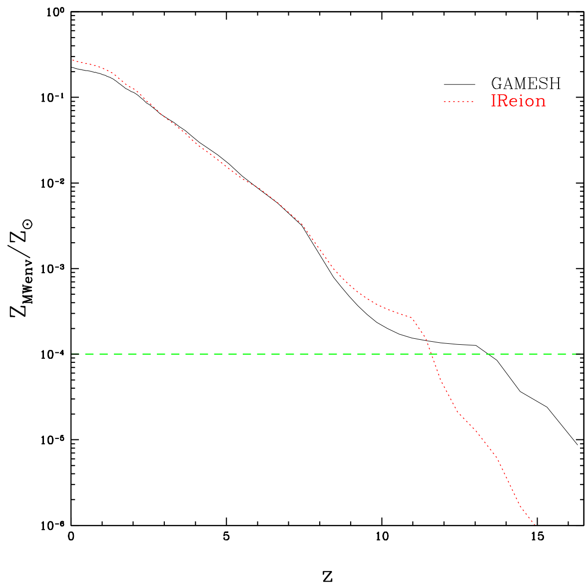

Figure 4.8 *Evolution in redshift of the MW environment metallicity Z_{IGM} (solid black line) in solar metallicity units. The values obtained by assuming instant reionization are shown in dotted red line. The green dashed line shows, as reference, the value adopted for the critical metallicity to form Pop II stars.*

0.99 up to 0.999. The dashed line indicates that isolated, high redshift galaxies ($z > 12.4$) are quite insensitive to their environment and the radiative feedback plays only a local role. A quick comparison with the blue dotted line clearly shows that these galaxies mainly form Pop III stars. After the population transition, Pop II forming galaxies are instead progressively affected by their environment: below $z \sim 8$, both the increase of the virial radii of the sources and a more uniform ionizing background make the environment progressively more important and the feedback acts globally. At these redshifts the gas temperature is sustained by: (i) the few satellite galaxies surviving radiative feedback, (ii) the global UVB entering the box, and (iii) the predominant emission from the central MW-type galaxy. It is in fact clear from Fig. 4.7 that less than 40% of galaxies is capable to accrete gas from the surrounding reservoir to fuel the star formation process below $z \sim 4$.

4.3.3 Interplay with chemical feedback

In this section we briefly investigate how the reionization process can leave specific signatures in the chemical evolution of the MW environment and in the final properties of the MW at $z = 0$ and, in particular, of the most metal-poor stars observed in the Galactic halo.

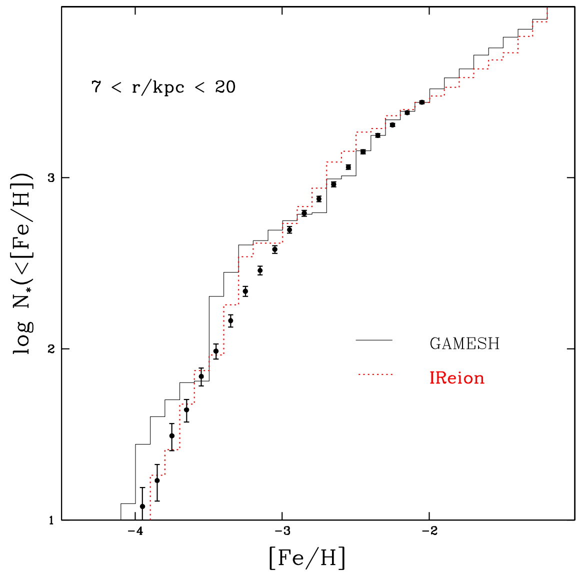

Figure 4.9 *MDF of the central galaxy calculated by* GAMESH *(solid black line) and in the IReion case (dotted red line) in the radial range* $7 < r < 20$ *kpc. Black points indicate observed data taken from Beers & Christlieb 2005.*

In Fig. 4.8 we show the redshift evolution of the IGM metallicity Z_{IGM}[8] predicted by GAMESH (solid black line) and the corresponding values obtained by assuming instant reionization (dotted red line). As already noted commenting Fig. 4.4 and 4.5, the star-formation history of Pop III stars is remarkably different when an accurate model for the radiative feedback is taken into account and their rapid burst, predicted by our simulation, is clearly imprinted in the metallicity of the diffuse, external medium. In fact, Z_{IGM} experiences a rapid increase at high redshift, reaching the critical value $Z_{cr} = 10^{-4} Z_{\odot}$ already at $z \sim 14$.

After a flat evolution corresponding to the Pop III to Pop II transition the increasing trend is restored by the increase in SFR of Pop II stars. As for the SFR (see Fig. 4.4), Z_{IGM} becomes consistent with the value predicted by the IReion case in the redshift interval $3 < z \leq 8$ after which it flattens. Note that a 15% difference in the SFR at $z = 0$ due to an extended reionization is reflected in 25% decrease of the final metallicity Z_{IGM}.

It should be noted that the trend at high redshift is certainly un-physical because the metallicity of the medium surrounding the galaxies on our box scale is expected to increase more progressively in redshift from very low Z_{IGM} as correctly predicted by the IReion model. We thoroughly investigated what causes this trend, finding a concurrence of reasons. First, our N-body simulation does not provide a sufficient mass resolution to accurately predict the distribution of low mass mini-halos, which are expected to have played a relevant role in the early metal

[8]This value is defined as the metallicity of the medium surrounding the collapsed halos and it is calculated as ratio of the mass of metals over the total mass of the gas.

enrichment of the MW and its dwarf satellites (see for example Salvadori & Ferrara 2009; Sales et al. 2014; Salvadori et al. 2014). As a consequence GAMESH tends to over-estimates the production/dispersion of metals in the first star-forming objects. Second, as indicated by pure semi-analytic calculations that simultaneously reproduce different data-sets at $z = 0$ (see Salvadori & Ferrara (2012); Salvadori et al. (2014)), a better description of both the stellar life-times and the in-homogeneous dispersion of metals into the IGM is required when the effect of an in-homogeneous reionization are considered. Finally, on the radiative feedback side, the extension of the frequency range to a Lyman-Werner frequency band is necessary to correctly reproduce the star formation in H_2-cooling halos.

The MDF of ancient stars in the final MW-like galaxy, clearly reflects the different evolution of both the total SFR and Z_{IGM} at $z > 8 - 10$, where the majority of [Fe/H] < -3 stars are formed (see the discussion in Sec. 2.6). In Fig. 4.9 we compare the MDFs of $z = 0$ stars in the radial range 1 kpc $< r <$ 20 kpc for the IReion and GAMESH runs. Black points with errorbars show the available data for Galactic halo stars in the same Galactocentric ranges (see also SF10).

Both curves show a satisfactory agreement in the overall trend of the observed data, and the differences between the two runs are much smaller than the errors induced when considering different MW merger histories (Salvadori et al. 2007, see also Sec. 2.5). While the GAMESH run fits the data for [Fe/H]> -3 (see Beers & Christlieb 2005), it clearly overproduces the number of low-metallicity stars, [Fe/H]< -3. This is due to the slower progress of metal enrichment, as reflected by the shallow increase of Z_{IGM} in the redshift range $8 < z < 13$ (see the plateau in Fig. 4.8). We interpret this issue as a clear indication that the current resolution of the simulation does not allow to accurately trace star formation and radiative feedback at the highest redshifts.

4.4 Conclusions

In this work we investigated the early formation process of a MW-like galaxy by using GAMESH, a novel tool combining for the first time in the literature, a N-body simulation with a detailed chemical and radiative feedback in a self-consistent framework. Many aspects of the formation process have been discussed along the cosmic time as the evolution of the SFR, the Pop III to Pop II transition, the statistics of progenitor halos in which star formation is suppressed, and finally the interplay between chemical and radiative feedback in setting up the chemical properties of the Local Group and the final MDF of the Galactic halo.

Even with a low resolution N-body simulation, which lacks in statistics and does not allow to draw definite conclusions on many aspects of the problem, GAMESH has been proven to be an ideal tool to provide both a comprehensive vision of the early formation of the Galaxy and its reionization process, and to include an accurate self-consistent treatment of chemical, mechanical and radiative feedback in numerical simulations.

The capability of GAMESH to switch between pure semi-analytic treatment and inclusion of accurate RT enabled us to carefully compare and contrast all the results obtained by both models and to compare with observed properties of the Galaxy and the surrounding environment at $z = 0$. In addition, the GAMESH algorithm is very general and does not limit its field of applicability to a MW formation process; it can be extended and adapted to a wide range of galaxy and star formation related topics.

In order to improve the DM halo statistic, in the next Chapter we apply the GAMESH pipeline to a N-body simulation with higher mass resolution. This allows to better follow the build up of DM and baryonic properties of a MW-like halo in a local volume. With this improved resolution, we will also be able to better account for the star formation in mini-halos and to determine their role in the MW formation process.

5

The history of dark and luminous matter in the Milky Way environment

In this Chapter the GAMESH pipeline is coupled with a new DM only Galaxy formation simulation performed with the numerical scheme GDC+ (Kawata & Gibson, 2003a) leading to the formation of an isolated, MW type halo in a cosmic cube of about 4 cMpc side length, with a better resolution with respect to the N-body simulation described in the previous Chapter. Here we present a preliminary analysis of the new simulation, investigating the evolution of the dark matter and baryons.
We first extract the DM merger tree of the MW-type halo, and quantify the relative importance of mergers and accretion during its assembly. Then we follow the star formation and the chemical enrichment history, comparing the resulting SFR, mass of stars, gas and metals at z = 0 to values inferred by observations. This allows us to calibrate the simulation by fixing the two free parameters of the model, i.e. the star formation efficiency in Lyman-α cooling halos and the efficiency of SN-driven winds. Finally, we analyze the properties of the MW progenitor population at $0 < z < 4$, and we find that they follow observed galaxy scaling relations, showing that the simulation is able to adequately describe the baryon cycle along the Galaxy assembly history. A further work will complement that presented here by investigating the interplay between chemical and radiative feedback in a full reionization context.

The Chapter is organized as follows. In Section 5.1 we introduce the new DM simulation, we describe the halo catalogue, the assembly history and the properties of the resulting MW halo type. Section 5.2 describes the calibration of the GAMESH simulation on a set of properties from observations and models. Section 5.3 shows the simulation results, while Section 5.4 finally summarizes the preliminary conclusions of this Chapter.

5.1 DM Galaxy formation simulation

In this section we describe the DM only simulation performed to obtain a MW-size halo. We first describe the numerical scheme adopted in GDC+, the initial conditions of the simulation, the halo catalogue and its merger tree. The properties of the MW halo are finally described as well as the statistics of various halo populations in a surrounding volume of 4 cMpc side length.

5.1.1 GDC+ and initial conditions

Pure N-body cosmological simulations of a MW-sized halo are run with GCD+ (Kawata & Gibson, 2003a; Kawata et al., 2013) with a β-version of periodic-boundary condition capability with TreePM algorithm with parallel FFTW module. We used initial conditions created with MUSIC (Hahn & Abel, 2011) with Planck cosmology (Planck Collaboration et al., 2014). We identify a MW-sized halo, and created a zoom-in initial condition. The final simulation consists of a total of 62421192 particles, 55012200 of which in the highest resolution region. The particle mass of the highest resolution is 3.4×10^5 M$_\odot$. The virial mass of the halo simulated is 1.7×10^{12} M$_\odot$.

We store the simulation output every 15 Myr from $z \sim 20$ down to $z = 10$, and every 100 Myr after this redshift. The total number of output snapshots is 155. This high enough time resolution is crucial for GAMESH application.

We analyzed the DM density at 512^3 grid points in the 4 cMpc side volume centered on the target DM halo.

Finally, we note that the initial conditions have not been selected to reproduce the observed structural and dynamical properties of the Local Group (LG), but rather to simulate a candidate MW-like halo at high resolution. As a result, the central 4 cMpc volume contains a total collapsed mass of $M_{DM} \sim 3 \times 10^{12} M_\odot$ and M31- or M32-sized halos are found instead in the larger 8 cMpc region.

5.1.2 Halo catalogue

We identify the sub-halo at every snapshots using a standard friend-of-friends (FoF) algorithm with a linking parameter of $b = 0.2$ and threshold number of particles of 100.

Hereafter we define as LG the cube of 4 cMpc side centered on the most massive halo of the simulation. Note that LG is the maximum volume resolved exclusively by the high-resolution DM particles of GDC+.

5.1.3 Merger trees and dynamical interactions

For each halo found by the FoF at redshift z_i, we have built its merger tree (MT) by iteratively searching all its particle IDs (pIDs) in the previous snapshots, back to the initial redshift z_1.

A OpenMP[1] parallel searching technique, specifically tuned on the simulation data, has been developed to build up the merger tree correlating the pIDs and halo IDs (hIDs) and to establish the ancestor/descendant relationships among hIDs found in $[z_i, z_{i-1}]$. It should be noted that once a pID at z_{i-1} is not associated with any hID, it is searched in the non collapsed part of the volume and associated with a reserved value we call "IGM ID". We also verified that due to the re-centering technique adopted by GDC+, few pIDs are sporadically not found in the LG volume because not geometrically captured. These pIDs are then classified as "missing" and their associated hID marked as hID$= -1$, to exactly conserve the total mass.

While extremely demanding in term of computational processing, once done, this approach allows us to exactly conserve the mass across dynamical interactions of DM halos with their environments and to exactly follow all their dynamical processes regulating the accretion of DM halos: mergers, tidal stripping and halo disruptions. All these events can then be classified and analyzed and their baryonic counterpart exactly handled in the semi-analytic code. Baryonic properties (generally gas mass, metal mass and stars) can be then properly transferred throughout collapsed structures or returned to the baryonic IGM, by scaling with the mass contribution or by associating them to the single DM particle dynamics and mimic an in-homogeneous spreading in the IGM of the local volume (see Section 5.1 for more details).

We classified the various dynamical interactions occurring during the mass assembly in the following categories:

- halo growth by accretion: this event occurs when an isolated halo acquires particles only from the IGM, typically by mass accretion.
- Halo growth by merger: when a halo at snapshot z_{i+1} results in a contribution of two or many halos at z_i, and possibly the IGM.
- Halo stripping: when a halo loses part of its mass by tidal interactions with nearby halos.
- Halo destruction: when a halo found at z_i loses its identity at z_{i+1} because it is disrupted by tidal interactions and its particles are returned primarily in the IGM.

In the next section we describe the assembly history of the most massive, MW-like, DM halo found at the center of the LG cube at $z = 0$.

5.1.4 The Milky Way DM halo assembly

Here we describe the assembly history of the MW halo defined above, in the context of its LG.

[1] www.openmp.org

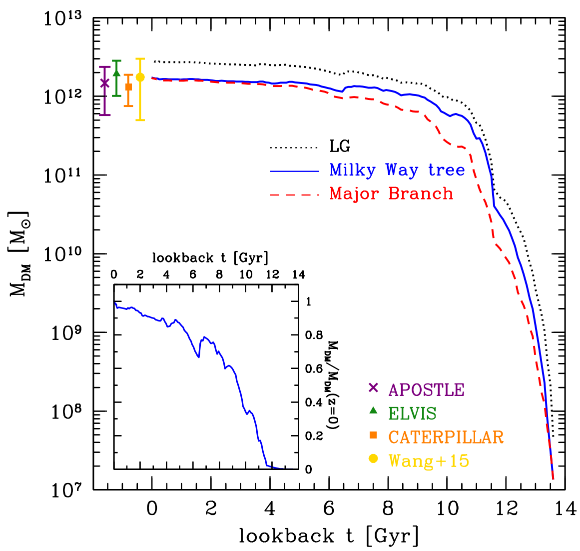

Figure 5.1 *Build up history of the central, MW-sized halo in the adopted N-body simulation. The total DM mass of all the MW progenitors (M_{DM}) is shown as function of the lookback time t as solid blue line. The dashed red line shows the MW merger tree as obtained by following the major branch only. The total collapsed mass enclosed in the LG volume is shown as the dotted black line. For reference, the mass of similar MW-sized halos taken from DM simulations or independent methods is also shown. See text for details. The enclosed panel illustrates the same MW history by plotting $M_{DM}(z)/M_{MW}(z=0)$ instead of the total collapsed mass.*

Figure 5.1 shows the total mass of the MW halo merger tree (solid blue line) as a function of the lookback time (t). The dotted black line refers instead to the total collapsed mass found in the LG. As described above, our merger tree has been built particle-by-particle and the blue line accounts, by design, for the entire populations of halos which will collapse onto the MW by $z = 0$, formed at all scales. To highlight the importance of having an accurate merger tree we also show, as dashed red line, the MT resulting by following only the most massive halo (M_{MM}, or major branch) at each z_i. It is immediately evident that by following the build up history along the major branch, the error in mass becomes relevant at high redshift where a sensible fraction of the collapsed mass is distributed in a large number of MW progenitor halos. The two MTs converge instead at $t = 4$ Gyr, (i.e. $z \sim 0.3$) where a large fraction of the final MW is already collapsed in M_{MM}. To understand the build up time scale, we computed the so called 'characteristic time' (t_a) for the assembly of the MW halo, operationally defined as the redshift at which $M_{MM}(z) = M_{MW}(z = 0)/2$ (see Mo et al. 2010) and it results in $t = 4.36$ Gyr, i.e. $z = 1.46$. Note that this estimate is compatible with the histories found in an independent set of DM simulations described in Behroozi et al. (2013, see in particular their Figure 19), and relative to halos of similar mass. Also note that the same time obtained from the blue line (i.e. accounting for all progenitors, see Navarro et al. 1996) results in $t = 2.66$ Gyr ($z \sim 2.45$), further indicating the importance of accounting for the large fraction of mass present as independent

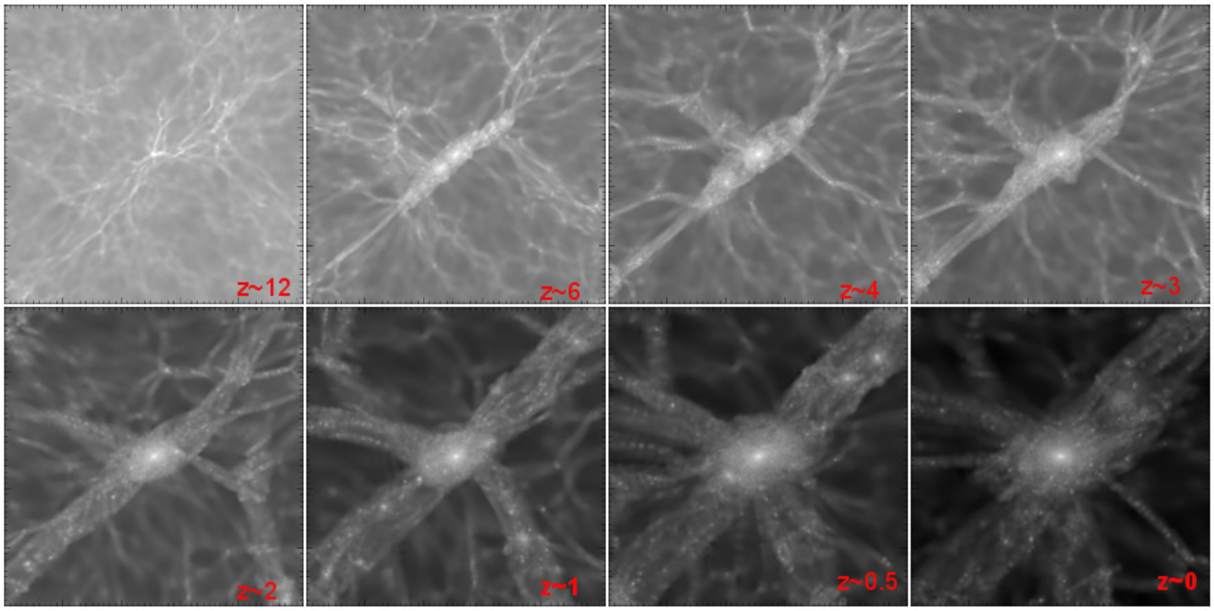

Figure 5.2 *Slice cuts of the LG evolution at various redshifts. The panels show the gas number density distribution obtained by scaling the DM mass in each cell of the spatial grid by the universal baryon fraction. The spatial resolution is $r \sim 7.8$ kpc.*

collapsed structures at high redshift.

Since in the literature the halo build up histories are usually shown as $M_{DM}(z)/M_{MW}(z=0)$, in the bottom left corner of this figure, we show the same history in this units for a more straightforward comparison with other simulations (see for example Figure 9 in Griffen et al. 2016).

The resulting MW mass found at $z = 0$ ($M_{MW} \sim 1.7 \times 10^{12} M_\odot$) is finally compared with the scatter in mass of MW-size halos found in recent simulations targeting the Local Group, both DM-only (the ELVIS simulation suite by Garrison-Kimmel et al. 2014 and the CATERPILLAR project by Griffen et al. 2016) and the recent hydro-dynamical APOSTLE simulation (Fattahi et al., 2016; Sawala et al., 2016). In all the cases we find a remarkable consistence of our MW halo mass with these independent results[2]. Finally note the additional agreement with the gold filled circle, showing estimates of Wang et al. (2015), obtained by using dynamical tracers.

To understand the MW growth within the global evolution of its LG, one can compare the blue and black solid lines of Figure 5.1 and cross-check with the visual picture provided by Figure 5.2, that shows a series of slice cuts illustrating the redshift evolution of the LG and the central MW galaxy. Here the gas number density, obtained by scaling the DM mass by the universal baryon fraction, is shown as gradient from white (collapsed regions) to black (voids).

It is immediately evident that while at high redshifts the collapsed mass of both MW and LG

[2]Note that the scatter in these values is obtained from the scatter in the MW-halo samples found in the various runs.

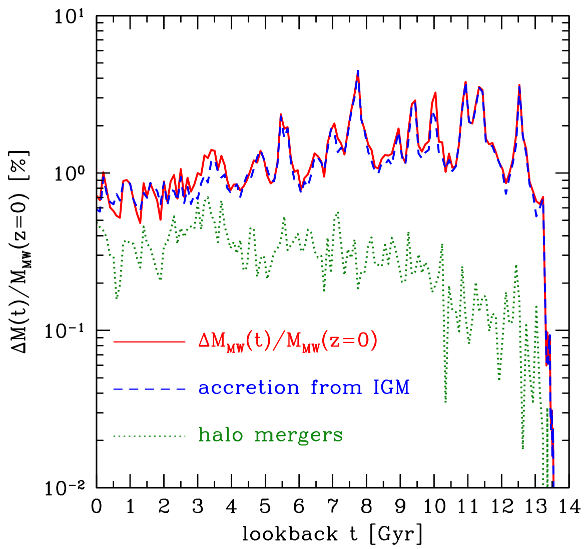

Figure 5.3 *Differential contribution of DM mass, relative to the final MW mass, as a function of the lookback time t (solid red line). The contributions from the IGM and collapsed structures are shown as dashed blue and green dotted lines respectively.*

have a similar evolution[3], below $t = 11$ Gyr ($z \sim 2$) many structures not belonging to the MT of the MW, start collapsing in the entire volume or enter the LG domain from the larger scale[4]. The evolution at high redshifts proceeds by assembling collapsed structures along the diagonal filament created by the collapsing sheet. This is easily visible in the first slice cuts (top row, from left to right) where the time evolution of the main web filaments is shown. Below $z \sim 3$, the central halo dynamically dominates the LG region and continues to drag material entering from larger scales: around $z \sim 2$ in fact, an external filament not previously visible within 4 cMpc provides collapsed halos to the central galaxy. This is a clear indication that galaxy formation is a multi-scale, multi-environment process, assembling baryonic mass created in different environments (see also Section 5.3). At the final time ($z = 0$) the central halo shows a complex interplay with many filaments where a plethora of satellite galaxies are still collapsing towards the central attractor[5].

As explained in Section 5.1.3, the accuracy of our MT allows us to disentangle the different growth processes (halo mergers or accretion from the IGM) and to describe their relative contribution. The result of this analysis is provided in Figure 5.3 where we show the percentage of mass increase relative to the final MW mass ($\Delta M(t)/M_{MW}(z = 0)$), as a function of the lookback time t (solid red line). It is immediately evident that across cosmic times, the MW

[3]This is mainly because all the halos collapse first along a filament at the center of the box.
[4]This is the 8 cMpc scale assumed by GDC+ to gravitationally constrain the LG domain.
[5]An animation can be found in the article online resource files.

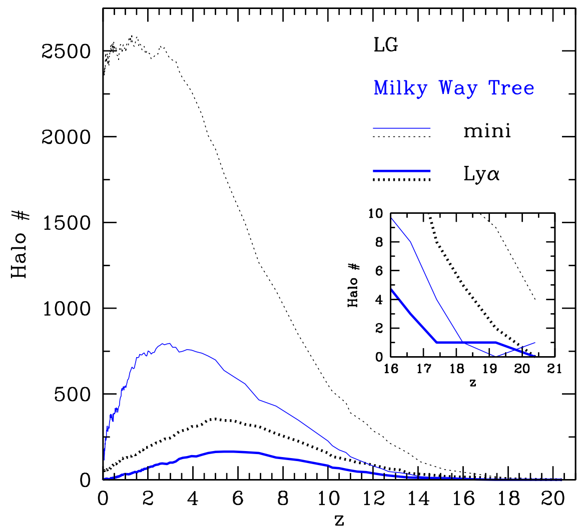

Figure 5.4 *Number of halos found in the LG (black dotted lines) and participating to the merger tree of the MW (blue solid lines) as a function of redshift. Mini-halos (Lyman-α cooling halos) are shown with thin (thick) lines. The enclosed panel shows a zoom-in at high redshift.*

halo grows by means of a smooth and continuous assembly of matter spaced out by many violent accretion events, each of which provides a $\sim$3% contribution to the final mass (see for example the spikes around t = 12.5 Gyr (z = 4.68) and t = 11.5 Gyr (z = 2.64)). As a further example note that a major event, increasing the mass of the most massive halo by 5%, is found around $t \sim 8$ Gyr (i.e. z = 1.02), and this corresponds to the last major merger experienced by the MW galaxy. Below t = 3 Gyr ($z \sim 0.2$) both the mergers and the accretion from the IGM phase become smoother and the mass growth progresses with steps contributing for less than 1% to the final mass.

The relative contribution of accretion and mergers can be understood by comparing the dotted green line with the dashed blue line (IGM accretion) and the dotted green line (halo mergers). While mass accretion from the surrounding IGM is dominating at all times, the green line shows an increasing number of halo mergers at low redshifts, with a substantial contribution around $t \in [2-4]$ Gyr (i.e. $z \in [0.15-0.35]$). It should be noted though, that while halo mergers contribute on average for less that 0.5 % to the final DM mass, their stellar, gas and metal contents contribute to shape the observed properties of the MW (see Section 5.2). It is then very important to complement the information provided by the dynamics of the DM with the relative contribution of mini-halos ($T_{vir} < 10^4$ K) and Lyman α- (Lyα-) cooling halos ($T_{vir} > 10^4$ K). In fact, the different impact of radiative and mechanical feedback processes on these two populations affect their evolution and leave imprints on observable properties of the MW, such as the metallicity distribution function of the most metal-poor stars in the Galactic halo (as discussed in previous Chapters).

Figure 5.4 shows the redshift evolution of the number of mini-halos (thin lines) and Lyα-cooling halos (thick lines) along the merger tree of the MW (blue solid lines) and in the LG (black dotted lines). First note the plethora of mini-halos predicted by the DM simulation around the MW at $z = 0$. In fact, during its mass assembly, less than 30% of the entire mini-halo population in the LG volume is embedded in the final MW halo; these halos remain in the LG, providing a trace of the environmental conditions experienced by this volume along its redshift evolution. While the same considerations apply for the more massive population of Lyα-cooling halos, their number is about one order of magnitude lower, with very few objects ($\mathrm{N_{Ly\alpha}} \sim 60$) still orbiting around the MW halo at $z = 0$.

5.2 Baryonic evolution

In this work we follow the baryonic evolution of the galaxies associated with the DM halos by running only the semi-analytic part of the GAMESH pipeline. This means that radiative feedback is simulated by adopting a redshift dependent minimum mass of star forming halos (Salvadori & Ferrara 2009, 2012, see also Ch. 3) and assuming an instant reionization at $z_{\mathrm{reio}} = 6$ (as in Ch. 2 and 4). In a future work we will investigate the effects of radiative feedback on star forming galaxies in the proper context of a local volume reionization simulation, performed by enabling the CRASH side of the pipeline, as done in the previous chapter.

A change in the N-body simulation implies a recalibration of the two free parameters of GAMESH, namely the star formation efficiency in Ly-α cooling halos, ϵ_*, and the efficiency of supernova-driven winds, ϵ_w. Following Salvadori & Ferrara (2009, 2012), the star formation efficiency in mini-halos is assumed to be $\epsilon_{\mathrm{MH}}/\epsilon_* = 2[1 + (T_{vir}/2 \times 10^4\mathrm{K})^{-3}]^{-1}$, as a result of the reduced efficiency of gas cooling (see also Valiante et al. 2016 and Sec. 3.1.1). When $z \leq z_{\mathrm{reio}}$ star formation can only occur in galaxies with $T_{vir} > 2 \times 10^4$ K, to account for the effects of photo-heating and photo-evaporation (see Ch. 4 for a thorough comparison between the instant reionization model and the model with a self-consistent reionization history computed by GAMESH).

As discussed in the previous Chapter, we calibrate the free parameters of the model by requiring the star formation rate, the stellar and gas masses, and the metallicity of the simulated MW galaxy at $z = 0$ to match the observationally-inferred values. For some of these quantities, such as the star formation rate or the total gas mass, the values inferred by different studies show up to one order of magnitude difference, as a result of the different tracers used in the observations or of the modeling strategy adopted to reconstruct the galaxy components (bulge, disk and halo). A large collection of critically revised estimates and galaxy modeling techniques can be found in Kennicutt (1998); McKee & Ostriker (2007); Kennicutt & Evans (2012); Bland-Hawthorn & Gerhard (2016).

Besides the different methodologies, in the last years the total stellar mass (M_*) inferred for the MW has largely converged to a value of $M_* = [3 - 7] \times 10^{10} M_\odot$, as proven by a series of independent estimates (Flynn et al., 2006; McMillan, 2011; Bovy & Rix, 2013; Kubryk

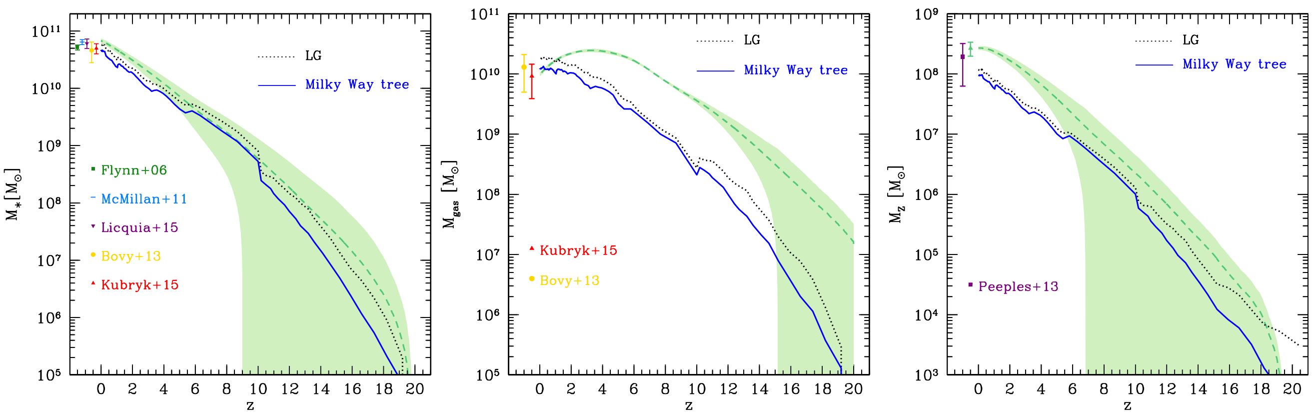

Figure 5.5 *Redshift evolution of the total stellar (left panel), gas (middle) and metal (right) masses. In each panel, the values predicted by* GAMESH *for the Local Group and for the merger tree of the MW are shown with black dotted and blue solid lines, respectively. The dashed green lines show the values computed in Sec. 2.3 as averages over 50 independent Monte Carlo realizations of a semi-analytical merger tree for a* $10^{12} M_{\odot}$ *DM halo (the shaded areas show the corresponding 1-*σ *deviation). Observations for the stellar and the gas masses at* $z = 0$ *are taken from Flynn et al. (2006, green square), McMillan (2011, azure minus), Licquia & Newman (2015, violet downtriangle), Bovy & Rix (2013, yellow circle), Kubryk et al. (2015, red uptriangle). The derivations of the mass of metals at* $z = 0$ *are taken from Peeples et al. (2014, violet square) and from that used in Sec. 2.3 (light green triangle). Note that in the middle and right panels the blue solid and black dotted lines correspond to the mass of gas and metal used in star formation, while the green dashed lines with the shaded regions refer to the total gas and metal mass (see text).*

et al., 2015; Licquia & Newman, 2015). These are shown by colored points in the left panel of Figure 5.5. In the same panel, we show the redshift evolution of M_*, as predicted by the semi-analytic model shown in Ch. 2 (solid green line with the shaded region) and the stellar mass assembly predicted by GAMESH for the LG and for the merger tree of the MW, when $\epsilon_* = 0.09$ and $\epsilon_w = 0.0016$. The model is in good agreement with the observations, with a final value of $M_* \sim 4.6 \times 10^{10}$ M$_{\odot}$ for the MW halo candidate. It also predicts a total stellar mass of $\sim 6 \times 10^{10}$ M$_{\odot}$ in the LG. The redshift evolution is also consistent with that predicted by the semi-analytical model and its statistical scatter.

Below $z \sim 4$ the models show a different evolution, and at $z = 0$ the semi-analytical model predicts a mass $M_* \sim 7 \times 10^{10}$ M$_{\odot}$ with a star formation efficiency $\epsilon_* = 0.8$, i.e. one order of magnitude higher than the value required by GAMESH. The reason for this difference can be partly ascribed to the different mass of the final MW DM halo, which in Chs. 2 and 3 is assumed to be $M_{\rm MW}(z = 0) = 10^{12} M_{\odot}$, a factor of 1.7 smaller than the value predicted by the N-body simulation adopted here. In addition, at $z \leq 4$ the GAMESH MW halo progenitors have systematically one order of magnitude higher total gas mass than the ones predicted by the semi-analytic model.

This can be seen in the middle panel of Figure 5.5, where we show the redshift evolution of the gas mass. Here the black dotted and blue solid lines represent the mass of gas used in star formation i.e. $\sim 0.1 M_g$, while the green dashed line represents to the total M_g predicted by in Ch. 2. As illustrated in Section 5.1.4 and in Figure 5.2, the early assembly of the MW halo in the N-body simulation is dominated by mass accretion and mergers of nearby halos, and the evolution is similar to the one predicted in Sec. 2.3 using the semi-analytical merger trees based on the Extended Press Schechter formalism (EPS, Press & Schechter 1974). When $z < 4$, the simulated MW-halo grows by many episodes of violent accretion and mergers with halos entering the LG from the larger scales. All these effects cannot be accounted for by the semi-analytical merger trees.

Despite the intrinsic differences found in their assembly histories, both models predict a final gas mass in the MW in agreement with the observed values. Here the comparison should be taken with caution. In fact, the total gas mass in the MW includes the cold and warm components (molecular and atomic phases mainly in the disk) and a hot halo (coronal) component, as exhaustively detailed in Bland-Hawthorn & Gerhard (2016). The observations reported in the middle panel of Fig. 5.5 refer to the total interstellar medium (ISM) mass in the disk as inferred from dynamical measurements (Bovy & Rix, 2013, yellow circle), and by averaging the values of the atomic and molecular gas masses obtained by different observational studies (Kubryk et al., 2015, red uptriangle). We note that using the most likely mass range for the Galactic corona $(2.5 \pm 1) \times 10^{10} M_\odot$, (Bland-Hawthorn & Gerhard, 2016), the total baryonic mass is found to be in the range $[7 - 11] \times 10^{10} M_\odot$. If we account for the total amount of gas enclosed in the MW halo, we find $\sim 1.3 \times 10^{11} M_\odot$.

Finally, in the right panel of Fig. 5.5 we show the evolution of the metal mass in the ISM. Here we do not follow separately the evolution of dust, hence all the lines show the total mass in heavy elements (gas-phase metals and dust). The models show behaviors which reflect their corresponding stellar mass assembly histories, and the model described in Ch. 2 predicts a higher metal content at $z = 0$, consistent with its higher $M_*(z = 0)$. Both models are in agreement with the violet square at $z = 0$, based on a detailed inventory of metal mass components in present-day L_* galaxies (Peeples et al., 2014). To be consistent with the observations reported in the other panels of Fig. 5.5, we have computed the mass of metals and dust in the ISM from the fitting functions of Peeples et al. (2014), using a stellar mass in the range $[3 - 7] \times 10^{10} M_\odot$ and we find $M_Z = [0.95 - 4.7] \times 10^8 M_\odot$. In addition, Peeples et al. (2014) provide an estimate of the CGM metal mass as probed by low- and high-ionization (O VI) species based on COS-halos data and of the mass of dust in the circum-galactic medium (CGM) based on the reddening of background quasars (Ménard et al., 2010). Taking the values from their Table 5 and adding the metal mass in the hot X-ray emitting CGM gas[6], we infer a total mass of heavy elements in the CGM within a radius $r \approx 150$ kpc of $1.7 \times 10^8 M_\odot$ with minimum (maximum) values of $0.9\,(3.7) \times 10^8 M_\odot$. Hence, the total estimated mass of metals is found to be in the range $[1.85 - 8.4] \times 10^8 M_\odot$. If we assume the metals to follow the DM halo radial profile at these large radii, we find $M_Z(r < 150$ kpc)

[6] We compute this quantity from equation (24) in Peeples et al. (2014) assuming a stellar mass of $[3-7] \times 10^{10} M_\odot$.

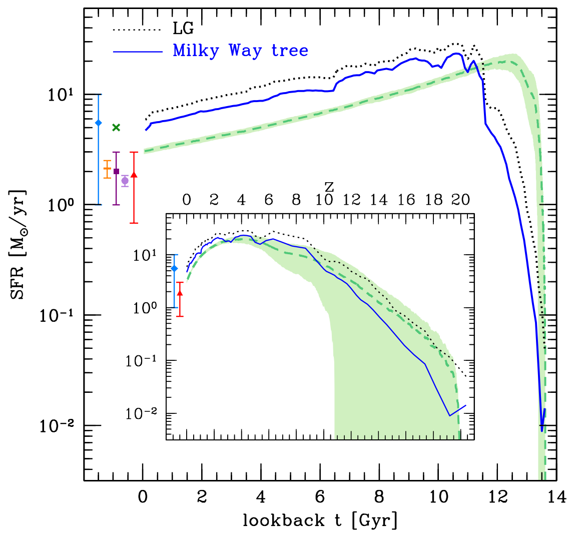

Figure 5.6 *Total star formation rate in the MW merger tree (solid blue line) and in the LG (dotted black line) as function of the lookback time. The average SFR found in Sec. 2.3 is shown with dashed green line, with the shaded region showing the 1−σ dispersion. In the enclosed panel the same quantities are shown as function of z. Data points with errorbars, when available, are taken from the literature (see text for details).*

predicted by the simulation to be $6.9 \times 10^8 M_\odot$, in agreement with the observed value.

Hence, we conclude that having selected the two free parameters to be $\epsilon_* = 0.09$ and $\epsilon_w = 0.0016$ the stellar mass and the mass of gas and metals in the ISM predicted by GAMESH for the MW-like halo at $z = 0$ are consistent with the observations. A multiphase treatment of the gas and dust evolution in GAMESH, similar to what presented in Ch. 2 and 3, will be implemented in the future.

In Figure 5.6 we show the total star formation rate (SFR) predicted by our model as function of the lookback time. Data points indicate observationally inferred estimates found in the literature, from the oldest estimates by Smith et al. 1978 (SFR$\sim$ 5 $M_\odot$ yr^{-1}, dark green cross), McKee & Williams 1997; Diehl et al. 2006 (SFR$\sim$ 4 $M_\odot$ yr^{-1}, violet square) to the newest, generally lower values around SFR$\sim$ 2 $M_\odot$ yr^{-1} e.g. Robitaille & Whitney 2010 (orange minus), Licquia & Newman 2015 (light-violet circle), Kubryk et al. 2015 (red triangle).

As exhaustively discussed in Chomiuk & Povich (2011), the number of assumptions needed to derive the total SFR of the current MW (for example in its structure, its stellar sample and stellar IMF) is so large that the resulting scatter can span one order of magnitude (see the azure diamond with the largest errorbars). For the MW-like halo at $z = 0$, GAMESH finds a SFR$\sim$ 4.6 $M_\odot$ yr^{-1}, a factor of two higher than recent estimates but still compatible with the data scatter. In the enclosed panel, we show the same SFR as a function of redshift z, to better visualize the

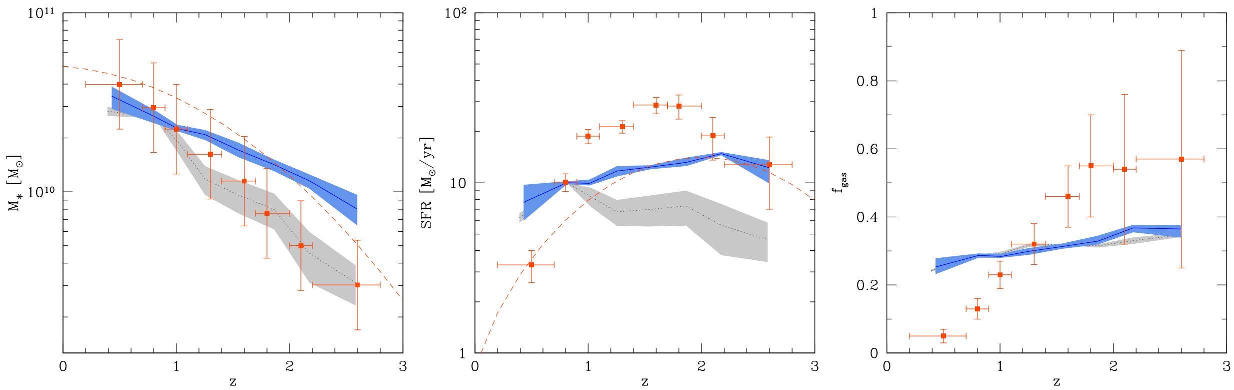

Figure 5.7 *Comparison between the stellar mass (left panel), SFR (middle panel) and gas fraction (right panel) of MW progenitors in the* GAMESH *simulation and observational data from Papovich et al. (2015, red points). The blue solid lines show the average values among MW progenitors selected in each redshift bin following the same procedure adopted by Papovich et al. (2015). The grey dotted lines show the results when the minimum mass adopted to select MW progenitors in each redshift bin is decreased by 0.75 dex (see text). The shaded regions represent the 1-σ scatter around the mean.*

evolution at high redshift.

While the global trend of the SFR predicted by GAMESH agrees with the one found in Ch. 2, and the two SFRs show similar values at their peaks ($\sim 15-20$ $M_\odot$ yr^{-1}), the latter are found at different redshits. The progressive, quasi parallel decline of the total SFR, results in final SFRs diverging by ~ 1.5 $M_\odot$ yr^{-1}. As argued for the gas and stellar mass behaviors, we ascribe these discrepancies to intrinsic differences in the MW mass assembly history, particularly at $z < 4$.

5.3 Properties of the Milky Way progenitors

So far, we have investigated the global properties of the simulated halos, in the MW merger tree and in the LG. In this Section, we discuss the SFR, the mass in stars, gas and metals predicted for MW progenitor systems at $0 < z < 4$ by the GAMESH simulations and compare these with observed values.

Recent studies have started to investigate the redshift evolution of progenitors of MW-like galaxies at $z = 0$, selecting candidates from very deep near-IR surveys on the basis of their constant comoving density (van Dokkum et al., 2013), of their evolution on the galaxy star forming main sequence (Patel et al., 2013), or of multi-epoch abundance matching techniques (Papovich et al., 2015).

Using a combined data sets based on the FourStar Galaxy Evolution (ZFOURGE) survey, CANDELS *Hubble Space Telescope* (HST), *Spitzer*, and *Herschel*, Papovich et al. (2015) derived photometric redshifts and stellar masses for MW progenitors and discuss their evolution with redshift. To compare with their analysis, we have extracted MW progenitors from the GAMESH simulation adopting a similar selection procedure. We first identify all the simulated systems in the same redshift bins of the observations, and then we select those with a stellar mass which falls within ±0.25 dex of the central stellar mass adopted by Papovich et al. (2015, see entries 1 and 2 in their Table 1). The number of selected progenitors ranges between 41 (in the lowest redshift bin, $0.2 < z < 0.7$) to 6 (in the highest redshift bin, $2.2 < z < 2.8$).

Figure 5.7 shows the resulting evolution of the average stellar mass (right panel), SFR (middle panel) and gas fraction (right panel), defined as $f_{\rm gas} = M_*/(M_{\rm gas} + M_*)$. The blue solid lines show the model predictions, with the shaded region representing the $1-\sigma$ scatter, and the red points are the Papovich et al. (2015) data. To increase the statistics of MW progenitors, particularly in the higher z bins, we also show the model predictions when the mass selection is done within ±1 dex of the central mass adopted by Papovich et al. (2015, grey dotted line with shaded region). We find that the simulated progenitors follow a stellar mass trend which is in good agreement with the observations, particularly if the mass selection includes a larger number of MW progenitor systems at $z > 1.5$. In agreement with previous studies, we find that more than 90% of the MW mass has been built since ~ 2.5. However, the star formation rate and the gas fraction of the simulated galaxies have a shallower evolution in the 3 Gyr period between $z = 2.5$ and $z = 1$ than found by Papovich et al. (2015). In particular, the peak SFR of $\sim 10\,M_\odot/{\rm yr}$ at $z \sim 1-2$ of the most massive MW progenitors is smaller than the value reported by Papovich et al. (2015), and in closer agreement with the evolution found by van Dokkum et al. (2013, see the red dashed lines). We find that the MW mass buildup can be fully explained by the SFRs of its progenitor systems, and does not require significant merging (van Dokkum et al., 2013). If star formation dominated the formation of the MW galaxy, then its growth must heavily depend on the evolution of cold gas and gas-accretion histories. This is consistent with the results presented in Section 5.1. In addition, by inverting the Kennicutt-Schmidt law, Papovich et al. (2015) show that the effective size and SFRs imply that the baryonic cold-gas fractions drop as galaxies evolve from high redshift to $z \sim 0$ (see the red data points in the right panel of Fig. 5.7). The predicted $f_{\rm gas}$ of the simulated sample shows instead a rather flat trend and, independently of the adopted selection criteria, the average SFR and gas fraction are larger than inferred by the observations below $z \sim 1$.

We have also checked the position of the simulated MW progenitors relative to the galaxy main sequence of star formation. In Fig. 5.8 we show the results using the same redshift bins adopted in Fig. 5.7, but without making any selection on the stellar mass. In each panel, the points represent all the simulated systems, while the dashed line is the analytic fit to the observations, taken from Schreiber et al. (2015, see their Eq. 9) and computed at the central redshift of each bin. There is a large scatter in the SFR of the smallest MW progenitors and most of the systems with $M_* < 10^8 M_\odot$ show SFRs that can vary by almost one order of magnitude. While the galaxy main sequence can not be constrained by observations in this regime, an increasing scatter towards low stellar masses has already been found in hydrodynamical simulations as a result of the rising importance of stellar feedback (Hopkins et al., 2014). Yet, the more massive among the MW progenitors at each redshift lie within a factor of 2 of the galaxy main sequence (the region

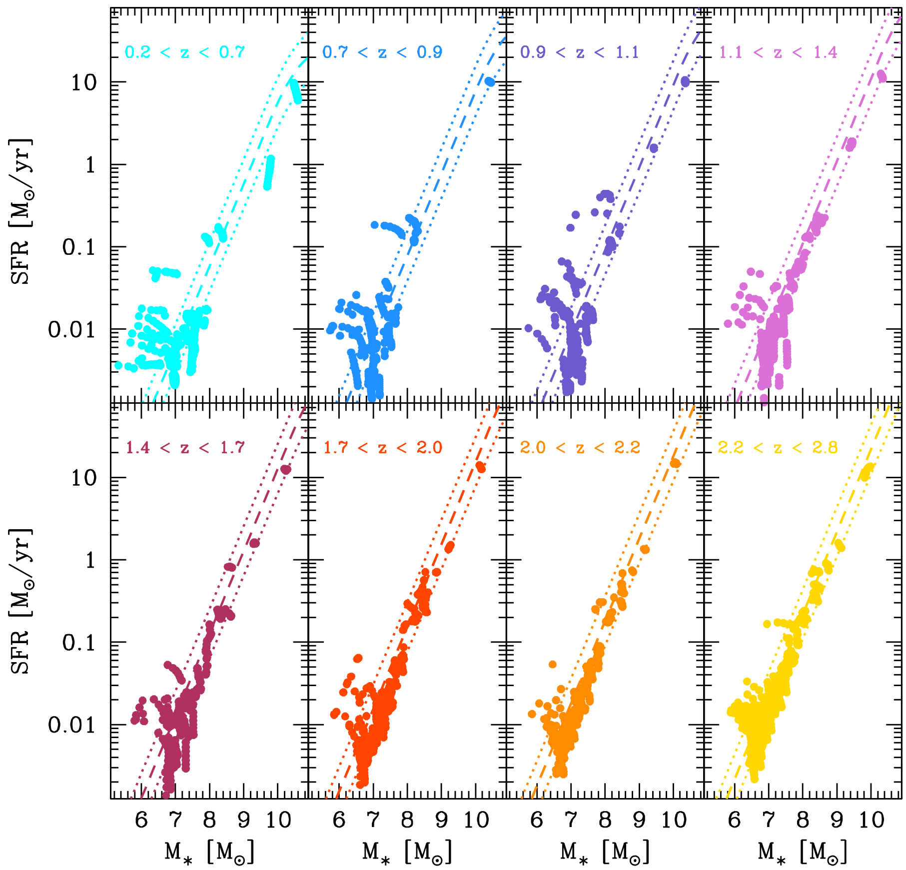

Figure 5.8 *The star formation rate as a function of stellar mass of all MW progenitors in different redshift bins, as indicated in the legenda. In each panel, the points represent the simulated systems and the dashed line shows the analytic fit to the galaxy main sequence at the central redshift of the bin, taken from Schreiber et al. (2015). The dotted lines are a factor of 2 above/below the fit.*

within the two dotted lines) all the way from $z \sim 2.5$ to $z \sim 0$.

Finally, we compare the gas metallicities of the simulated MW progenitors with the observed mass-metallicity relation (MZR) at different redshifts and with two (redshift independent) combinations of stellar mass, SFR and metallicity known as the fundamental metallicity relation (Mannucci et al., 2010, FMR) and fundamental plane of metallicity (Hunt et al., 2012, 2016a, FPZ).

The results are shown in Figs. 5.9 and 5.10, respectively. The interstellar oxygen abundance has been computed assuming a solar oxygen-to-metal mass ratio of 0.00674/0.0153 = 0.44 (Caffau et al., 2011b), so that the solar metallicity corresponds to 12 + log(O/H) = 8.759. The points represent all the simulated MW progenitors in the same redshift bins of Maiolino et al. (2008)

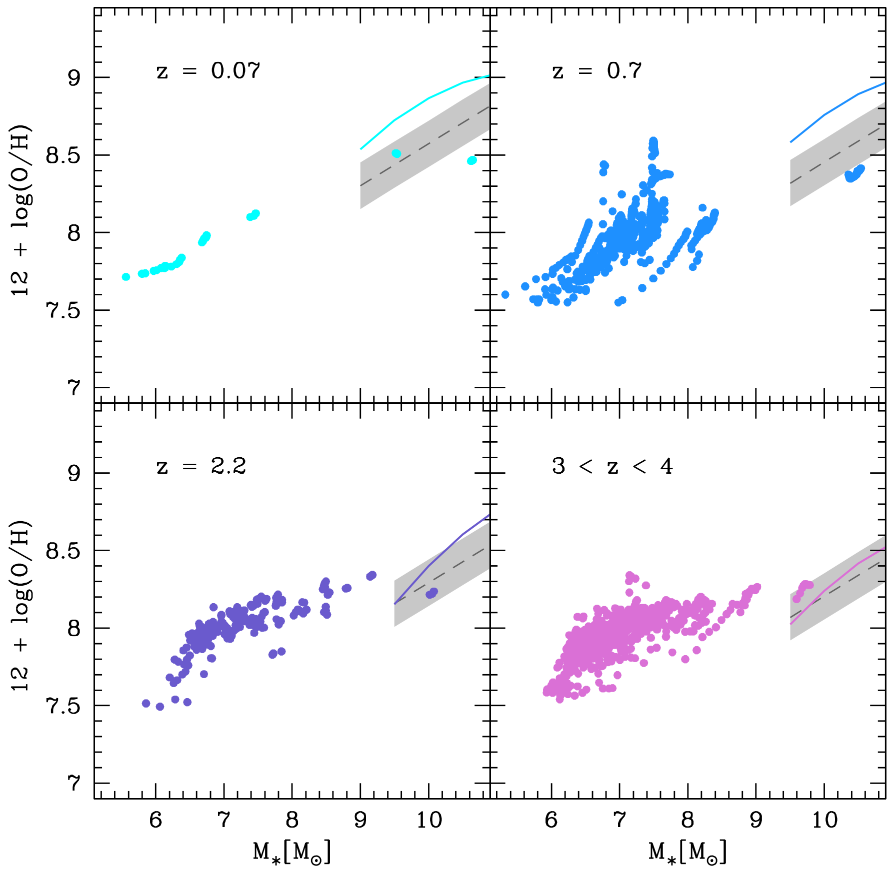

Figure 5.9 *The mass metallicity relation at different redshifts (see the legenda). The points show the simulated MW progenitors and the solid lines represent the fit to the observed relations at reported by Maiolino et al. (2008, at $z < 3$) and Mannucci et al. (2009, at $3 < z < 4$). The dashed lines are the fit obtained by Hunt et al. (2016a) with the shaded region showing the* ±0.15 *dex scatter.*

and Mannucci et al. (2009), without any additional selection on the stellar mass or star formation rate. Instead, the solid lines show the fit to the data and are drawn only in the mass range probed by the observations. It is clear that most of the simulated systems have stellar masses that are outside this range, except for the few most massive MW progenitors with $M_* > 10^9 M_\odot$. At $3 < z < 4$, these systems have metallicities slightly higher than those implied by the Mannucci et al. (2009) fit. However, at $z < 3$ the simulated systems fall systematically below the fits by Maiolino et al. (2008). A better agreement is found with the fit to the mass-metallicity relation proposed by Hunt et al. (2016a, and computed using their Eq. 2 at the average redshift of each bin), shown as the dark grey dashed line, with the shaded region representing a dispersion of ±0.15 dex.

A similar result is found in Fig. 5.10, where we show the position of the simulated MW

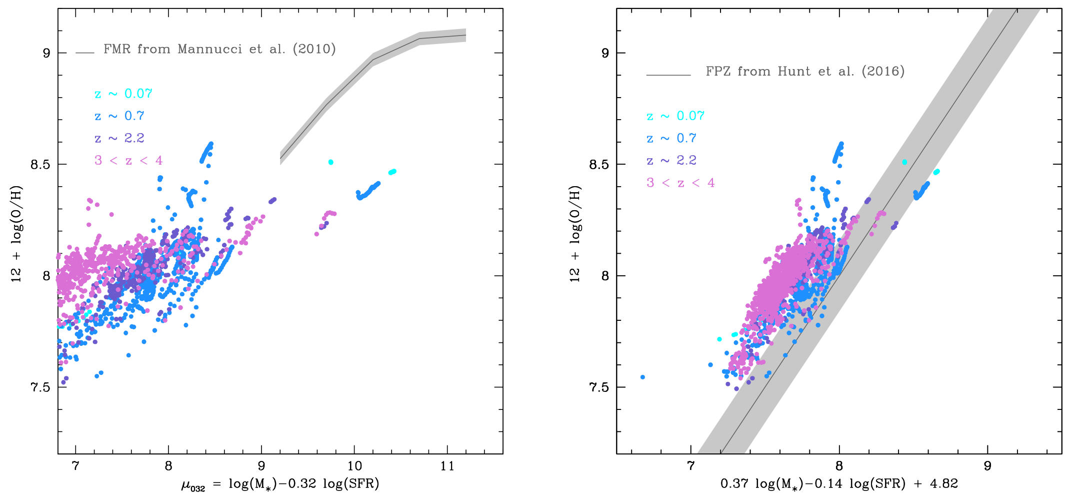

Figure 5.10 *Distribution of the MW progenitors relative to the fundamental metallicity relation by Mannucci et al. (2010, left panel) and to the fundamental plane of metallicity by Hunt et al. (2016a, right panel). All the simulated systems at* $\langle z \rangle = 0.07, 0.7, 2.2$ *and at* $3 < z < 4$ *(using the same color coding adopted in Fig. 5.9) are shown with data points. Dashed lines with shaded regions show the observed fits (see text).*

progenitors relative to the FMR (left panel) and FPZ (right panel). Here we have reported systems selected in the same redshift bins as in Fig. 5.9. As usual, smaller MW progenitors which populate the lower right side of the panels show a large scatter at all redshifts. The most massive MW progenitors align along the FMR but with a -0.5 dex metallicity offset. Conversely, their metallicity is within the scatter of the FPZ.

We conclude that while the simulated systems may be slightly too metal-poor at high stellar masses and too metal-rich at lower stellar masses, the discrepancy with the MZR evolution by Maiolino et al. (2008) and with the FMR by Mannucci et al. (2010) may be at least partly due to the different metallicity calibrations used by these authors, which may overestimate the observed metallicity by 0.3 dex (Hunt et al., 2016a, see in particular their Section 4.4). More interestingly, the distribution of the most massive MW progenitors is consistent with the FPZ and aligned with the FMR. Since these redshift-independent scaling relations between metallicity, stellar mass and star formation rate are believed to originate from the interplay between gas accretion, star formation and SN-driven outflows (see, among others, Dayal et al. 2013 and Hunt et al. 2016b), we conclude that the description of these physical processes in the GAMESH simulation leads to results consistent with observations at $0 < z < 4$.

5.4 Conclusions

In this Chapter we presented a preliminary analysis on a high resolution N-body simulation of a MW-like DM halo. The simulation has a better resolution with respect to that presented in Ch. 4, with a consequent improvement in the statistic of DM (mini-)halos, required to investigate high-z star formation and chemical enrichment under the influence of radiative and chemical feedback effects.

Firstly, we investigated the properties of the well-resolved final MW at the center of the simulated box, finding a DM mass at $z = 0$ of $M_{MW} \sim 1.7 \times 10^{12} M_{\odot}$, in very good agreement with the findings of both DM-only and hydro-dynamical simulations, and with observational estimates based on different dynamical tracers. To study the DM mass assembly of the simulated MW, we reconstructed its merger tree, and we found that by $z \approx 1.46$ it already gained half of its final mass.

Secondly, we ran the semi-analytical part of the GAMESH pipeline along the calculated merger tree to follow the evolution of the baryonic properties of the MW and of its progenitors. We found a good agreement between observed and simulated SFR, stellar, gas and metal mass at $z = 0$. Following recent studies on progenitors of MW-like galaxies, we analyzed the properties of MW progenitors and compared them to observations at $z < 4$. We found that the redshift evolution of the stellar mass and SFR of simulated MW progenitors is in good agreement with observations, although their gas fraction appears to have a shallower evolution at $0 < z < 4$ compared to the data. We found that the simulated MW progenitors follow the observed galaxy main sequence of star formation at $0 < z < 4$, although with a large scatter at $M_* < 10^8 M_{\odot}$, likely due to the increasing effects of stellar feedback on the least massive systems. The most massive MW progenitors appear to be slightly too metal-poor compared to the observed mass-metallicity relation at $z < 3$, but their metallicity is within the scatter of the redshift-independent fundamental plane of metallicity, which relates metallicity, stellar mass and SFR.

Hence, we conclude that the GAMESH simulation that we have presented above is able to adequately describe the complex interplay between star formation and the mass exchange with the MW environment, such as gas accretion and SN-driven outflows. The improved statistics of DM mini-halos will allow us to investigate their evolution under the joint effects of radiative and chemical feedback processes and to establish their contribution to the assembly history of the MW stellar halo and its satellites.

6

Conclusions

In this Thesis we explored several open issues on early cosmic star formation. We investigated the typical mass range of the first stars, the so-called Population III (Pop III) stars, their initial mass function (IMF) and the transition to ordinary Population II (Pop II) stars, with particular attention to the role of dust. We also studied the effect of feedback processes on star formation in galaxies hosting the first stars. Since Pop III stars are also the first sources of metal enrichment of the Universe, understanding their properties is fundamental to understand the chemical evolution of galaxies and their present-day properties. In this Thesis we focused on the Milky Way (MW) Galaxy to address these issues by interpreting the observations of most iron-poor and ancient stars observed in the Galactic halo.
Here we briefly summarize the main results of this work.

We first considered the information encoded in current observations of the most iron-poor and ancient stars found in the MW halo to understand the physics of the Pop III to Pop II transition and provide constraints on the mass of Pop III stars. In order to do this we use the semi-analytic code GAMETE which reconstructs the dark matter (DM) merger tree of a MW-like halo and then follows the star formation and the chemical enrichment in all the MW progenitors along the merger tree, also including the formation and destruction of dust. In this way we can link the properties of the first stars to those of the stars which, in our model, survive until today. By comparing the simulated metallicity distribution function (MDF) and the C-enhancement of its stars with current observations, we can set some constraints on the properties of Pop III stars. We found that the existence of stars in the Galactic halo MDF with iron abundance as low as [Fe/H] $\approx$ -7 is a clear indication that the contribution of massive Pop III ($m_* \geq 140 M_\odot$, such as pair instability SNe, PISNe) to metal enrichment must largely be subdominant. On the other side, less massive stars ($m_* \leq 40 M_\odot$) should explode as faint SNe to match the [Fe/H] of the low-tail of the MDF. Hence our reference Pop III IMF extends in the mass range [10-140] $M_\odot$ with a Larson slope.
In addition, by inspecting the separate contribution of C-enhanced and of C-normal stars to the total galactic MDF, our model predicts the existence of C-normal stars at [Fe/H] $\approx$ -5 (as observed) only if the transition between massive metal-free Pop III stars and the first low-mass long-living Pop II ones is driven by dust rather than by gas-phase metals, with a critical dust-to-gas mass ratio likely to be $\mathcal{D}_{\rm cr} = 4.4 \times 10^{-9}$, in agreement with independent theoretical models.

However, the MDF predicted by our model does not show any change in slope as found in the observed MDF, in particular in the low-[Fe/H] tail which is built at very high redshift ($z > 10$), when the radiative feedback may likely affect the star formation in the first mini-halos.

Motivated by these results we investigated the role of star-forming mini-halos in shaping the properties of the Galactic halo MDF, and tried to put data-driven constraints on the IMF of Pop III stars. To this end we included mini-halos in our model with a sophisticated description of the physical processes affecting their star formation: photo-dissociation of H_2 molecules by Lyman Werner radiation (far-UV) and reionization of the intergalactic medium (IGM) by ultraviolet ionizing (UV) radiation, as well as a random sampling of the Pop III IMF when not enough total stellar mass is formed. By accounting for inefficient star formation in mini-halos, we find that the Pop III IMF is in general poorly sampled, naturally limiting the possible formation of PISNe if their mass range is accounted for in the IMF. Indeed, we obtained that, in order to form at least one PISN in a given halo, the total stellar mass formed in a burst must be larger than $\approx 10^4 M_\odot$. This confirms the subdominant role of Pop III PISNe altough the Pop III IMF extends up to 300 $M_\odot$.
We found that the resulting simulated MDF shows a better agreement with current high resolution observations with respect to the model previously presented. We reproduced the observed C-enhanced metal-poor (CEMP) plateau at [Fe/H] $\lesssim$ -5 and we predicted these stars to be mostly polluted by the nucleosynthetic signature of Pop III faint SNe (hence to be second-generation stars). Conversely, second-generation stars with the chemical imprint of more massive Pop III stars (i.e. PISNe) are predicted to appear at higher [Fe/H], due to the large amount of metals typically produced by this stellar population. In particular, we found that the distribution of these stars should peak at [Fe/H] $\approx$ -1.5, and that they represent $\approx 0.25\%$ of the total number of stars predicted at [Fe/H] < -2. This is in agreement with the current detection of only 1 star showing the possible signature of PISN stars, out of 500 stars observed in this metallicity range.
By exploring different Pop III IMFs, i.e. by changing their stellar mass range and/or slope, we show that the resulting MDF is strongly dependent on the assumed IMF. We found that a flat IMF is disfavored by observations, since the agreement between the simulated CEMP MDF and the observed one is worse than for the reference IMF, mostly at low and high [Fe/H]. On the other side, considering an IMF which accounts for the formation of low-mass Pop III stars, we find that ~30% of CEMP stars at [Fe/H]< -5 should be contaminated by zero-metallicity Asymptotic Giant Branch (AGB) stars, i.e. they should be CEMP-s rather than CEMP-no. Although this seems inconsistent with current observations a larger statistic of stars at [Fe/H] < -5 is required to completely rule out this Pop III IMF model.

To investigate the effects of radiative and chemical feedback on star formation in the high redshift Universe, we developed a new software pipeline called GAMESH, which couples our semi-analytic code GAMETE, a low resolution N-body DM simulation and the radiative transfer code CRASH to simulate MW formation. With GAMESH we have been able to study the complex interplay between chemical and radiative feedback and its effects on the formation epoque of Pop III stars and on the transition to second generations of stars. By accurately simulating the effects of radiative transfer on gas ionization and temperature, we have been able to simulate the

inhomogeneous reionization process as it occurs in a Local Volume of our Universe (on a 2 Mpc scale) and to follow the pattern of the radiation field in each region of space. We found that the reionization process is completed (with a volume-averaged H reionization of ≈ 0.998) by $z \approx 6.4$, with negligible neutral fractions left in denser regions.
We found that the effect of radiative feedback at high redshift ($z \gtrsim 12.4$) is mainly local, i.e. the radiation from newly formed Pop III stars only affects nearby objects, as indicated by the size of their H II regions. As a consequence, Pop III stars continues to form in pristine halos which are sufficiently far from previous radiation sources, and the global transition to Pop II stars is observed to occur earlier than by assuming an "ad-hoc" instantaneous reionization at $z \sim 6$. This is due to the larger contribution of longer living Pop III star forming halos to the metal enrichment. This confirms that a proper treatment of radiative feedback is required to correctly describe the stochastic star formation process at high redshift, mostly occurring in mini-halos, even with the poor statistics provided by the adopted N-body simulation.
Radiative feedback starts to have a global effect on all halos in the simulation box when the number and/or the ionizing rate of radiation sources increases due to the increasing Pop II star formation rate and to the progress of their ionized bubble overlapping. By investigating the radiative feedback on the largest scale of our simulation, we found that its global effect prevents star formation (by stopping the accretion of gas from the IGM scale) in more than 60% of galaxies by redshift $z \approx 4$.

A proper statistical sample of mini-halos has been obtained by adopting a new N-body simulation with an increased mass resolution (almost a factor of 2), thus having a better resolved MW-type halo at its center. Having a larger sample of mini-halos and a good mass and spatial resolution of the MW halo allows us to properly investigate the role of the dark and luminous MW progenitors in shaping the formation of the MW, as well as the physical properties of its progenitor galaxies in a wide redshift range. As first step we ran only the semi-analytical part of the GAMESH pipeline and we calibrated the simulation by considering the simplest case of instantaneous reionization, finding that our model is able to fit the observed and/or derived global properties of the MW: its star formation rate, the total mass of stars, the mass of gas and metals as observed at z=0.
We also investigated the properties of MW progenitors and compared with observations of candidate progenitors of MW-like galaxies at $z < 4$: we found that they generally follow the observed redshift evolution of the stellar mass, and they are in good agreement with observations of the galaxy main sequence. In addition, the distribution of the most massive MW progenitors appears to be consistent with the observed mass-metallicity relation and with the fundamental plane of metallicity.
We are now working on the implementation of the main features of the GAMETE code described in this Thesis in the GAMESH pipeline applied to the high resolution N-body simulation. These include the relaxation of the instantaneous recycling approximation (IRA), which allows to evaluate the chemical enrichment and dust production by stars with different masses in their proper lifetime. This is a mandatory step to properly simulate the environments where second-generation stars formed. Furthermore, by turning on the radiative transfer code CRASH we will investigate the effect of radiative feedback processes in regulating star formation in mini-halos. These additional studies will allow us to predict position, velocity, age and surface chemical

abundances of the most metal-poor stars in the MW and its dwarf satellites. These information will provide important indications for the observational search of fossil remnants of the first stars, to further explore the link between star formation at the highest redshifts and the Local Universe.

List of Figures

List of Tables

Bibliography

Abate C., Pols O. R., Karakas A. I., Izzard R. G., 2015, *A&A*, 576, A118

Abel T., Bryan G. L., Norman M. L., 2000, *ApJ*, 540, 39

Abel T., Bryan G. L., Norman M. L., 2002, *Science*, 295, 93

Abel T., Wise J. H., Bryan G. L., 2007, *ApJL*, 659, L87

Ahn K., Shapiro P. R., Iliev I. T., Mellema G., Pen U.-L., 2009, *ApJ*, 695, 1430

Allende Prieto C. et al., 2015, *A&A*, 579, A98

Alvarez M. A., Bromm V., Shapiro P. R., 2006, *ApJ*, 639, 621

Anninos P., Norman M. L., 1996, *ApJ*, 460, 556

Aoki W., Beers T. C., Christlieb N., Norris J. E., Ryan S. G., Tsangarides S., 2007, *ApJ*, 655, 492

Aoki W. et al., 2013, *AJ*, 145, 13

Aoki W., Tominaga N., Beers T. C., Honda S., Lee Y. S., 2014, *Science*, 345, 912

Asano R. S., Takeuchi T. T., Hirashita H., Nozawa T., 2013, *MNRAS*, 432, 637

Bahcall N. A., Fan X., 1998, *ApJ*, 504, 1

Baranov A. A., Chardonnet P., Chechetkin V. M., Filina A. A., Popov M. V., 2013, *A&A*, 558, A10

Bardeen J. M., Bond J. R., Kaiser N., Szalay A. S., 1986, *ApJ*, 304, 15

Barkana R., Loeb A., 2001, *Physics reports*, 349, 125

Barklem P. S. et al., 2005, *A&A*, 439, 129

Battaglia G. et al., 2005, *MNRAS*, 364, 433

Beers T. C., Christlieb N., 2005, *ARA&A*, 43, 531

Beers T. C., Preston G. W., Shectman S. A., 1985, *AJ*, 90, 2089

Beers T. C., Preston G. W., Shectman S. A., 1992, *AJ*, 103, 1987

Beers T. C., Rossi S., Norris J. E., Ryan S. G., Shefler T., 1999, *AJ*, 117, 981

Behroozi P. S., Wechsler R. H., Conroy C., 2013, *ApJ*, 770, 57

Benjamin J. et al., 2007, *MNRAS*, 381, 702

Bessell M. S., Norris J., 1984, *ApJ*, 285, 622

Bianchi S., Schneider R., 2007, *MNRAS*, 378, 973

Bisterzo S., Gallino R., Straniero O., Cristallo S., Käppeler F., 2012, *MNRAS*, 422, 849

Bland-Hawthorn J., Gerhard O., 2016, *ARA&A*, 54, 529

Bland-Hawthorn J., Sutherland R., Webster D., 2015, *ApJ*, 807, 154

Bocchio M., Marassi S., Schneider R., Bianchi S., Limongi M., Chieffi A., 2016, *A&A*, 587, A157

Bond J. R., Arnett W. D., Carr B. J., 1984, *ApJ*, 280, 825

Bond J. R., Cole S., Efstathiou G., Kaiser N., 1991, *ApJ*, 379, 440

Bonifacio P. et al., 2015, *A&A*, 579, A28

Bonifacio P., Limongi M., Chieffi A., 2003, *Nature*, 422, 834

Bovill M. S., Ricotti M., 2009, *ApJ*, 693, 1859

Bovill M. S., Ricotti M., 2011, *ApJ*, 741, 18

Bovy J., Rix H.-W., 2013, *ApJ*, 779, 115

Bromm V., 2013, *Reports on Progress in Physics*, 76, 112901

Bromm V., Ferrara A., Coppi P. S., Larson R. B., 2001, *MNRAS*, 328, 969

Bromm V., Loeb A., 2003, *Nature*, 425, 812

Bromm V., Yoshida N., Hernquist L., 2003, *ApJL*, 596, L135

Brook C. B., Kawata D., Scannapieco E., Martel H., Gibson B. K., 2007, *ApJ*, 661, 10

Brown A. G. A., Velázquez H. M., Aguilar L. A., 2005, *MNRAS*, 359, 1287

Bruzual G., Charlot S., 1993, *ApJ*, 405, 538

Bruzual G., Charlot S., 2003, *MNRAS*, 344, 1000

Bruzual A. G., 2002, in IAU Symposium, Vol. 207, *Extragalactic Star Clusters*, Geisler D. P., Grebel E. K., Minniti D., eds., p. 616

Caffau E. et al., 2011a, *Nature*, 477, 67

Caffau E. et al., 2012, *A&A*, 542, A51

Caffau E., Ludwig H.-G., Steffen M., Freytag B., Bonifacio P., 2011b, *Solar Phys.*, 268, 255

Cayrel R. et al., 2004, *A&A*, 416, 1117

Cerviño M., Luridiana V., 2006, *A&A*, 451, 475

Cerviño M., Luridiana V., Castander F. J., 2000, *A&A*, 360, L5

Chatzopoulos E., Wheeler J. C., 2012, *ApJ*, 748, 42

Chatzopoulos E., Wheeler J. C., Couch S. M., 2013, *ApJ*, 776, 129

Chen K.-J., Heger A., Woosley S., Almgren A., Whalen D. J., 2014, *ApJ*, 792, 44

Chen K.-J., Heger A., Woosley S., Almgren A., Whalen D. J., 2015, in Astronomical Society of the Pacific Conference Series, Vol. 498, *Numerical Modeling of Space Plasma Flows ASTRONUM-2014*, Pogorelov N. V., Audit E., Zank G. P., eds., p. 47

Chomiuk L., Povich M. S., 2011, *AJ*, 142, 197

Christlieb N., 2003, in Reviews in Modern Astronomy, Vol. 16, —it Reviews in Modern Astronomy, Schielicke R. E., ed., p. 191

Christlieb N. et al., 2002, *Nature*, 419, 904

Christlieb N., Gustafsson B., Korn A. J., Barklem P. S., Beers T. C., Bessell M. S., Karlsson T., Mizuno-Wiedner M., 2004, *ApJ*, 603, 708

Christlieb N., Schörck T., Frebel A., Beers T. C., Wisotzki L., Reimers D., 2008, *A&A*, 484, 721

Ciardi B., Ferrara A., Abel T., 2000a, *ApJ*, 533, 594

Ciardi B., Ferrara A., Governato F., Jenkins A., 2000b, *MNRAS*, 314, 611

Ciardi B., Ferrara A., Marri S., Raimondo G., 2001, *MNRAS*, 324, 381

Clark P. C., Glover S. C. O., Klessen R. S., 2008, *ApJ*, 672, 757

Clark P. C., Glover S. C. O., Smith R. J., Greif T. H., Klessen R. S., Bromm V., 2011, *Science*, 331, 1040

Cohen J. G., Christlieb N., Thompson I., McWilliam A., Shectman S., Reimers D., Wisotzki L., Kirby E., 2013, *ApJ*, 778, 56

Cole S., Lacey C. G., Baugh C. M., Frenk C. S., 2000, *MNRAS*, 319, 168

Cole S. et al., 2005, *MNRAS*, 362, 505

Cooke R. J., Madau P., 2014, *ApJ*, 791, 116

Corbelli E. et al., 2012, *A&A*, 542, A32

Crosby B. D., O'Shea B. W., Smith B. D., Turk M. J., Hahn O., 2013, *ApJ*, 773, 108

Davies J. I. et al., 2010, *A&A*, 518, L48

Dayal P., Ferrara A., Dunlop J. S., 2013, *MNRAS*, 430, 2891

de Bennassuti M., Schneider R., Valiante R., Salvadori S., 2014, *MNRAS*, 445, 3039

Dehnen W., Binney J., 1998, *MNRAS*, 294, 429

DeSouza A. L., Basu S., 2015, *MNRAS*, 450, 295

Diehl R. et al., 2006, *Nature*, 439, 45

Dijkstra M., Haiman Z., Mesinger A., Wyithe J. S. B., 2008, *MNRAS*, 391, 1961

Dijkstra M., Haiman Z., Rees M. J., Weinberg D. H., 2004, *ApJ*, 601, 666

Dobbs C. L. et al., 2014, *Protostars and Planets VI*, 3

D'Odorico V. et al., 2016, *MNRAS*, 463, 2690

Dopcke G., Glover S. C. O., Clark P. C., Klessen R. S., 2011, *ApJL*, 729, L3

Dwek E., Scalo J. M., 1980, *ApJ*, 239, 193

Efstathiou G., 2000, *MNRAS*, 317, 697

Ekström S., Meynet G., Chiappini C., Hirschi R., Maeder A., 2008, *A&A*, 489, 685

Eldridge J. J., 2011, in *Astronomical Society of the Pacific Conference Series*, Vol. 440, UP2010: Have Observations Revealed a Variable Upper End of the Initial Mass Function?, Treyer M., Wyder T., Neill J., Seibert M., Lee J., eds., p. 217

Fattahi A. et al., 2016, *MNRAS*, 457, 844

Feldman H. et al., 2003, *ApJL*, 596, L131

Ferrara A., 1998, *ApJL*, 499, L17

Ferrara A., Tolstoy E., 2000, *MNRAS*, 313, 291

Flynn C., Holmberg J., Portinari L., Fuchs B., Jahreiß H., 2006, *MNRAS*, 372, 1149

Font A. S. et al., 2011, *MNRAS*, 417, 1260

Fraser M. et al., 2011, *MNRAS*, 417, 1417

Frebel A., 2010, *Astronomische Nachrichten*, 331, 474

Frebel A. et al., 2005, *Nature*, 434, 871

Frebel A., Chiti A., Ji A. P., Jacobson H. R., Placco V. M., 2015, *arXiv*:1507.01973

Frebel A., Johnson J. L., Bromm V., 2007, *MNRAS*, 380, L40

Frebel A., Norris J. E., 2013, *Metal-Poor Stars and the Chemical Enrichment of the Universe*, SPRINGER, p. 55

Frebel A., Norris J. E., Gilmore G., Wyse R. F. G., 2016, *ApJ*, 826, 110

Fryer C. L., 1999, *ApJ*, 522, 413

Fryer C. L., Woosley S. E., Heger A., 2001, *ApJ*, 550, 372

Fu J. et al., 2013, *MNRAS*, 434, 1531

Fuller T. M., Couchman H. M. P., 2000, *ApJ*, 544, 6

Fumagalli M., da Silva R. L., Krumholz M. R., 2011, *ApJL*, 741, L26

Gal-Yam A. et al., 2011, *ApJ*, 736, 159

Galametz M., Madden S. C., Galliano F., Hony S., Bendo G. J., Sauvage M., 2011, *A&A*, 532, A56

Ganguly R., Sembach K. R., Tripp T. M., Savage B. D., 2005, *ApJS*, 157, 251

Garrison-Kimmel S., Boylan-Kolchin M., Bullock J. S., Lee K., 2014, *MNRAS*, 438, 2578

Glover S. C. O., Brand P. W. J. L., 2001, *MNRAS*, 321, 385

Gnedin N. Y., 2000, *ApJ*, 542, 535

Goriely S., Siess L., 2001, *A&A*, 378, L25

Goriely S., Siess L., 2004, *A&A*, 421, L25

Graziani L., Maselli A., Ciardi B., 2013, *MNRAS*, 431, 722

Greif T. H., Bromm V., Clark P. C., Glover S. C. O., Smith R. J., Klessen R. S., Yoshida N., Springel V., 2012, *MNRAS*, 424, 399

Greif T. H., Glover S. C. O., Bromm V., Klessen R. S., 2010, *ApJ*, 716, 510

Greif T. H., Johnson J. L., Bromm V., Klessen R. S., 2007, *ApJ*, 670, 1

Greif T. H., Springel V., White S. D. M., Glover S. C. O., Clark P. C., Smith R. J., Klessen R. S., Bromm V., 2011, *ApJ*, 737, 75

Griffen B. F., Ji A. P., Dooley G. A., Gómez F. A., Vogelsberger M., O'Shea B. W., Frebel A., 2016, *ApJ*, 818, 10

Gunn J. E. et al., 2006, *AJ*, 131, 2332

Haardt F., Madau P., 1996, *ApJ*, 461, 20

Haardt F., Madau P., 2012, *ApJ*, 746, 125

Hahn O., Abel T., 2011, *MNRAS*, 415, 2101

Haiman Z., Abel T., Rees M. J., 2000, *ApJ*, 534, 11

Haiman Z., Rees M. J., Loeb A., 1997, *ApJ*, 476, 458

Haiman Z., Thoul A. A., Loeb A., 1996, *ApJ*, 464, 523

Hansen T., Andersen J., Nordtröm B., 2013, *arXiv*:1301.7208

Hansen T. et al., 2015, *ApJ*, 807, 173

Hartwig T., Bromm V., Klessen R. S., Glover S. C. O., 2015, *MNRAS*, 447, 3892

Heger A., Fryer C. L., Woosley S. E., Langer N., Hartmann D. H., 2003, *ApJ*, 591, 288

Heger A., Woosley S. E., 2002, *ApJ*, 567, 532

Heger A., Woosley S. E., 2010, *ApJ*, 724, 341

Heger A., Woosley S. E., Spruit H. C., 2005, *ApJ*, 626, 350

Hirano S., Hosokawa T., Yoshida N., Omukai K., Yorke H. W., 2015, *MNRAS*, 448, 568

Hirano S., Hosokawa T., Yoshida N., Umeda H., Omukai K., Chiaki G., Yorke H. W., 2014, *ApJ*, 781, 60

Hirata C. M., Padmanabhan N., 2006, *MNRAS*, 372, 1175

Hirschi R., Chiappini C., Meynet G., Ekström S., Maeder A., 2007, in *American Institute of Physics Conference Series*, Vol. 948, Unsolved Problems in Stellar Physics: A Conference in Honor of Douglas Gough, Stancliffe R. J., Houdek G., Martin R. G., Tout C. A., eds., pp. 397–404

Hoeft M., Yepes G., Gottlöber S., Springel V., 2006, *MNRAS*, 371, 401

Hoekstra H. et al., 2006, *ApJ*, 647, 116

Hopkins P. F., Kereš D., Oñorbe J., Faucher-Giguère C.-A., Quataert E., Murray N., Bullock J. S., 2014, *MNRAS*, 445, 581

Horiuchi S., Beacom J. F., Kochanek C. S., Prieto J. L., Stanek K. Z., Thompson T. A., 2011, *ApJ*, 738, 154

Hosokawa T., Hirano S., Kuiper R., Yorke H. W., Omukai K., Yoshida N., 2016, *ApJ*, 824, 119

Hosokawa T., Omukai K., 2009, *ApJ*, 703, 1810

Hosokawa T., Omukai K., Yoshida N., Yorke H. W., 2011, *Science*, 334, 1250

Hummel J. A., Stacy A., Bromm V., 2016, *MNRAS*, 460, 2432

Hummel J. A., Stacy A., Jeon M., Oliveri A., Bromm V., 2015, *MNRAS*, 453, 4136

Hunt L., Dayal P., Magrini L., Ferrara A., 2016a, MNRAS, 463, 2002

Hunt L., Dayal P., Magrini L., Ferrara A., 2016b, *MNRAS*, 463, 2020

Hunt L. et al., 2012, *MNRAS*, 427, 906

Iliev I. T., Scannapieco E., Shapiro P. R., 2005, *ApJ*, 624, 491

Inayoshi K., Hosokawa T., Omukai K., 2013, *MNRAS*, 431, 3036

Ishigaki M. N., Tominaga N., Kobayashi C., Nomoto K., 2014, *ApJL*, 792, L32

Iwamoto N., Umeda H., Tominaga N., Nomoto K., Maeda K., 2005, *Science*, 309, 451

Jeans J. H., 1928, *Astronomy and cosmogony*. Cambridge, The University press

Jena T. et al., 2005, *MNRAS*, 361, 70

Jenkins E. B., 2009, *ApJ*, 700, 1299

Jeon M., Pawlik A. H., Bromm V., Milosavljević M., 2014, *MNRAS*, 444, 3288

Jeon M., Pawlik A. H., Greif T. H., Glover S. C. O., Bromm V., Milosavljević M., Klessen R. S., 2012, *ApJ*, 754, 34

Joggerst C. C., Almgren A., Woosley S. E., 2010, *ApJ*, 723, 353

Joggerst C. C., Whalen D. J., 2011, *ApJ*, 728, 129

Joggerst C. C., Woosley S. E., Heger A., 2009, *ApJ*, 693, 1780

Johnson J. L., Greif T. H., Bromm V., 2007, *ApJ*, 665, 85

Johnson J. L., Greif T. H., Bromm V., 2008, *MNRAS*, 388, 26

Jones A. P., Tielens A. G. G. M., Hollenbach D. J., 1996, *ApJ*, 469, 740

Kafle P. R., Sharma S., Lewis G. F., Bland-Hawthorn J., 2012, *ApJ*, 761, 98

Kafle P. R., Sharma S., Lewis G. F., Bland-Hawthorn J., 2014, *ApJ*, 794, 59

Karlsson T., 2006, *ApJL*, 641, L41

Karlsson T., Bromm V., Bland-Hawthorn J., 2013, *Reviews of Modern Physics*, 85, 809

Karlsson T., Johnson J. L., Bromm V., 2008, *ApJ*, 679, 6

Kawata D., Gibson B. K., 2003a, *MNRAS*, 340, 908

Kawata D., Gibson B. K., 2003b, *MNRAS*, 346, 135

Kawata D., Okamoto T., Gibson B. K., Barnes D. J., Cen R., 2013, *MNRAS*, 428, 1968

Keller S. C. et al., 2014, *Nature*, 506, 463

Kennicutt R. C., Evans N. J., 2012, *ARA&A*, 50, 531

Kennicutt, Jr. R. C., 1998, *ARA&A*, 36, 189

Kitayama T., Susa H., Umemura M., Ikeuchi S., 2001, *MNRAS*, 326, 1353

Kitayama T., Tajiri Y., Umemura M., Susa H., Ikeuchi S., 2000, *MNRAS*, 315, L1

Kitayama T., Yoshida N., 2005, *ApJ*, 630, 675

Kitching T. D., Heavens A. F., Taylor A. N., Brown M. L., Meisenheimer K., Wolf C., Gray M. E., Bacon D. J., 2007, *MNRAS*, 376, 771

Klessen R. S., Glover S. C. O., Clark P. C., 2012, *MNRAS*, 421, 3217

Klypin A., Kravtsov A. V., Valenzuela O., Prada F., 1999, *ApJ*, 522, 82

Kobayashi C., Tominaga N., Nomoto K., 2011, *ApJL*, 730, L14

Komatsu E. et al., 2009, *ApJS*, 180, 330

Komiya Y., 2011, *ApJ*, 736, 73

Komiya Y., Habe A., Suda T., Fujimoto M. Y., 2009, *ApJL*, 696, L79

Komiya Y., Habe A., Suda T., Fujimoto M. Y., 2010, *ApJ*, 717, 542

Komiya Y., Suda T., Fujimoto M. Y., 2016, *ApJ*, 820, 59

Komiya Y., Suda T., Minaguchi H., Shigeyama T., Aoki W., Fujimoto M. Y., 2007, *ApJ*, 658, 367

Kubryk M., Prantzos N., Athanassoula E., 2015, *A&A*, 580, A126

Kuhlen M., Madau P., 2005, *MNRAS*, 363, 1069

Kuo T.-M., Hirashita H., Zafar T., 2013, *MNRAS*, 436, 1238

Lacey C., Cole S., 1993, *MNRAS*, 262, 627

Larson R. B., 1998, *MNRAS*, 301, 569

Lee Y. S. et al., 2013, *AJ*, 146, 132

Lepp S., Shull J. M., 1984, *ApJ*, 280, 465

Li Y.-S., De Lucia G., Helmi A., 2010, *MNRAS*, 401, 2036

Licquia T. C., Newman J. A., 2015, *ApJ*, 806, 96

Lucatello S., Tsangarides S., Beers T. C., Carretta E., Gratton R. G., Ryan S. G., 2005, *ApJ*, 625, 825

Mac Low M.-M., Ferrara A., 1999, *ApJ*, 513, 142

Macciò A. V., Kang X., Fontanot F., Somerville R. S., Koposov S., Monaco P., 2010, *MNRAS*, 402, 1995

Macciò A. V., Kang X., Moore B., 2009, *ApJL*, 692, L109

Machacek M. E., Bryan G. L., Abel T., 2001, *ApJ*, 548, 509

Machida M. N., Doi K., 2013, *MNRAS*, 435, 3283

Mackey J., Bromm V., Hernquist L., 2003, *ApJ*, 586, 1

Madau P., Ferrara A., Rees M. J., 2001, *ApJ*, 555, 92

Madau P., Kuhlen M., Diemand J., Moore B., Zemp M., Potter D., Stadel J., 2008, *ApJL*, 689, L41

Madden S. C. et al., 2013, *PASP*, 125, 600

Maeder A., Meynet G., Chiappini C., 2015, *A&A*, 576, A56

Maio U., Ciardi B., Dolag K., Tornatore L., Khochfar S., 2010, *MNRAS*, 407, 1003

Maio U., Khochfar S., Johnson J. L., Ciardi B., 2011, *MNRAS*, 414, 1145

Maio U., Viel M., 2015, *MNRAS*, 446, 2760

Maiolino R. et al., 2008, *A&A*, 488, 488

Mannucci F., Cresci G., Maiolino R., Marconi A., Gnerucci A., 2010, *MNRAS*, 408, 2115

Mannucci F. et al., 2009, *MNRAS*, 398, 1915

Marassi S., Chiaki G., Schneider R., Limongi M., Omukai K., Nozawa T., Chieffi A., Yoshida N., 2014, *ApJ*, 794, 100

Marassi S., Schneider R., Limongi M., Chieffi A., Bocchio M., Bianchi S., 2015, *MNRAS*, 454, 4250

Maselli A., Ciardi B., Kanekar A., 2009, *MNRAS*, 393, 171

Maselli A., Ferrara A., 2005, *MNRAS*, 364, 1429

Maselli A., Ferrara A., Ciardi B., 2003, *MNRAS*, 345, 379

Mashchenko S., Couchman H. M. P., Sills A., 2006, *ApJ*, 639, 633

Masseron T., Johnson J. A., Plez B., van Eck S., Primas F., Goriely S., Jorissen A., 2010, *A&A*, 509, A93

McDonald P. et al., 2005, *ApJ*, 635, 761

McKee C., 1989, in IAU Symposium, Vol. 135, Interstellar Dust, Allamandola L. J., Tielens A. G. G. M., eds., p. 431

McKee C. F., Ostriker E. C., 2007, *ARA&A*, 45, 565

McKee C. F., Tan J. C., 2008, *ApJ*, 681, 771

McKee C. F., Williams J. P., 1997, *ApJ*, 476, 144

McMillan P. J., 2011, *MNRAS*, 414, 2446

Meléndez J., Placco V. M., Tucci-Maia M., Ramírez I., Li T. S., Perez G., 2016, *A&A*, 585, L5

Ménard B., Scranton R., Fukugita M., Richards G., 2010, *MNRAS*, 405, 1025

Meynet G., Ekström S., Maeder A., 2006, *A&A*, 447, 623

Meynet G., Hirschi R., Ekstrom S., Maeder A., Georgy C., Eggenberger P., Chiappini C., 2010, *A&A*, 521, A30

Meynet G., Maeder A., 2002, *A&A*, 390, 561

Mirocha J., 2014, *MNRAS*, 443, 1211

Mo H., van den Bosch F. C., White S., 2010, *Galaxy Formation and Evolution*. Cambridge University Press

Molaro P., Bonifacio P., 1990, *A&A*, 236, L5

Molaro P., Castelli F., 1990, *A&A*, 228, 426

Moore B., Ghigna S., Governato F., Lake G., Quinn T., Stadel J., Tozzi P., 1999, ApJL, 524, L19

Mori M., Ferrara A., Madau P., 2002, *ApJ*, 571, 40

Muratov A. L., Gnedin O. Y., Gnedin N. Y., Zemp M., 2013, *ApJ*, 772, 106

Navarro J. F., Frenk C. S., White S. D. M., 1996, *ApJ*, 462, 563

Navarro J. F., Frenk C. S., White S. D. M., 1997, *ApJ*, 490, 493

Nishi R., Susa H., 1999, *ApJL*, 523, L103

Nishi R., Tashiro M., 2000, *ApJ*, 537, 50

Noh Y., McQuinn M., 2014, *MNRAS*, 444, 503

Norris J. E., Christlieb N., Korn A. J., Eriksson K., Bessell M. S., Beers T. C., Wisotzki L., Reimers D., 2007, *ApJ*, 670, 774

Norris J. E., Gilmore G., Wyse R. F. G., Yong D., Frebel A., 2010, *ApJL*, 722, L104

Norris J. E. et al., 2013, *ApJ*, 762, 28

Nozawa T., Kozasa T., Habe A., 2006, *ApJ*, 648, 435

Oh S. P., Haiman Z., 2002, *ApJ*, 569, 558

Ohkubo T., Umeda H., Maeda K., Nomoto K., Suzuki T., Tsuruta S., Rees M. J., 2006, *ApJ*, 645, 1352

Okamoto T., Frenk C. S., Jenkins A., Theuns T., 2010, *MNRAS*, 406, 208

Okamoto T., Gao L., Theuns T., 2008, *MNRAS*, 390, 920

Omukai K., 2000, *ApJ*, 534, 809

Omukai K., 2012, *PASJ*, 64

Omukai K., Hosokawa T., Yoshida N., 2010, *ApJ*, 722, 1793

Omukai K., Nishi R., 1999, *ApJ*, 518, 64

Omukai K., Palla F., 2003, *ApJ*, 589, 677

Omukai K., Tsuribe T., Schneider R., Ferrara A., 2005, *ApJ*, 626, 627

O'Shea B. W., Norman M. L., 2007, *ApJ*, 654, 66

O'Shea B. W., Wise J. H., Xu H., Norman M. L., 2015, *ApJL*, 807, L12

Palla F., Galli D., Silk J., 1995, *ApJ*, 451, 44

Pallottini A., Ferrara A., Gallerani S., Salvadori S., D'Odorico V., 2014, *MNRAS*, 440, 2498

Papovich C. et al., 2015, *ApJ*, 803, 26

Parkinson H., Cole S., Helly J., 2008, *MNRAS*, 383, 557

Pastorello A. et al., 2006, *MNRAS*, 370, 1752

Pastorello A. et al., 2004, *MNRAS*, 347, 74

Patel S. G. et al., 2013, *ApJ*, 778, 115

Peebles P. J. E., 1993, *Physics Today*, 46, 87

Peeples M. S., Werk J. K., Tumlinson J., Oppenheimer B. D., Prochaska J. X., Katz N., Weinberg D. H., 2014, *ApJ*, 786, 54

Peters T., Schleicher D. R. G., Smith R. J., Schmidt W., Klessen R. S., 2014, *MNRAS*, 442, 3112

Pindao M., Schaerer D., González Delgado R. M., Stasińska G., 2002, *A&A*, 394, 443

Placco V. M., Frebel A., Beers T. C., Karakas A. I., Kennedy C. R., Rossi S., Christlieb N., Stancliffe R. J., 2013, *ApJ*, 770, 104

Placco V. M., Frebel A., Beers T. C., Stancliffe R. J., 2014, *ApJ*, 797, 21

Planck Collaboration et al., 2016, *arXiv*:1605.03507

Planck Collaboration et al., 2014, *A&A*, 571, A16

Planck Collaboration et al., 2015, *arXiv*:1502.01589

Podio L., Bacciotti F., Nisini B., Eislöffel J., Massi F., Giannini T., Ray T. P., 2006, *A&A*, 456, 189

Powell L. C., Slyz A., Devriendt J., 2011, *MNRAS*, 414, 3671

Press W. H., Schechter P., 1974, *ApJ*, 425

Primas F., Molaro P., Castelli F., 1994, *A&A*, 290

Raiteri C. M., Villata M., Navarro J. F., 1996, *A&A*, 315, 105

Reed D. S., Bower R., Frenk C. S., Gao L., Jenkins A., Theuns T., White S. D. M., 2005, *MNRAS*, 363, 393

Reiprich T. H., Böhringer H., 2002, *ApJ*, 567, 716

Rémy-Ruyer A. et al., 2014, *A&A*, 563, A31

Ricotti M., Gnedin N. Y., Shull J. M., 2001, *ApJ*, 560, 580

Ricotti M., Gnedin N. Y., Shull J. M., 2002, *ApJ*, 575, 49

Ricotti M., Gnedin N. Y., Shull J. M., 2008, *ApJ*, 685, 21

Ripamonti E., Iocco F., Ferrara A., Schneider R., Bressan A., Marigo P., 2010, *MNRAS*, 406, 2605

Ritter J. S., Safranek-Shrader C., Gnat O., Milosavljević M., Bromm V., 2012, *ApJ*, 761, 56

Ritter J. S., Safranek-Shrader C., Milosavljević M., Bromm V., 2016, *MNRAS*, 463, 3354

Robitaille T. P., Whitney B. A., 2010, *ApJL*, 710, L11

Ryan S. G., Norris J. E., 1991, *AJ*, 101, 1835

Safranek-Shrader C., Milosavljević M., Bromm V., 2014, *MNRAS*, 438, 1669

Sakurai Y., Vorobyov E. I., Hosokawa T., Yoshida N., Omukai K., Yorke H. W., 2016, *MNRAS*, 459, 1137

Sales L. V., Marinacci F., Springel V., Petkova M., 2014, *MNRAS*, 439, 2990

Salvadori S., 2009, PhD Thesis at SISSA/ISAS

Salvadori S., Dayal P., Ferrara A., 2010a, *MNRAS*, 407, L1

Salvadori S., Ferrara A., 2009, *MNRAS*, 395, L6

Salvadori S., Ferrara A., 2012, *MNRAS*, 421, L29

Salvadori S., Ferrara A., Schneider R., 2008, *MNRAS*, 386, 348

Salvadori S., Ferrara A., Schneider R., Scannapieco E., Kawata D., 2010b, *MNRAS*, 401, L5

Salvadori S., Schneider R., Ferrara A., 2007, *MNRAS*, 381, 647

Salvadori S., Skúladóttir Á., de Bennassuti M., 2016, *arXiv*:1512.05506

Salvadori S., Skúladóttir Á., Tolstoy E., 2015, *MNRAS*, 454, 1320

Salvadori S., Tolstoy E., Ferrara A., Zaroubi S., 2014, *MNRAS*, 437, L26

Santoro F., Shull J. M., 2006, *ApJ*, 643, 26

Sawala T. et al., 2016, *MNRAS*, 457, 1931

Scannapieco E., Kawata D., Brook C. B., Schneider R., Ferrara A., Gibson B. K., 2006, *ApJL*, 653, 285

Scannapieco E., Schneider R., Ferrara A., 2003, *ApJ*, 589, 35

Schaerer D., 2002, *A&A*, 382, 28

Schaye J., Aguirre A., Kim T.-S., Theuns T., Rauch M., Sargent W. L. W., 2003, *ApJ*, 596, 768

Schneider R., Ferrara A., Natarajan P., Omukai K., 2002, *ApJ*, 571, 30

Schneider R., Omukai K., Bianchi S., Valiante R., 2012a, *MNRAS*, 419, 1566

Schneider R., Omukai K., Inoue A. K., Ferrara A., 2006, *MNRAS*, 369, 1437

Schneider R., Omukai K., Limongi M., Ferrara A., Salvaterra R., Chieffi A., Bianchi S., 2012b, *MNRAS*, 423, L60

Schneider R., Valiante R., Ventura P., dell'Agli F., Di Criscienzo M., Hirashita H., Kemper F., 2014, *MNRAS*, 442, 1440

Schneider et al., 2004, *MNRAS*, 351, 1379

Schörck T. et al., 2009, *A&A*, 507, 817

Schreiber C. et al., 2015, *A&A*, 575, A74

Sheth R. K., Tormen G., 1999, *MNRAS*, 308, 119

Silk J., 2003, *MNRAS*, 343, 249

Slavin J. D., 2009, *Space Sci. Rev.*, 143, 311

Smith L. F., Biermann P., Mezger P. G., 1978, *A&A*, 66, 65

Smith R. J., Glover S. C. O., Clark P. C., Greif T., Klessen R. S., 2011, *MNRAS*, 414, 3633

Smith R. J., Glover S. C. O., Clark P. C., Klessen R. S., Springel V., 2014, *MNRAS*, 441, 1628

Smith R. J., Hosokawa T., Omukai K., Glover S. C. O., Klessen R. S., 2012, *MNRAS*, 424, 457

Sneden C., Cowan J. J., Gallino R., 2008, *ARA&A*, 46, 241

Spergel D. N. et al., 2007, *ApJS*, 170, 377

Spergel D. N. et al., 2003, *ApJS*, 148, 175

Spite M., Caffau E., Bonifacio P., Spite F., Ludwig H.-G., Plez B., Christlieb N., 2013, *A&A*, 552, A107

Springel V., Hernquist L., 2003, *MNRAS*, 339, 312

Springel V. et al., 2005, *Nature*, 435, 629

Stacy A., Bromm V., Lee A. T., 2016, *MNRAS*, 462, 1307

Stacy A., Greif T. H., Bromm V., 2010, *MNRAS*, 403, 45

Stacy A., Greif T. H., Bromm V., 2012, *MNRAS*, 422, 290

Stacy A., Pawlik A. H., Bromm V., Loeb A., 2014, *MNRAS*, 441, 822

Stahler S. W., Palla F., 2005, *The Formation of Stars*. WILEY-VCH, p. 865

Starkenburg E., Shetrone M. D., McConnachie A. W., Venn K. A., 2014, *MNRAS*, 441, 1217

Starkenburg T. K., Helmi A., Sales L. V., 2016, *A&A*, 587, A24

Sternberg A., Le Petit F., Roueff E., Le Bourlot J., 2014, *ApJ*, 790, 10

Suda T., Aikawa M., Machida M. N., Fujimoto M. Y., Iben J. I., 2004, *ApJ*, 611, 476

Suda T. et al., 2008, *PASJ*, 60, 1159

Sugiyama N., 1995, *ApJS*, 100, 281

Susa H., 2013, *ApJ*, 773, 185

Susa H., Hasegawa K., Tominaga N., 2014, *ApJ*, 792, 32

Susa H., Kitayama T., 2000, *MNRAS*, 317, 175

Susa H., Umemura M., 2004, *ApJL*, 610, L5

Susa H., Umemura M., 2006, *ApJL*, 645, L93

Suwa Y., Takiwaki T., Kotake K., Sato K., 2007, *PASJ*, 59, 771

Takahashi K., Umeda H., Yoshida T., 2014, *ApJ*, 794, 40

Takahashi K., Yoshida T., Umeda H., Sumiyoshi K., Yamada S., 2016, *MNRAS*, 456, 1320

Tegmark M. et al., 2004, *ApJ*, 606, 702

Tegmark M., Silk J., Rees M. J., Blanchard A., Abel T., Palla F., 1997, *ApJ*, 474, 1

Tielens A. G. G. M., 2005, *The Physics and Chemistry of the Interstellar Medium*. Cambridge University Press

Tinsley B. M., 1980, *Fundamentals of Cosmic Physics*, 5, 287

Tominaga N., Iwamoto N., Nomoto K., 2014, *ApJ*, 785, 98

Tominaga N., Umeda H., Nomoto K., 2007, *ApJ*, 660, 516

Tornatore L., Ferrara A., Schneider R., 2007, *MNRAS*, 382, 945

Tsuribe T., Omukai K., 2006, *ApJL*, 642, L61

Tsuribe T., Omukai K., 2008, *ApJL*, 676, L45

Tumlinson J., 2006, *ApJ*, 641, 1

Tumlinson J., 2007, *ApJL*, 664, L63

Tumlinson J., 2010, *ApJ*, 708, 1398

Turatto M. et al., 1998, *ApJL*, 498, L129

Turk M. J., Oishi J. S., Abel T., Bryan G. L., 2012, *ApJ*, 745, 154

Umeda H., Nomoto K., 2002, *ApJ*, 565, 385

Umeda H., Nomoto K., 2003, *Nature*, 422, 871

Valiante R., Schneider R., Bianchi S., Andersen A. C., 2009, *MNRAS*, 397, 1661

Valiante R., Schneider R., Salvadori S., Bianchi S., 2011, *MNRAS*, 416, 1916

Valiante R., Schneider R., Salvadori S., Gallerani S., 2014, *MNRAS*, 444, 2442

Valiante R., Schneider R., Volonteri M., Omukai K., 2016, *MNRAS*, 457, 3356

van den Hoek L. B., Groenewegen M. A. T., 1997, *A&AS*, 123, 305

van Dokkum P. G. et al., 2013, *ApJL*, 771, L35

Volonteri M., Haardt F., Madau P., 2003, *ApJ*, 582, 559

Vorobyov E. I., Baraffe I., Harries T., Chabrier G., 2013, *A&A*, 557, A35

Wada K., Venkatesan A., 2003, *ApJ*, 591, 38

Wang W., Han J., Cooper A. P., Cole S., Frenk C., Lowing B., 2015, *MNRAS*, 453, 377

Welty D. E., Jenkins E. B., Raymond J. C., Mallouris C., York D. G., 2002, *ApJ*, 579, 304

Wen Z. L., Han J. L., Liu F. S., 2010, *MNRAS*, 407, 533

Whalen D., O'Shea B. W., Smidt J., Norman M. L., 2008, *ApJ*, 679, 925

White S. D. M., Efstathiou G., Frenk C. S., 1993, *MNRAS*, 262, 1023

Wise J. H., Abel T., 2008, *ApJ*, 685, 40

Wise J. H., Demchenko V. G., Halicek M. T., Norman M. L., Turk M. J., Abel T., Smith B. D., 2014, *MNRAS*, 442, 2560

Wise J. H., Turk M. J., Norman M. L., Abel T., 2012, *ApJ*, 745, 50

Wisotzki L., Christlieb N., Bade N., Beckmann V., Köhler T., Vanelle C., Reimers D., 2000, *A&A*, 358, 77

Woosley S. E., Weaver T. A., 1995, *ApJS*, 101, 181

Wyithe J. S. B., Cen R., 2007, *ApJ*, 659, 890

Xu H., Wise J. H., Norman M. L., Ahn K., O'Shea B. W., 2016, *arXiv*:1604.07842

Yanny B. et al., 2009, *AJ*, 137, 4377

Yong D. et al., 2013a, *ApJ*, 762, 26

Yong D. et al., 2013b, *ApJ*, 762, 27

Yoon S.-C., Dierks A., Langer N., 2012, *A&A*, 542, A113

York D. G., Adelman J., Anderson, Jr. J. E., Anderson S. F., Annis J., Bahcall N. A., *et al.*, 2000, *AJ*, 120, 1579

Yoshida N., Abel T., Hernquist L., Sugiyama N., 2003, *ApJ*, 592, 645

Yoshida N., Omukai K., Hernquist L., Abel T., 2006, *ApJ*, 652, 6

Zafar T., Watson D., 2013, *A&A*, 560, A26

Zel'dovich Y. B., 1970, *A&A*, 5, 84

Zhukovska S., 2014, *A&A*, 562, A76

Zhukovska S., Gail H.-P., Trieloff M., 2008, *A&A*, 479, 453